THE FLUID MECHANICS OF EMBRYONIC NODAL CILIA

by

ANDREW A. SMITH

A thesis submitted to
The University of Birmingham
for the degree of
DOCTOR OF PHILOSOPHY

School of Mathematics
College of Engineering and Physical Sciences
The University of Birmingham
June 2013

Abstract

Symmetry breaking of the left-right body axis is a crucial step in development for many vertebrate species. The left-right axis is the final axis to be determined after the dorsal-ventral and anterior-posterior axes and in many species this is initiated with a directional cilia-driven fluid flow located in the organising structure. Experiments and mathematical models of the mouse organising structure have shown that a clockwise rotation of cilia, when viewed from tip to base, coupled with a tilt towards the posterior direction, will produce an asymmetric fluid flow.

Experimental observations of the mouse organising structure, the node, show that cilia are arranged differently depending on the stage of development; a theoretical study of the fluid mechanics of these stages is carried out mathematically for the first time in this work. Experimental results show that at early stages of development, where cilia have a small tilt angle, the fluid flow is vortical. At later stages of development, where the tilt angle is significantly larger, an asymmetric right to left flow is observed. Using singularities of Stokes flow, slender body theory and the boundary integral equation, a computational model of the fluid flow in the mouse organising structure for a range of cilia configurations is developed and run on the University of Birmingham's cluster, BlueBEAR. The computational results show the development of a directional particle transport as the cilia tilt increases. These results agree well with the experimental observations and indicate that a directional fluid flow is not produced as soon as the organising structure is present.

Another species of great interest for studying this stage of development is the zebrafish. The zebrafish organising structure, the Kupffer's vesicle, has a more complex internal arrangement of cilia than the mouse node. Experimental studies have shown that the fluid flow forms an anticlockwise swirl about the dorsal-ventral axis when looking in the ventral direction. Previous experimental observations have led to two different models of how cilia produce flow in the Kupffer's vesicle. One model states that posteriorly tilted

cilia coupled with a greater cilia density on the dorsal roof will produce the observed fluid flow whilst another model proposes that cilia located around the 'equator' of the Kupffer's vesicle have a tilt in the dorsal direction.

A mathematical model is developed and run on BlueBEAR using the boundary element method and the regularised boundary integral equation to investigate potential cilia mechanisms that produce the observed fluid flow. The computational results of this model suggest that a possible mechanism capable of producing a similar flow to those observed in experiment is a combination of posteriorly tilted roof and floor cilia, dorsally tilted equatorial cilia, and a greater number of cilia on the roof in the dorsal-anterior 'corner' than on the floor. Recently, it has been observed that the majority of cilia in the zebrafish Kupffer's vesicle fall into two main groups. One group of cilia are observed to rotate with one frequency while a second group of cilia exhibit two frequencies during their rotation. A model of the two groups of cilia is presented by introducing a 'wobble' into the semi-cone angle of the cilia that exhibit two frequencies. The observed frequencies have also been shown to be different between wildtype and mutant embryos where the missing gene in the mutant embryos also affects cilium length. Cilium length is important when studying Stokes flow because the velocity is proportional to cilium length and the volume flow rate is proportional to the cube of cilium length. The computed fluid flows suggest that the introduction of a wobble in wildtype embryos will not dramatically change the flow, however in mutant embryos the combined effect of changing the rotation frequencies and cilium length drastically alters the fluid flow; the average velocities agree well with the experimental observations. As with the mouse model, these results suggest that the zebrafish Kupffer's vesicle has to develop a combination of rotation mechanisms and cilium length before an appropriate symmetry breaking flow can be established.

ACKNOWLEDGEMENTS

First and foremost I would like to thank my supervisors Professor John Blake and Dr. David Smith. Their great insight and expertise in this field have been invaluable for the duration of this work. Secondly, the EPSRC for the financial support without which I would not have been able to carry out this work. My friends and family, with special thanks to my wife, Sophie, for all her encouragement and support and in particular Thomas Montenegro-Johnson, for many great discussions and a wonderful collaboration during the zebrafish study in which he contributed the domain meshing.

I also wish to acknowledge again my supervisors for all their support during times of preparing published work. Work in this thesis has been published in the Journal of Engineering Mathematics, Journal of Fluid Mechanics and European Physical Journal E and copies of these publications can be found in the appendices. The involvement in these has been extremely helpful whilst writing this work. The computations in these publications and in this work were performed using the University of Birmingham's BlueBEAR high performance computing service, please see `http://www.bear.bham.ac.uk` for more details.

Finally, I wish to acknowledge Dr. Susana Lopes along with her colleagues and students from the Cilia Regulation and Disease Lab at CEDOC, Lisbon. The great work her and her team conduct on zebrafish embryos and the first zebrafish model presented here has led to an exciting collaboration on the two frequency cilia groups and a publication is currently being prepared.

CONTENTS

LIST OF FIGURES

LIST OF TABLES

CHAPTER 1

INTRODUCTION AND BACKGROUND

From the outside vertebrates appear bilaterally symmetric. However, in many species, internal body plans are asymmetrically arranged in a very organised way. For example, the heart can normally be found on the left in chickens, frogs, mice and zebrafish [38] to name but a few, and of course humans, see figure 1.1(a). Furthermore, in humans, the liver is usually found on the right side of the body, whereas the stomach and spleen are on the left side.

During embryonic development three body axes are established. The first is the dorsal-ventral (D-V) axis which runs from an organism's back to their front and is established upon implantation of the fertilised egg. The D-V axis is followed by the anterior-posterior (A-P) axis which is from the head of an organism to the feet and is established randomly. Up to this stage of development any symmetry problems in the D-V and A-P axes can easily be corrected by a simple rotation or reflection of these two established body axes. The same statement cannot be said about an organism once the third axis, the left-right (L-R) axis, is established as this axis determines the chirality of the embryo and simple rotations and reflections of the body axes is no longer possible to correct any problems, see figure 1.1(c).

It is only in the last 80 years that the mechanisms involved in establishing L-R asymmetric development have begun to be understood. Kartagener [43], amongst others, identified a triad of common symptoms, sinusitis, bronchiectasis and forms of *situs inver-*

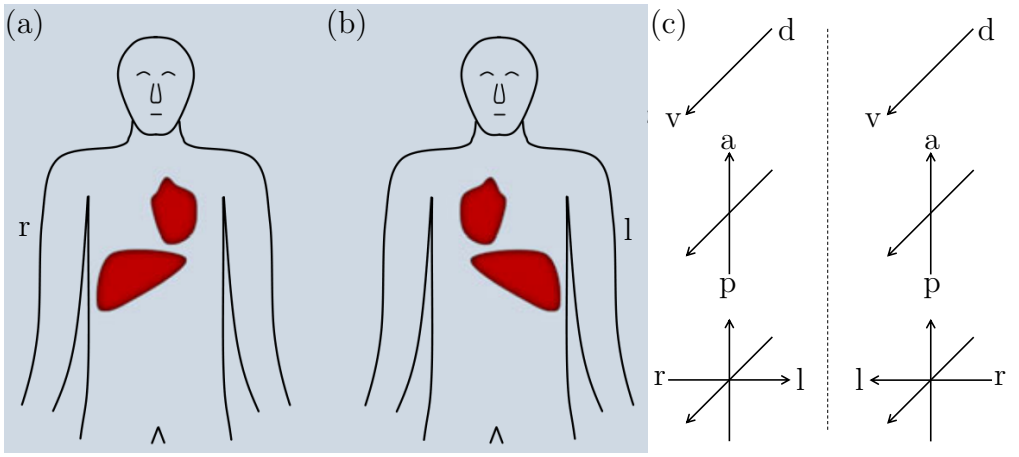

Figure 1.1: Organ location for (a) normal *situs* and (b) *situs inversus*; the condition *situs inversus* affects less than 1 % of the human population. Reprinted with permission from Cambridge University Press, Smith *et al.* [73] (2012), *Journal of Fluid Mechanics*. (c) Schematic of the body axes. When only the dorsal-ventral axis or the dorsal-ventral and anterior-posterior axes are established the system is achiral, the mirror image is superimposable on the original. Once the left-right axis is defined the system takes one of two chiral forms as depicted. Axis notation d, dorsal; v, ventral, a, anterior; p, posterior; l, left and r, right.

sus, the lateral transposition of internal organs, see figure 1.1(b). This became known as Kartagener's triad and if a patient has developed sinusitis and bronchiectasis they are said to have Kartagener's syndrome [3]. Patients with *situs inversus* can exhibit many different types of organ positioning, see figure 1.2. *Situs inversus totalis* is the complete L-R reversal of all organ positionings in the body and a patient with this type of *situs inversus* will function like a patient with *situs solitus*, no organ positioning reversal. Impaired organ function is found in patients with only a portion of organs with L-R positioning reversal. For example *situs inversus thoracalis* reverses upper abdomen organs whereas *situs inversus abdominalis* reverses lower abdomen organs and in these cases the upper and lower organs will have impaired function respectively. Two further conditions associated with *situs inversus* are polysplenia and asplenia. Both result in a lack of asymmetry of body organs and multiple spleens in polysplenia and an absent spleen in asplenia.

In 1974 Afzelius reported dysfunctional cilia and flagella in four male patients; three of the patients were reported to have dysfunctional lung cilia, another three of the patients had *situs inversus*, and infertility was reported where sperm flagella were missing

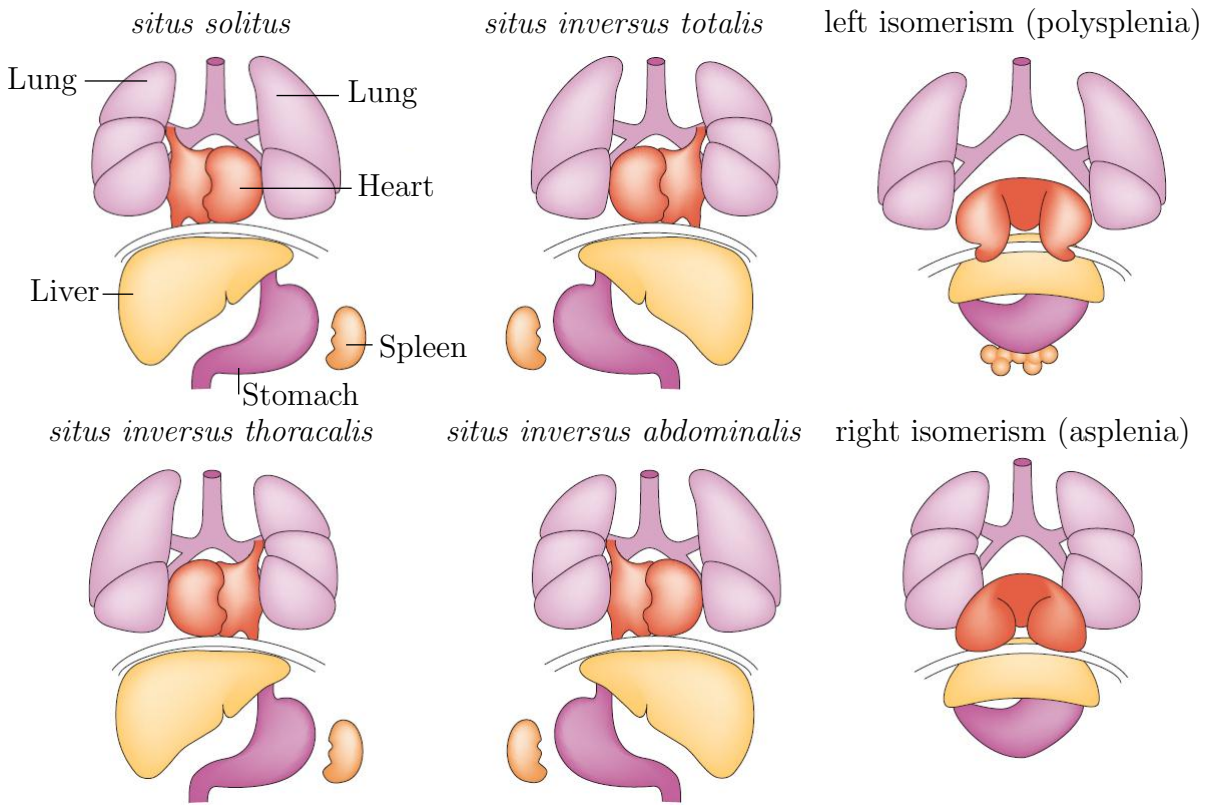

Figure 1.2: An illustration of normal left-right asymmetric organ location in the human body (*situs solitus*) and five laterality defects affecting the lungs, heart, liver, stomach and spleen. Reprinted with permission from Nature Publishing Group, Fliegauf *et al.* [28] (2007), *Nature Reviews Molecular Cell Biology.*

the motor protein dynein. Cilia and flagella are microscopic hair-like structures found throughout nature in and on many species and dynein is a protein that converts chemical energy into mechanical energy for movement. Most commonly, cilia and flagella will either have a $9 + 0$ or $9 + 2$ internal structure, see figure 1.3, which is a structure consisting of 9 outer microtubule doublets and a central pair of microtubule singlets for a $9 + 2$ configuration and no central pair for $9 + 0$. These two types of cilia and flagella can be further subcategorised into motile and immotile $9 + 0$ and $9 + 2$ cilia [28] where motile cilia have dynein arms and immotile cilia do not; some common occurrences of these types of cilia are shown in figure 1.4. Based on the observations of dysfunctional cilia and flagella, Afzelius hypothesised that the establishment of L-R asymmetry of the body could be through the movement of cilia on embryonic epithelial tissue [2].

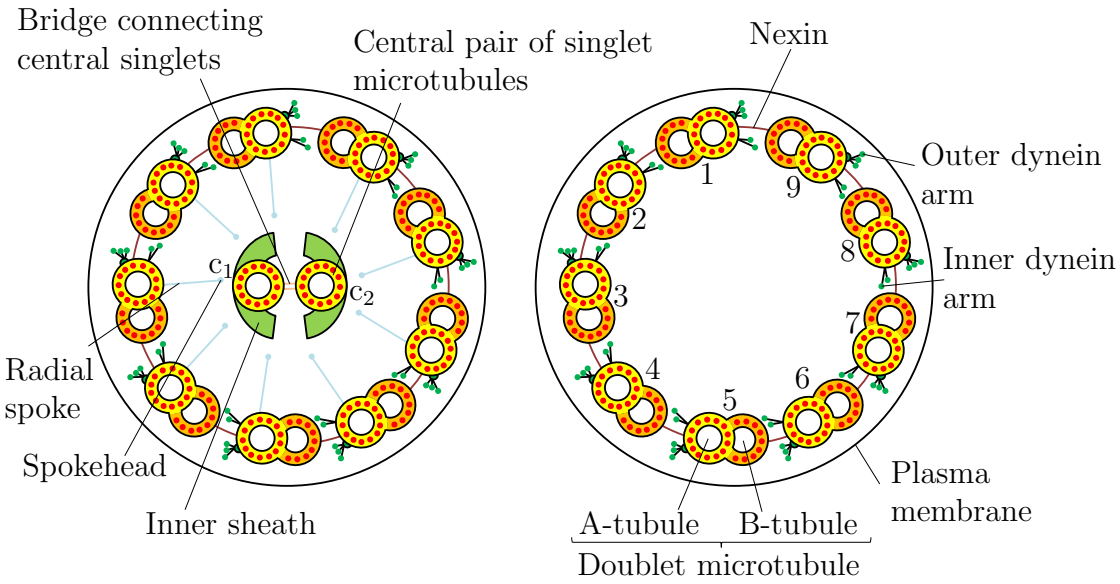

Figure 1.3: Cross section of a cilium showing the 9 + 2 and 9 + 0 internal structures of microtubules and the location of dynein arms in motile cilia. A 9 + 0 configuration is missing the central pair of microtubules as well as the connections to the outer doublets. The outer doublets are labelled with the convention of viewing the cilium from tip to base. Redrawn from Lodish *et al.* [55].

It took a further 20 years until Sulik *et al.* [80] discovered a structure on a mouse embryo at 7–9 days post-fertilisation (dpf), referred to as the mouse organising structure, mouse node or simply node, for the link between cilia and asymmetric development to be further explored. The mouse node is a triangular depression that forms on the ventral surface of the embryo and is 50–100 μm from left to right and 10–20 μm from dorsal to ventral. The node is covered with a membrane, referred to as a Reichert's membrane, and is filled with extraembryonic fluid [31]. The dorsal surface of the mouse node is covered with a few hundred ciliated cells each expressing a single cilium [32] that projects into the flow domain from the cell surface, measuring 3–5 μm in length with a diameter of 0.3 μm [33], see figure 1.5.

The original observations of cilia in the mouse node showed that they had the same internal structure as known immotile cilia, leading to the early suggestion that the cilia in the mouse node were immotile. Immotile cilia naturally do not move under their own action whereas dysfunctional motile cilia should normally move but they do not due to problems with internal mechanisms, for example lacking the motor protein dynein. How-

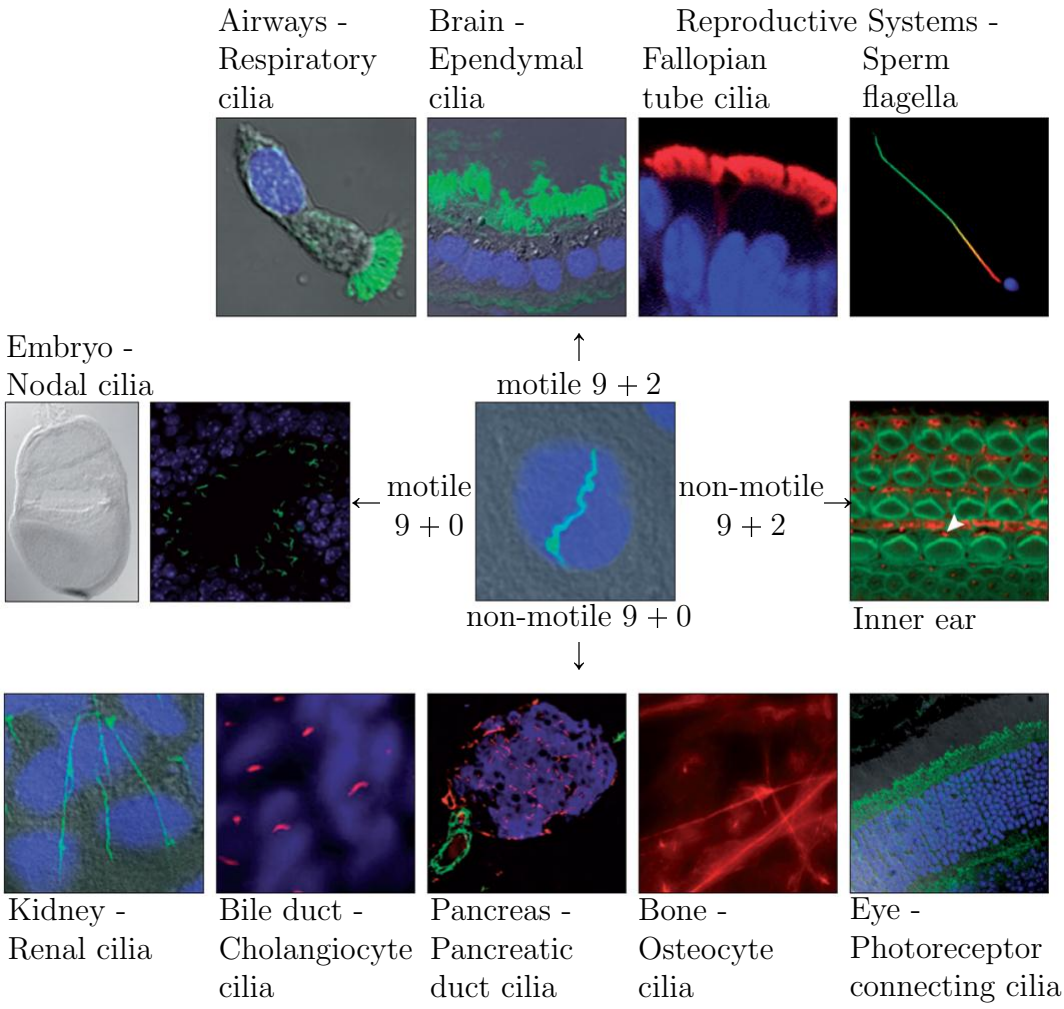

Figure 1.4: Ciliary dysfunction in human diseases. The centre panel shows a monociliated cell. Left panels show motile $9 + 0$ cilia found in the embryonic node that produce the nodal flow to break left-right symmetry of the body. Top panels show motile $9+2$ cilia that transport extracellular fluid along epithelial surfaces found on the respiratory epithelial cells, brain ependymal cells and epithelial cells lining the fallopian tubes [87]. Sperm flagella are elongated motile cilia that generate motility. The bottom panels show non-motile $9+0$ cilia that extend from most cells in the body and sense environmental signals. Well known examples are shown in the kidney and the bile duct [36] and pancreatic duct cilia [14]. The osteocyte cilia are thought to sense the amount of strain in bones whereas the connecting cilia in the photoreceptors of the eye connect the inner and outer segments. The right panel shows non-motile $9 + 2$ cilia found in the inner ear (kinocilium, red, arrowhead; stereocilia, green) [22]. Other than the four cilia types shown in this figure there are other types, for example the $9 + 4$ cilia found in the rabbit organising structure [26]. In all images, axonemes were stained red or green by indirect immunofluorescence and nuclei were also stained. Reprinted with permission from Nature Publishing Group, Fliegauf *et al.* [28] (2007), *Nature Reviews Molecular Cell Biology.*

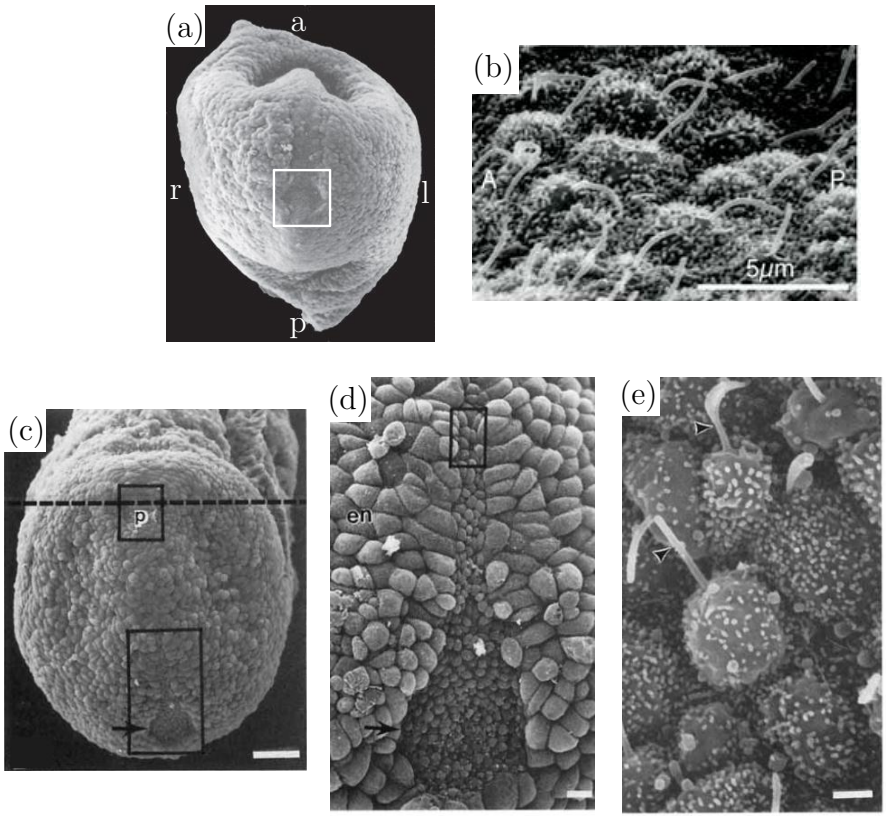

Figure 1.5: Mouse embryo and nodal cilia. (a) Low magnification view of a mouse embryo at 7.5 days post-fertilisation. The Reichert's membrane has been removed and the embryo is observed from the ventral side. The node is indicated by the white square. Reprinted with permission from Elsevier, Hirokawa *et al.* [34] (2006), *Cell.* (b) Scanning electron micrograph of cilia in the node viewed at approximately 30° from the horizontal. Reprinted with permission from Nonaka *et al.* [61] (2005), *PLoS Biology*, 3(8). (c) View of a mouse embryo from the ventral side, the node is indicated by an arrow. p, prechordal plate. (d) Magnification of the lower black rectangle in (c) showing the triangular shape of the node indicated by an arrow. en, endoderm. (e) Magnification of the black rectangle in (d), individual cilia are highlighted with an arrow. Panels (c,d,e) reprinted with permission from John Wiley and Sons, Sulik *et al.* [80] (1994), *American Journal of Anatomy.* Scale bars (c) 50 μm, (d) 10 μm, (e) 1 μm. Axis notation a,A anterior; p,P posterior; l, left and r, right.

ever, Sulik *et al.* reported that cilia in the mouse node were motile and that their motion played a part in establishing L-R axis asymmetry, 'an association with the establishment of sidedness' [80]. The discovery of motile cilia in the node by Sulik *et al.* provided the first support for the link between dynein mutation and *situs inversus.*

There have been recent reports [16, 49] that there are three different types of cilia

found in the mouse node, the $9+0$ and $9+2$ configurations described above and a novel $9+4$ configuration that has a duplication of the central pair of microtubules [26]. These three types of cilia in the mouse node are consistent with similar observations in rabbits [9, 26]. All types of cilia and indeed flagella, a related and great topic of interest, all share the basic internal structure of the *axoneme*. From here onwards cilia in an organising structure will be referred to as *nodal cilia*.

Nonaka *et al.* [60] confirmed, using video microscopy, that nodal cilia were motile and that their motion is a clockwise rotation when viewed from tip to base. Nonaka *et al.* also observed that these 'whirling' cilia drive a directional fluid flow in the node. Furthermore, Nonaka *et al.* showed that knockout mice, lacking the protein KIF3B, did not produce nodal cilia, subsequently did not break L-R symmetry normally, exhibiting morphological abnormalities including randomised L-R asymmetry and did not survive beyond midgestation, thus confirming the link between nodal cilia, organ positioning and *situs inversus*.

In 2002 to establish that a fluid flow in the node, termed a *nodal flow*, is sufficient for symmetry breaking Nonaka *et al.* [59] cultured mouse embryos in artificial flow conditions. Mouse embryos were dissected at 7.7 dpf and those that were between the late bud and late headfold stage of development were developed in the flow chamber for 14 hours before being subjected to conventional rotation culture for a further 32 hours bringing the embryos to approximately 9.5 dpf. After such time the embryos were delicately fixed and stained in the chamber before artificial flow was applied. In wildtype mice where cilia function normally, a weak ($5.7\,\mu\mathrm{ms}^{-1}$) or strong ($110\,\mu\mathrm{ms}^{-1}$) artificial leftward flow had no effect on the overall direction of flow in the node, whereas a strong rightward flow was able to reverse the flow direction and in those mice *situs inversus* was the result. However, a weak rightward flow was not sufficient to reverse the flow direction. Nonaka *et al.* also found that applying artificial flow to mutant embryos lacking nodal flow restored L-R asymmetric development. Applying artificial leftward flow to mutant embryos resulted in normal organ *situs* and an artificial rightward flow produced *situs inversus*. Impor-

tantly, the direction of the flow in wildtype embryos was always leftward regardless of the orientation of the embryo with respect to the chamber that the experiment took place in. Since no flow was observed in mutant embryos with immotile or missing cilia, it can be concluded that it is nodal cilia that drive the directional flow in the node. These experiments showed for the first time how fluid mechanics plays a significant role in L-R asymmetric development.

Recently, Hashimoto *et al.* [32] showed that as the mouse node develops it goes through a number of changes. There is a continual increase in the number of cilia as development advances, see figure 1.6 and cilia positions in the node also change, with there being a greater number located towards the posterior edge with a larger tilt angle towards the posterior direction also being observed. Hashimoto *et al.* observed that at early stages of development, 'late bud' ($\approx$ 7.5–8.0 dpf), each cilium has a small tilt angle towards either the posterior or anterior direction, depending on whether the cilium is closer to the posterior or anterior edge of the cell which it protrudes from. At this stage of development cilia are mainly located centrally on each cell. At mid stages of development, 'early headfold' ($\approx$ 7.5–8.0 dpf) and 'late headfold' ($\approx$ 8.0 dpf) stages, cilia are located in posterior regions of cells with increasing numbers giving a greater proportion that are tilted towards the posterior. Finally, for the latter stages of development that the node is present, '1 somite' and '3 somite' (both 8.0+ dpf) stages, cilia are found in posterior regions of cells with significant posterior tilt. The flow fields at each of these developmental stages as well as for a range of cilia parameters will be studied in chapter 5.

Cilia have been observed in similar organising structures to that of the mouse in other organisms, the Spemann's organiser in amphibians, the Hensen's node in birds and the Kupffer's vesicle in fish [38]. All of these are referred to as organising structures. However, whilst motile cilia and a fluid flow have been reported in both the chick and the frog, it is not the earliest observed L-R asymmetric event [9, 30, 50, 79]. Contrary to these two examples, the observed flow in the zebrafish organising structure is believed to be the earliest asymmetric event [9, 83] in the development cycle.

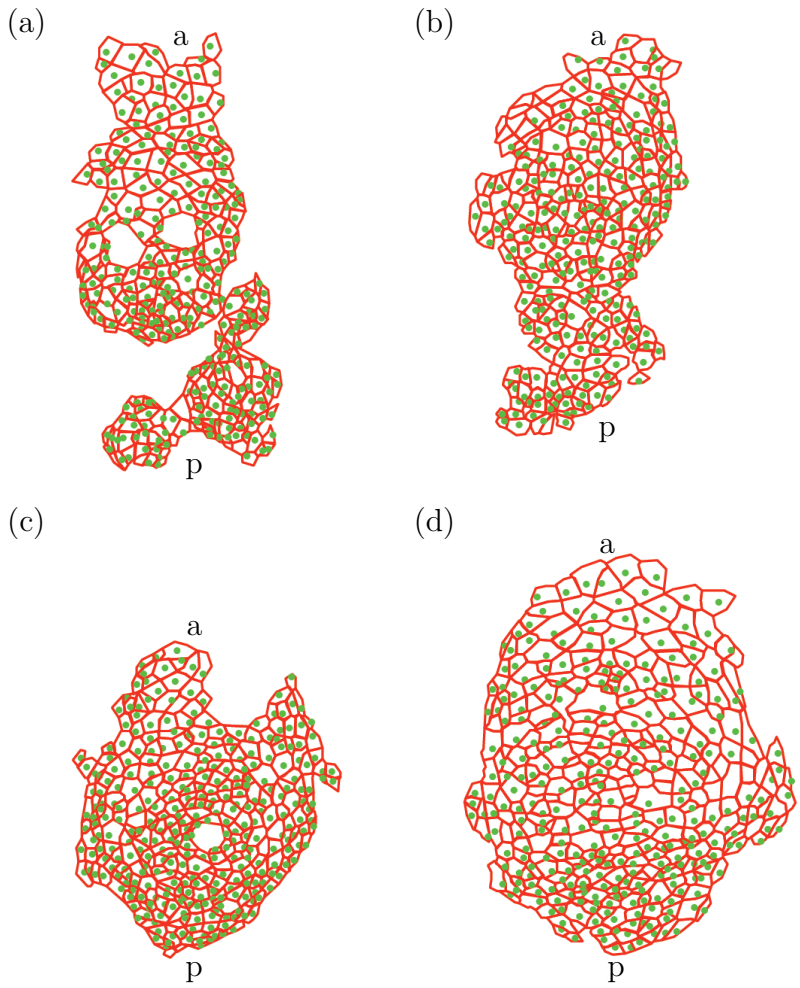

Figure 1.6: Reconstruction of node shape showing cilia positions (·) and cell boundaries (—) for (a) late bud (≈ 7.5–8.0 dpf), (b) early headfold (≈ 7.5–8.0 dpf), (c) late headfold (≈ 8.0 dpf) and (d) 3 somite (8.0+ dpf) stages of development. Reprinted with permission from Nature Publishing Group, Hashimoto *et al.* [32, Supp. Mat.] (2010), *Nature Cell Biology*. Axis notation a, anterior and p, posterior.

The zebrafish organising structure, termed the Kupffer's vesicle (KV), is a closed spheroidal structure measuring approximately 70 μm×60 μm×30 μm (L-R×A-P×D-V)[47] that forms at around 12 hours post-fertilisation [45], see figure 1.7(a,b,c), with the entire internal surface of the zebrafish KV being lined with cilia approximately 4 μm in length in wildtype embryos and 2–3 μm in mutant embryos [56]. At present both $9+0$ and $9+2$ cilia have been observed in KV [27] where some are motile and some are immotile, with the vast majority being motile cilia that perform a rotation similar to that observed of cilia in the mouse node.

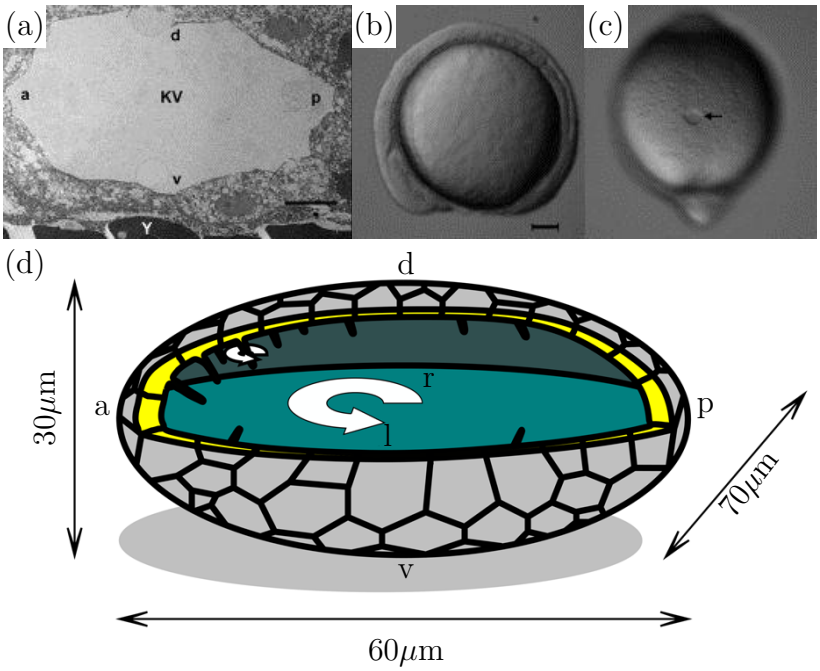

Figure 1.7: Zebrafish Kupffer's vesicle. (a) An electron micrograph of the zebrafish Kupffer's vesicle at 12 hours post-fertilisation. KV, Kupffer's vesicle; Y, yolk. Side (b) and tail (c) view of brightfield reconstructions of confocal data sets showing the Kupffer's vesicle at 12 hours post-fertilisation, the arrow in (c) indicates the Kupffer's vesicle. (d) Schematic of the zebrafish Kupffer's vesicle showing the cilia positions and their motion. Panels (a,b,c) reprinted with permission from John Wiley and Sons, Kreiling *et al.* [47] (2007), *Developmental Dynamics*. Panel (d) redrawn from Kreiling *et al.* [47]. Scale bars (a) 10 μm (b) 100 μm. Axis notation d, dorsal; v, ventral; a, anterior; p, posterior; l, left and r, right.

The observed flow in the zebrafish KV is an anti-clockwise swirl about the D-V axis that is faster from anterior to left than from posterior to right at the centre plane between the dorsal roof and ventral floor, see figure 1.8. However, there is not a consensus on the cilia mechanism used to produce such a flow. Supatto *et al.* [81] suggest a dorsal tilt of 'equatorial' cilia, treating the spheroid as a globe with the dorsal roof and ventral floor being similar to the north and south poles respectively, whereas Kreiling *et al.* [47] suggest that cilia on the roof and the floor are tilted towards the posterior direction. Kreiling *et al.* also report an asymmetric cilia distribution with respect to the A-P and D-V axes, with a greater proportion of cilia in the D-A 'corner'. Recent observations by Lopes and Rua *et al.* [personal communication] have shown that there are multiple cilia beat frequencies and these frequencies are different for wildtype and mutant zebrafish

embryos. Initially, the problem of cilium tilt direction and distribution in the KV will be investigated in chapter 6 followed by the impact of cilia length and rotation mechanisms on the fluid flow. The impact of cilium rotation mechanisms by multiple beat frequencies is currently being investigated in collaboration with Lopes and Rua *et al.* and will also be discussed in chapter 6.

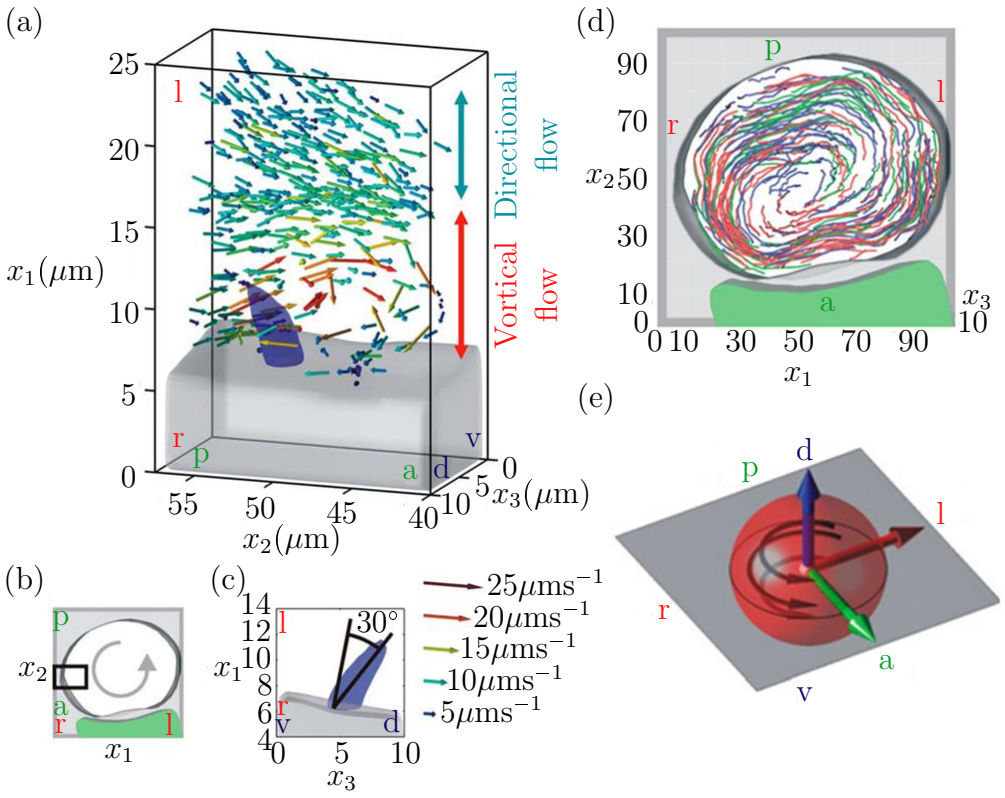

Figure 1.8: Experimental observations of the flow inside the zebrafish Kupffer's vesicle reprinted with permission from Elsevier, Supatto *et al.* [81] (2008), *Biophysical Journal*. (a) Dorsal view of the measured fluid velocity about a single cilium located on the right side of a Kupffer's vesicle. The velocity magnitude is represented by arrow length that has been extracted from three-dimensional particle tracking data showing the transition from vortical flow close to the cilium to directional flow above the cilium. (b) General flow pattern in the AP-LR plane. The black box shows the position of the flow in the vesicle given in (a). (c) Posterior view showing a 30° dorsal tilt of the beating axis. (d) Particle tracks showing the steady-state flow around the inside of a Kupffer's vesicle where the three different track colors show flows taken at three separate 15 second time intervals. The tracks indicate that the steady-state flow is a swirl about the D-V axis. (e) Schematic of the flow observed inside a Kupffer's vesicle represented with an arrow. Axis notation d, dorsal; v, ventral; a, anterior; p, posterior; l, left and r, right.

While the experiments of Nonaka *et al.* [59, 60] on mice linked directional flow with

L-R asymmetric development they also raised questions. Firstly, it was not known how each cilium consistently rotates clockwise. Brokaw [10, 11] studied this question in great detail and has proposed a number of possible answers. Via computer simulations, Brokaw assessed two main mechanisms. The first of which is that the dynein arms (see figure 1.3) on doublet N are regulated by the sliding velocities of doublets N and $N+1$. Doublets are labelled anticlockwise round the axoneme when viewing from tip to base. This means the dynein on doublet N is activated before the dynein on doublet $N-1$, interpreted as a clockwise propogation of dynein from one doublet to the next, when viewed from tip to base. However, there is no known mechanism for such dynein activity leading Brokaw to propose that an off-axis component of dynein force produces a right-handed twist in the axoneme. This comes from observations in Chlamydomonas and Tetrahymena [42, 88] where dynein can cause microtubules to rotate and translocate, meaning dynein could potentially produce a twist and initiate clockwise rotations in nodal cilia. Brokaw [10] concluded that the second mechanism was more likely and that once a rotation direction is determined it remains. An answer to the question of rotation direction is still under active investigation.

Another question arising from the experimental observations is how a clockwise rotation drives a directional fluid flow. A resolution to this question was first given by Cartwright *et al.* [15] whereby it was proposed that rotating cilia need to be tilted towards the already-established posterior direction to give a leftward flow. This prediction was confirmed experimentally by Okada *et al.* [65] and in a scaled mechanical model by Nonaka *et al.* [61] using copper wires to represent nodal cilia. The copper wires were tilted by different angles and rotated to find the optimum configuration for maximum flow. Nonaka *et al.* found that the velocity of the fluid was dependent on the tilt angle, with a faster flow being generated by larger tilt angles and no directional flow when the tilt angle is zero.

The third question to come out of the experimental observations is how a fluid flow initiates L-R asymmetric development. This question remains unanswered but there are

currently two main views on this subject. The first is that a morphogen gradient is established across the node [12] where the concentration of a molecule is higher on one side than it is on the other [60, 64]. To support this mechanism 'nodal vesicular parcels' (NVPs), membrane enclosed particles containing morphogens, have been viewed in the node by Tanaka *et al.* [85] being transported by the nodal flow. Because the node is a closed domain anything transported leftward must be returned rightward due to mass conservation. This creates the potential problem of a uniform distribution of NVPs which would not initiate asymmetric development unless there was, for example, an inactivation time for NVPs or possibly that the NVPs are ruptured at the 'left' of the node and not the 'right' [85]. The other mechanism proposed is that there are two distinct groups of nodal cilia, one motile group that generate the fluid flow and one immotile group that 'sense' the flow. Such a model is referred to as a 'two-cilia model' [84] and is supported by observations of immotile cilia on the walls of the mouse node [57]. It is not clear which mechanism is used to interpret the fluid flow in the node or if it is even one of these or a combination. In all the species that are currently being studied it is not clear how the fluid flows are interpreted and a model of the organising structures and the fluid flows found inside them will help to gain further understanding of the mechanisms involved in initiating L-R asymmetric development.

The work presented in this thesis concentrates on the generation of fluid flows in organising structures by the action of rotating cilia rather than the mechanisms used to interpret the flows that initiate the downward cascade of information that results in L-R asymmetric development, as the precise mechanism remains unknown [72]. In recent years there have been many models of the mouse node but none of the zebrafish KV, some of which use singularity methods and a few that do not. To discuss the types of flow found in the node the singularities of Stokes flow will first be reviewed in chapter 2 along with regularised and integral representations of singularities. This is followed by a review of singularity and geometric models of the mouse node in chapter 3. The action of a cilium can be represented using a line distribution of singularities via slender body theory which

will be discussed in chapter 4 leading to a computational model of the embryonic mouse node in chapter 5 that includes the covering membrane; this model is applied to many different cilia configurations and developmental stages. A computational model of the zebrafish KV is developed in chapter 6 using a mesh of the entire domain for the first time and is used to gain further insight into the two reported cilium tilt directions and distributions in the KV as well as other observed cilia mechanisms. Each chapter will be summarised leaving chapter 7 for a general discussion of the entire work and its findings.

CHAPTER 2

FLUID MECHANICS TECHNIQUES

2.1 Introduction

In this chapter the singular solutions to Stokes' equations for both an infinite fluid and in the presence of a plane boundary along with derivatives of these solutions will be reviewed. These singular solutions can be used to gain an initial insight into fluid flows by analysing the type of flow each singularity generates. The theory of regularised Stokeslets for infinite and semi-infinite domains will also be reviewed and the boundary integral equation for Stokes flow problems for standard and regularised singularities will be discussed.

2.2 Stokes flow and singularity solutions

The motion of an incompressible fluid is described by the Navier-Stokes equations

$$\rho\frac{\partial \boldsymbol{u}}{\partial t} + \rho\boldsymbol{u}\cdot\nabla\boldsymbol{u} = -\nabla p + \mu\nabla^2\boldsymbol{u} + \boldsymbol{f} \quad \text{and} \quad \nabla\cdot\boldsymbol{u} = 0, \tag{2.1}$$

where ρ is the constant density of the fluid, μ is dynamic viscosity, p is pressure, $\boldsymbol{u}$ is velocity, t is time and $\boldsymbol{f}$ represents any body forces, for example gravity or electromagnetic

forces. The Navier-Stokes equations (2.1) can be written in dimensionless form as

$$\mathrm{Re}\left(\frac{\partial \boldsymbol{u}}{\partial t} + \boldsymbol{u}\cdot\nabla\boldsymbol{u}\right) = -\nabla p + \nabla^2\boldsymbol{u} + \boldsymbol{f} \quad \text{and} \quad \nabla\cdot\boldsymbol{u} = 0, \tag{2.2}$$

where $\mathrm{Re} = \rho U L/\mu$ is the Reynolds number with U and L being characteristic velocity and length scales respectively. A high Reynolds number, $\mathrm{Re} \gg 1$, corresponds to when inertial forces dominate over viscous forces whereas a low Reynolds number, $\mathrm{Re} \ll 1$, corresponds to when viscous forces dominate over inertial forces. An embryonic node typically has $L \approx \mathcal{O}(100)\,\mu\mathrm{m}$ and $U \approx \mathcal{O}(1\text{–}10)\,\mu\mathrm{ms}^{-1}$ giving $\mathrm{Re} \approx \mathcal{O}(10^{-4}\text{–}10^{-3}) \ll 1$ assuming the fluid is water at approximately room temperature meaning the node is a low Reynolds number system.

In low Reynolds number flows mixing is very different to what would be familiar in every day life. Turbulent mixing can play no role as turbulence does not occur in this regime and the observed flows are brought about by chaotic advection [15, 66], giving rise to two important features; advection and diffusion. Advection is characterised on a time scale given by $\tau_a = L/U$ and for $L = 50\,\mu\mathrm{m}$ and $U = 10\text{–}50\,\mu\mathrm{ms}^{-1}$, $\tau_a = 1\text{–}5\,\mathrm{s}$. Similarly, a diffusion timescale, is given by $\tau_d = L^2/D$ where $D = 10\text{–}100\,\mu\mathrm{m}^2\mathrm{s}^{-1}$ is a typical diffusion coefficient for biological macromolecules [15], $\tau_d = 25\text{–}250\,\mathrm{s}$. The ratio of these timescales is defined as the Péclet number given by $\mathrm{Pe} = \tau_d/\tau_a = LU/D$ showing the relative importance of advection and diffusion for transport in a fluid flow. Here, $\mathrm{Pe} = 5\text{–}250$, which is greater than unity meaning advection is important, but not so much greater than unity that diffusion is unimportant. Therefore, morphogen transport is an advection-diffusion system.

Low Reynolds number flows can be accurately represented in the zero Reynolds number limit of (2.2). Taking this limit and restoring dimensions gives Stokes' equations for an incompressible fluid

$$\nabla p = \mu\nabla^2\boldsymbol{u} + \boldsymbol{f} \quad \text{and} \quad \nabla\cdot\boldsymbol{u} = 0. \tag{2.3}$$

For exterior unbounded flows, Stokes' equations are required to satisfy that $\boldsymbol{u}$ and p

approach a constant as $|\boldsymbol{x}|$ tends to infinity [48]. When N body forces are located at discrete points, $\boldsymbol{x}_p$, the force per unit length is given by $\boldsymbol{f} = \sum_{p=1}^{N} \boldsymbol{F}_p \delta(\boldsymbol{x}_p)$ where $\delta(\boldsymbol{x}_p)$ is the Dirac delta function. For a force located at a single point, $\boldsymbol{x}_p = \boldsymbol{y}$, Stokes' equations in an infinite fluid can be solved using three-dimensional Fourier and inverse Fourier transforms. The Fourier transform decouples the velocity from the pressure and the inverse Fourier transform gives

$$\left.\begin{aligned} u_i(\boldsymbol{x}) &= \frac{F_j}{8\pi\mu}\left(\frac{\delta_{ij}}{r} + \frac{r_i r_j}{r^3}\right) = \frac{1}{8\pi\mu} S_{ij}(\boldsymbol{x},\boldsymbol{y}) F_j, \\ p(\boldsymbol{x}) &= \frac{F_j r_j}{4\pi r^3}, \end{aligned}\right\} \tag{2.4}$$

where the Einstein summation convention is used for repeated indices here and throughout, $r = (r_1^2 + r_2^2 + r_3^2)^{1/2}$ is the distance between points $\boldsymbol{x}$ and $\boldsymbol{y}$ where $r_i = x_i - y_i$ and the second rank tensor, $S_{ij}(\boldsymbol{x},\boldsymbol{y})$, is termed a *Stokeslet*. The Stokeslet has an associated third rank tensor, $T_{ijk}(\boldsymbol{x},\boldsymbol{y}) = -6 r_i r_j r_k / r^5$, such that the stress tensor is given by

$$\sigma_{ik}(\boldsymbol{x}) = -\frac{3F_j}{4\pi}\frac{r_i r_j r_k}{r^5} = \frac{1}{8\pi} T_{ijk}(\boldsymbol{x},\boldsymbol{y}) F_j. \tag{2.5}$$

2.3 Higher order and other singularities

To obtain higher order singularities the gradient of the infinite domain Stokes flow solution $(2.4)_1$ is taken in a chosen direction to give a stokes-doublet, $H_{ijk}(\boldsymbol{x},\boldsymbol{y})$, of arbitrarily chosen strength C_{jk},

$$u_i^{\mathrm{SD}}(\boldsymbol{x}) = \frac{C_{jk}}{8\pi\mu}\left[\left\{-\frac{r_i\delta_{jk}}{r^3} + \frac{3r_i r_j r_k}{r^5}\right\} + \left\{\frac{r_k\delta_{ij} - r_j\delta_{ik}}{r^3}\right\}\right] = \frac{1}{8\pi\mu} H_{ijk}(\boldsymbol{x},\boldsymbol{y}) C_{jk}. \tag{2.6}$$

The part of the stokes-doublet in (2.6) that is symmetric in jk is termed a *stresslet* and the antisymmetric part is termed a *rotlet*. A stresslet represents the straining motion of the velocity field and a rotlet represents the rotational motion.

For a rotlet with the rotational strength defined as

$$\Omega_i = -\varepsilon_{ijk} C_{jk} \tag{2.7}$$

where ε_{ijk} is the Levi-Civita symbol, the contribution to the velocity field in an infinite fluid can be written as [6]

$$\boldsymbol{u}^{\mathrm{R}} = \frac{\boldsymbol{\Omega} \wedge \boldsymbol{r}}{8\pi\mu r^3}. \tag{2.8}$$

Taking the Laplacian of the infinite domain Stokeslet $(2.4)_1$, scaled by viscosity, gives the source-doublet in an infinite fluid domain

$$D_{ij}(\boldsymbol{x}, \boldsymbol{y}) = \mu \nabla^2 S_{ij}(\boldsymbol{x}, \boldsymbol{y}) = -\frac{1}{4\pi} \left(\frac{\delta_{ij}}{r^3} - \frac{3 r_i r_j}{r^5} \right). \tag{2.9}$$

The source-doublet is used to satisfy the no-slip boundary condition in the formulation of slender body theory and will be discussed further in chapter 4.

2.4 Singularities near a plane boundary

The solution to Stokes' equations due to a point force in the presence of a plane boundary was first derived using Fourier transforms by Blake [7] wherein full details can be found; only an outline is presented here. The velocity, u_i^*, and pressure, p^*, fields are each made up of two contributions, $u_i^* = u_i + v_i$ and $p^* = p + q$ respectively where u_i and p are the solutions for an infinite fluid domain given by (2.4). To solve for v_i and q an image Stokeslet is placed in the boundary such that $\boldsymbol{v}$ will contain the image Stokeslet and higher order singularities to satisfy the no-slip boundary condition on the plane. The velocity and pressure, v_i and q, must then satisfy

$$\nabla q = \mu \nabla^2 \boldsymbol{v} \quad \text{and} \quad \nabla \cdot \boldsymbol{v} = 0. \tag{2.10}$$

Equation (2.10) must satisfy the no-slip boundary condition, $\boldsymbol{u}(S) + \boldsymbol{v}(S) = 0$, where S is the set of all points on the boundary. The point force located in the boundary at the image point is taken to have the same magnitude but opposite sign to the point force located in the fluid and the plane boundary is at $x_3 = 0$, see figure 2.1. Equation (2.10) is

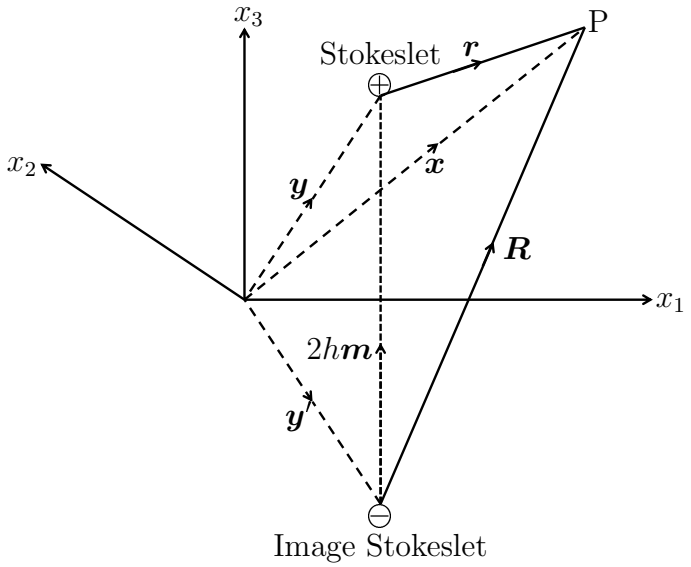

Figure 2.1: The position of a Stokeslet $\oplus$ in a fluid and its image counterpart $\ominus$ in the plane boundary. The plane boundary, S, is located at $x_3 = 0$ and the point P is at $\boldsymbol{x} = (x_1, x_2, x_3)$ with a Stokeslet at $\boldsymbol{y} = (y_1, y_2, h)$ and an image Stokeslet at $\boldsymbol{y}' = (y_1, y_2, -h)$. The Stokeslet and point P are related by $\boldsymbol{r} = \boldsymbol{x} - \boldsymbol{y}$ and the image Stokeslet and point P are related by $\boldsymbol{R} = \boldsymbol{x} - \boldsymbol{y}'$. The two Stokeslet positions are related by $2h\boldsymbol{m}$ where $\boldsymbol{m} = \boldsymbol{e}_3 = (0, 0, 1)$. Redrawn from Blake [7].

solved using Fourier transforms [7, 25, 48, 78] and the velocity, $\boldsymbol{u}^* = \boldsymbol{u} + \boldsymbol{v}$, and pressure, $p^* = p + q$, fields due to a point force in the j-direction, F_j, in the presence of a plane boundary at $x_3 = 0$ are,

$$\left.\begin{aligned} u_i^*(\boldsymbol{x}) =& \frac{F_j}{8\pi\mu}\left[\frac{\delta_{ij}}{r} + \frac{r_i r_j}{r^3} - \frac{\delta_{ij}}{R} - \frac{R_i R_j}{R^3} + 2h\Delta_{jk}\frac{\partial}{\partial R_k}\left(\frac{hR_i}{R^3} - \frac{\delta_{i3}}{R} - \frac{R_i R_3}{R^3}\right)\right] \\ =& \frac{1}{8\pi\mu} B_{ij}(\boldsymbol{x}, \boldsymbol{y}) F_j, \\ p^*(\boldsymbol{x}) =& \frac{F_j}{4\pi}\left[\frac{r_j}{r^3} - \frac{R_j}{R^3} - 2h\Delta_{jk}\frac{\partial}{\partial R_k}\left(\frac{R_3}{R^3}\right)\right], \end{aligned}\right\} \tag{2.11}$$

where Δ_{jk} takes value 1 for $j = k = 1, 2$, value -1 for $j = k = 3$ and zero otherwise. The tensor, $B_{ij}(\boldsymbol{x}, \boldsymbol{y})$, denotes the Green's function tensor for the Stokes flow equations near a no-slip plane boundary at $x_3 = 0$. The point force in the fluid is located at $\boldsymbol{y} = (y_1, y_2, h)$ and the image in the boundary at $\boldsymbol{y}' = (y_1, y_2, -h)$ with r defined as before and $R = (R_1^2 + R_2^2 + R_3^2)^{1/2}$ where $R_i = x_i - y_i'$.

For $r \ll h$ the near-field solution is well approximated by a Stokeslet in an infinite fluid $(2.4)_1$. In contrast, the far-field is considerably modified due to the presence of the plane boundary at $x_3 = 0$. This is because the Stokeslet image system is made up of a Stokeslet $\mathcal{O}(1/r)$, stokes-doublet $\mathcal{O}(1/r^2)$ and a source-doublet $\mathcal{O}(1/r^3)$. When a Stokeslet is parallel to the plane boundary the far-field is well approximated by a combination of stresslets. The combination of stresslets arises because the antisymmetric contributions from the two stokes-doublets cancel leaving the symmetric stresslet, shown in figure 2.2(a). However, when a Stokeslet is perpendicular to the plane boundary the two stokes-doublets have opposite signs and cancel giving a stokes-quadrupole far-field. Because the stokes-quadrupole has the same order of magnitude as a source-doublet the far-field is given as a combination of a stokes-quadrupole and a source-doublet [7], shown in figure 2.2(b).

As a cilium rotates it is far from the surface for a portion of the rotation, termed the effective stroke, and is close to the surface for the rest of the rotation cycle, termed the recovery stroke. Both of these cases can be physically interpreted using the Stokeslet image system (2.11) and the singularity representations in figure 2.2 and are shown diagrammatically in figure 2.3.

Figure 2.3(a) shows the effective stroke and highlights the three 'zones of influence'. For a cilium of length l, the inner-field, $r \ll l$, velocity field is $\mathcal{O}(\log r)$ which can be shown by integrating a Stokeslet and source-doublet distribution, as shown by Lighthill [51]. The near-field, $r \sim l$, velocity decays as $\mathcal{O}(1/r)$ because it is dominated by a Stokeslet field. The far-field, $r \gg l$, velocity decays as $\mathcal{O}(1/r^2)$ because the Stokeslet and image system are approximated by a symmetric stokes-doublet resulting in a stresslet.

Figure 2.3(b) shows the 'zones of influence' for the recovery stroke. Because the cilium

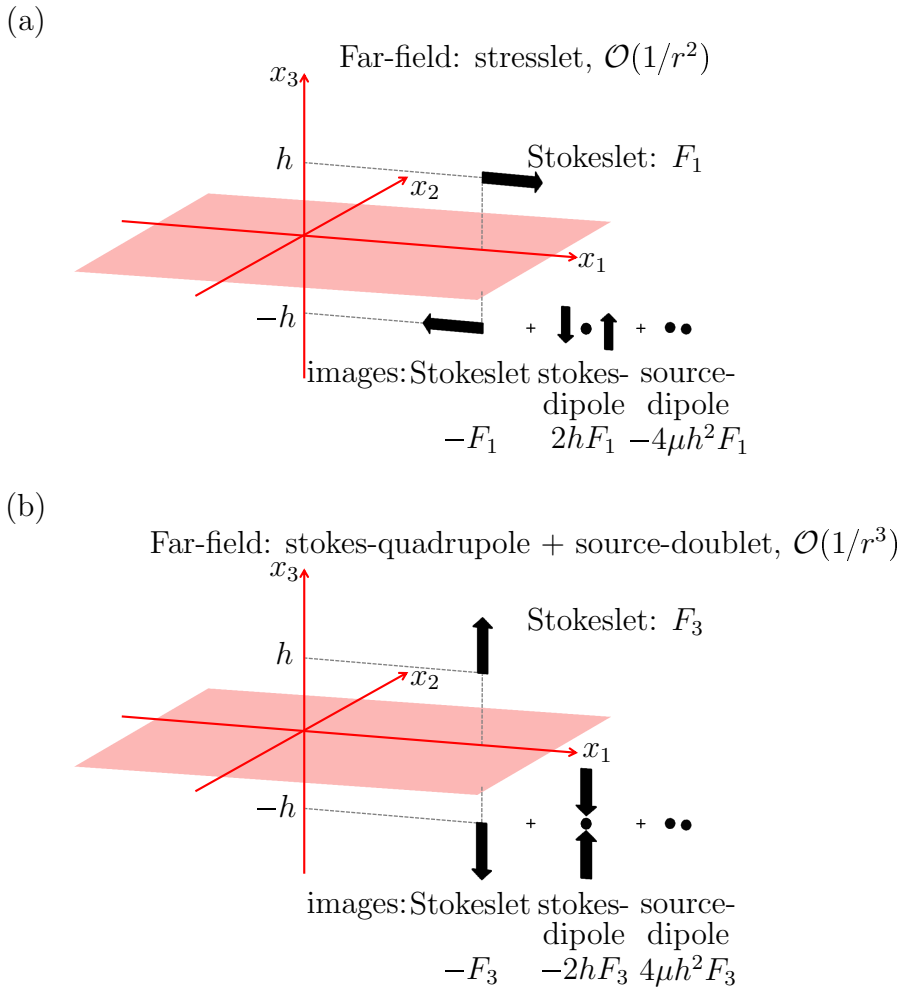

Figure 2.2: Diagrams representing the image system for Stokeslets (a) parallel ($j = 1$) and (b) perpendicular ($j = 3$) to the plane boundary. The strengths of each singularity are given. Redrawn from Blake [7].

is close to the surface, the volume of fluid in the near-field is greatly reduced. This results in particles moving in a 'loopy drift' because the volume of fluid is exposed to a relatively strong $\mathcal{O}(1/r)$ field during the effective stroke but an $\mathcal{O}(1/r^2)$ field during the recovery stroke. Particles far from the surface experience a stresslet field during the effective and recovery strokes, with the effective stroke field being stronger as the stresslet strength is proportional to the distance from the surface. These predictions are for a semi-infinite domain and the inclusion of an overlying membrane is expected to alter the flows due to mass conservation. These considerations here however provide a good initial insight.

A rotlet in the presence of a plane boundary can be found in a similar way to that of

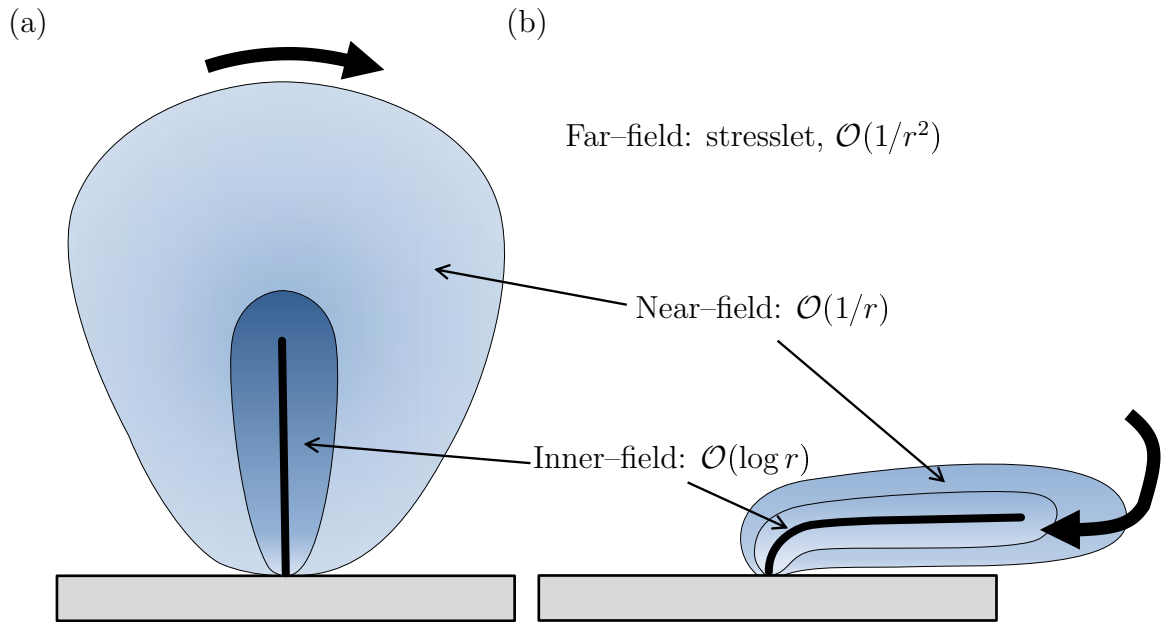

Figure 2.3: The 'zones of influence' for (a) the effective stroke and (b) the recovery stroke. The inner-, near- and far-fields decay differently depending on the distance, r, from a cilium of length l. The inner-field corresponds to $r \ll l$, near-field $r \sim l$ and far-field $r \gg l$. Reprinted with permission from Springer, Smith *et al.* [77] (2011), *Journal of Engineering Mathematics*.

the Stokeslet [8] and is given by

$$u_i(\boldsymbol{x}) = \frac{\Omega_j}{8\pi\mu}\left[\frac{\varepsilon_{ijk}r_k}{r^3} - \frac{\varepsilon_{ijk}R_k}{R^3} + 2\varepsilon_{kj3}\left(\frac{\delta_{ik}h}{R^3} - \frac{3hR_iR_k}{R^5} + \frac{3R_iR_kR_3}{R^5}\right)\right]. \tag{2.12}$$

For the components of $\boldsymbol{\Omega}$ parallel to the plane boundary ($j = 1, 2$), the dominant far-field behaviour of the image system rotlet, (2.12), is a stresslet. This is because the image system is made up of a rotlet, $\mathcal{O}(1/r^2)$, stresslet, $\mathcal{O}(1/r^2)$, and source-doublet, $\mathcal{O}(1/r^3)$. This results in a straining motion in the far-field with radial streamlines. For the component of $\boldsymbol{\Omega}$ perpendicular to the boundary ($j = 3$), the far-field behaviour of (2.12) is a rotlet-doublet because when $j = 3$ only the rotlet contribution to the image system remains as $\varepsilon_{k33} = 0$ for all k.

The source-doublet image system is not considered here because the contributions to satisfy the no-slip boundary condition all decay rapidly, $\mathcal{O}(1/r^3)$ [8].

2.5 Regularised Stokeslets

The method of *regularised Stokeslets* was first introduced and developed by Cortez *et al.* [20, 21]. The technique is based upon the superposition of exact solutions to Stokes' equations (2.3) with the force, $\boldsymbol{f}$, being given by a smooth approximation to a Dirac delta function termed a *cut-off function*. This produces a modified Stokeslet solution, namely a regularised Stokeslet, for which the singularity has been removed for non-zero regularisation whilst maintaining that the divergence of velocity is zero.

Cortez [20] demonstrated that for the case of forces spread over a ball centred at $\boldsymbol{y}$ that the force is given by $\boldsymbol{f} = \boldsymbol{F}\psi_\epsilon(\boldsymbol{x}-\boldsymbol{y})$, where $\psi_\epsilon(\boldsymbol{x})$ is a cut-off function concentrated at $\boldsymbol{x} = \boldsymbol{0}$ satisfying $\int \psi_\epsilon(\boldsymbol{x})\mathrm{d}\boldsymbol{x} = 1$. The regularisation parameter, ϵ, controls the level of spreading of the cut-off function, see figure 2.4, and for computations is typically less than unity and physically gives the extent of the region that the force applies. When $\boldsymbol{f} = \boldsymbol{F}\psi_\epsilon(\boldsymbol{x}-\boldsymbol{y})$, Stokes' equations become

$$\nabla p^\epsilon = \mu\nabla^2\boldsymbol{u}^\epsilon + \boldsymbol{F}\psi_\epsilon(\boldsymbol{x}-\boldsymbol{y}) \quad \text{and} \quad \nabla\cdot\boldsymbol{u}^\epsilon = 0, \tag{2.13}$$

where p^ϵ is a regularised pressure and $\boldsymbol{u}^\epsilon$ a regularised velocity. Both two- and three-dimensional problems can use either a cut-off function of exponential form or from the family $\psi_\epsilon^n(\boldsymbol{x}) = C_n\epsilon^{2(n-1)}/(4\pi(|\boldsymbol{x}|^2+\epsilon^2)^{(2n+1)/2})$ where C_n are constants calculated from $\int \psi_\epsilon(\boldsymbol{x})\mathrm{d}\boldsymbol{x} = 1$ and $n \geqslant 2$ [20].

When $\boldsymbol{x}$ is close to $\boldsymbol{y}$, the absolute value of the Stokeslet tensor, $|S_{ij}(\boldsymbol{x},\boldsymbol{y})|$, is large, similarly $|S_{ij}(\boldsymbol{x},\boldsymbol{y})|$ tends to infinity as $\boldsymbol{x}$ tends to $\boldsymbol{y}$. In this case a velocity given by $(2.4)_1$ is also large for non-zero F_j making accurate evaluation of $(2.4)_1$ difficult using numerical quadrature. By using a regularised Stokeslet the singularity is removed and evaluation is possible even when $\boldsymbol{x} = \boldsymbol{y}$. Solutions are well defined for all $\boldsymbol{x}$ in $\mathbb{R}^3$ even in cases when the forces are located along curves or at discrete points instead of on a closed surface [20].

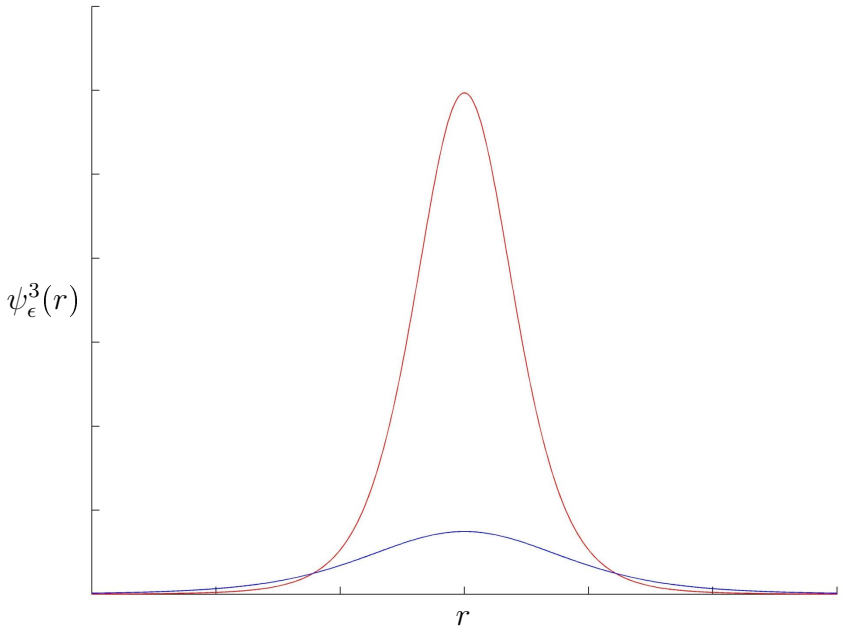

Figure 2.4: An example cut-off function $\psi^3_\epsilon(r) = 15\epsilon^4/(8\pi(r^2+\epsilon^2)^{7/2})$ where $r = |\boldsymbol{x}|$ for $n = 3$, $\epsilon = 0.1$ (—) and $\epsilon = 0.2$ (—) centred about $r = 0$.

As for singular solutions the velocity solution takes the form

$$u_i^\epsilon(\boldsymbol{x}) = \frac{1}{8\pi\mu} S_{ij}^\epsilon(\boldsymbol{x},\boldsymbol{y}) F_j \tag{2.14}$$

where $S_{ij}^\epsilon(\boldsymbol{x},\boldsymbol{y})$ is a regularised Stokeslet. A regularised Stokeslet is associated with a regularised pressure and stress tensor given by

$$p^\epsilon(\boldsymbol{x}) = \frac{1}{8\pi} P_j^\epsilon(\boldsymbol{x},\boldsymbol{y}) F_j \quad \text{and} \quad \sigma_{ik}^\epsilon(\boldsymbol{x}) = \frac{1}{8\pi} T_{ijk}^\epsilon(\boldsymbol{x},\boldsymbol{y}) F_j. \tag{2.15}$$

The tensors $P_j^\epsilon(\boldsymbol{x},\boldsymbol{y})$ and $T_{ijk}^\epsilon(\boldsymbol{x},\boldsymbol{y})$ are given by $P_j^\epsilon(\boldsymbol{x},\boldsymbol{y}) = 8\pi\partial G_\epsilon(\boldsymbol{x}-\boldsymbol{y})/\partial x_j$ and $T_{ijk}^\epsilon(\boldsymbol{x},\boldsymbol{y}) = -\delta_{ik}P_j^\epsilon(\boldsymbol{x},\boldsymbol{y}) + \partial S_{ij}^\epsilon(\boldsymbol{x},\boldsymbol{y})/\partial x_k + \partial S_{kj}^\epsilon(\boldsymbol{x},\boldsymbol{y})/\partial x_i$ respectively. The function $G_\epsilon(\boldsymbol{x})$ satisfies $\nabla^2 G_\epsilon(\boldsymbol{x}) = \psi_\epsilon(\boldsymbol{x})$ and $\nabla^2 B_\epsilon(\boldsymbol{x}) = G_\epsilon(\boldsymbol{x})$ where $B_\epsilon(\boldsymbol{x})$ and $G_\epsilon(\boldsymbol{x})$ are smooth approximations to the Green's functions that satisfy $\nabla^2 G(\boldsymbol{x}) = \delta(\boldsymbol{x})$, $\nabla^2 B(\boldsymbol{x}) = G(\boldsymbol{x})$ [17, 20]. Combining (2.14) and (2.15) with $(2.13)_1$ gives,

$$\nabla^2 S_{ij}^\epsilon(\boldsymbol{x},\boldsymbol{y}) - \frac{\partial P_j^\epsilon(\boldsymbol{x},\boldsymbol{y})}{\partial x_i} = -8\pi\delta_{ij}\psi_\epsilon(\boldsymbol{x}-\boldsymbol{y}) \tag{2.16}$$

where δ_{ij} is the Kronecker delta. Combining (2.14) with $(2.13)_2$ gives

$$\frac{\partial S_{ij}^{\epsilon}(\boldsymbol{x},\boldsymbol{y})}{\partial x_i} = 0. \tag{2.17}$$

By (2.16) the regularised Stokeslet can be given by

$$S_{ij}^{\epsilon}(\boldsymbol{x},\boldsymbol{y}) = 8\pi\left(\frac{\partial^2 B_{\epsilon}(\boldsymbol{x}-\boldsymbol{y})}{\partial x_i \partial x_j} - \delta_{ij} G_{\epsilon}(\boldsymbol{x}-\boldsymbol{y})\right) \tag{2.18}$$

which satisfies (2.17) exactly. Writing the regularised Stokeslet as in (2.18) means that $S_{ij}^{\epsilon}(\boldsymbol{x},\boldsymbol{y})$ can be determined from any cut-off function, $\psi_{\epsilon}(\boldsymbol{x})$, after first calculating $G_{\epsilon}(\boldsymbol{x})$ and $B_{\epsilon}(\boldsymbol{x})$ using the above relations.

The regularised pressure, Stokeslet and stress tensor depend completely on the choice of cut-off function. For the remainder of this work, the cut-off function used will be $\psi_{\epsilon}^3(r)$ with $C_3 = 15/2$ [20],

$$\psi_{\epsilon}(r) = \psi_{\epsilon}^3(r) = \frac{15\epsilon^4}{8\pi\left(r^2+\epsilon^2\right)^{7/2}}, \tag{2.19}$$

see figure 2.4. For this choice of cut-off function $G_{\epsilon}(r)$ and $B_{\epsilon}(r)$ are calculated to be

$$G_{\epsilon}(r) = -\frac{1}{8\pi}\frac{2r^2+3\epsilon^2}{(r^2+\epsilon^2)^{3/2}} \quad \text{and} \quad B_{\epsilon}(r) = -\frac{1}{8\pi}(r^2+\epsilon^2)^{1/2}. \tag{2.20}$$

The regularised pressure, Stokeslet and stress tensor then follow as

$$P_j^{\epsilon}(\boldsymbol{x},\boldsymbol{y}) = r_j \frac{2r^2+5\epsilon^2}{(r^2+\epsilon^2)^{5/2}}, \tag{2.21}$$

$$S_{ij}^{\epsilon}(\boldsymbol{x},\boldsymbol{y}) = \delta_{ij}\frac{r^2+2\epsilon^2}{(r^2+\epsilon^2)^{3/2}} + \frac{r_i r_j}{(r^2+\epsilon^2)^{3/2}}, \tag{2.22}$$

$$T_{ijk}^{\epsilon}(\boldsymbol{x},\boldsymbol{y}) = -6\frac{r_i r_j r_k}{(r^2+\epsilon^2)^{5/2}} - 3\epsilon^2\frac{\left[r_i\delta_{jk}+r_j\delta_{ik}+r_k\delta_{ij}\right]}{(r^2+\epsilon^2)^{5/2}}, \tag{2.23}$$

where r and r_i are defined as in (2.4).

Ainley *et al.* [4] derived the regularised image system formulation by analysing combinations of regularised singularities in the presence of a plane boundary at $x_1 = 0$ until the no-slip boundary condition was satisfied. Smith [74] rewrote the Ainley *et al.* formulation

in index notation for a plane boundary at $x_3 = 0$ finding it to be

$$B_{ij}^{\epsilon}(\boldsymbol{x},\boldsymbol{y}) = \frac{\delta_{ij}(r^2+2\epsilon^2)+r_i r_j}{r_\epsilon^3} - \frac{\delta_{ij}(R^2+2\epsilon^2)+R_i R_j}{R_\epsilon^3} + 2h\Delta_{jk}\left[\frac{\partial}{\partial R_k}\left(\frac{hR_i}{R_\epsilon^3} - \frac{\delta_{i3}(R^2+2\epsilon^2)+R_i R_3}{R_\epsilon^3}\right) - 4\pi h\delta_{ik}\phi_\epsilon(R)\right] - \frac{6h\epsilon^2}{R_\epsilon^5}(\delta_{i3}R_j - \delta_{ij}R_3), \tag{2.24}$$

allowing direct comparison to the singular Stokeslet image system solution given in (2.11). The function $\phi_\epsilon(R)$ is given by $\psi_\epsilon^2(R)$ for $C_2 = 3$ and is $\phi_\epsilon(R) = 3\epsilon^2/(4\pi(R^2+\epsilon^2)^{5/2})$. It can be seen that the first three terms in (2.11) are modified by the inclusion of a regularisation parameter, ϵ, and that there are two new terms. The term containing the cut-off function $\phi_\epsilon(R)$ is the function that generates the source-doublet appropriate to the no-slip condition on the plane boundary. The final term is the difference between two rotlets that are derived from different cut-off functions. Here $r_\epsilon = (r^2+\epsilon^2)^{1/2}$ and $R_\epsilon = (R^2+\epsilon^2)^{1/2}$ where r and R have the same definition as in (2.11). The limit as ϵ tends to zero of all the regularised tensors, $P_j^{\epsilon}(\boldsymbol{x},\boldsymbol{y})$, $S_{ij}^{\epsilon}(\boldsymbol{x},\boldsymbol{y})$, $T_{ijk}^{\epsilon}(\boldsymbol{x},\boldsymbol{y})$, $B_{ij}^{\epsilon}(\boldsymbol{x},\boldsymbol{y})$ yield the original tensors as expected.

2.6 The boundary integral equations

The boundary element method allows a three-dimensional problem to be studied by only considering the motion of the boundary, thus reducing the dimension of the problem. The boundary element method is a method of solving linear partial differential equations that have been written as integral equations, termed *boundary integrals*. In depth details of the derivation of the boundary integral equation can be found in Pozrikidis [68].

The boundary integral equation is derived from the Lorentz reciprocal identity that states for two flows $\boldsymbol{u}$ and $\boldsymbol{u}'$ with associated stresses $\boldsymbol{\sigma}$ and $\boldsymbol{\sigma}'$ that

$$\frac{\partial}{\partial x_k}\left(u_i'\sigma_{ik} - u_i\sigma_{ik}'\right) = 0. \tag{2.25}$$

Associating the velocity field $\boldsymbol{u}'$ with a Stokes flow due to a point force of arbitrary strength $\boldsymbol{F}$, at $\boldsymbol{y}$ gives

$$u_i'(\boldsymbol{x}) = \frac{1}{8\pi\mu} S_{ij}(\boldsymbol{x},\boldsymbol{y}) F_j \quad \text{and} \quad \sigma_{ik}'(\boldsymbol{x}) = \frac{1}{8\pi} T_{ijk}(\boldsymbol{x},\boldsymbol{y}) F_j. \tag{2.26}$$

Applying (2.25) to (2.26) and integrating with respect to $\boldsymbol{x}$ over a volume V gives the surface integral

$$\int_{\partial D} \left[S_{ij}(\boldsymbol{x},\boldsymbol{y})\sigma_{ik}(\boldsymbol{x}) - \mu u_i(\boldsymbol{x}) T_{ijk}(\boldsymbol{x},\boldsymbol{y}) \right] n_k(\boldsymbol{x}) \mathrm{d}S(\boldsymbol{x}) = 0 \tag{2.27}$$

after applying the divergence theorem where $n_k(\boldsymbol{x})$ is a surface normal.

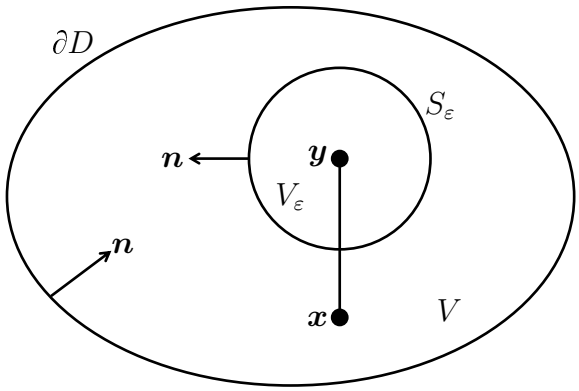

Figure 2.5: Diagram of the domains used to construct the boundary integral equation. Control volume V with boundary ∂D and inward pointing normal $\boldsymbol{n}$ and spherical volume V_ε centred at $\boldsymbol{y}$ with boundary S_ε and outward pointing normal $\boldsymbol{n}$. Redrawn from Pozrikidis [68].

Choosing a point $\boldsymbol{y}$ inside a sphere of volume $V_\varepsilon = 4\pi\varepsilon^3/3$ that is surrounded by a volume V as shown in figure 2.5 gives that the integrand of (2.27) has no singular points, therefore

$$\int_{\partial D \cap S_\varepsilon} \left[S_{ij}(\boldsymbol{x},\boldsymbol{y})\sigma_{ik}(\boldsymbol{x}) - \mu u_i(\boldsymbol{x}) T_{ijk}(\boldsymbol{x},\boldsymbol{y}) \right] n_k(\boldsymbol{x}) \mathrm{d}S(\boldsymbol{x}) = 0. \tag{2.28}$$

As ε tends to zero the tensors $S_{ij}(\boldsymbol{x},\boldsymbol{y})$ and $T_{ijk}(\boldsymbol{x},\boldsymbol{y})$ to leading order in ε are,

$$S_{ij}(\boldsymbol{x},\boldsymbol{y}) \approx \frac{\delta_{ij}}{\varepsilon} + \frac{r_i r_j}{\varepsilon^3} \quad \text{and} \quad T_{ijk}(\boldsymbol{x},\boldsymbol{y}) \approx -6\frac{r_i r_j r_k}{\varepsilon^5}, \tag{2.29}$$

where $r_i = x_i - y_i$ and the velocity, $\boldsymbol{u}(\boldsymbol{x})$ and stress, $\boldsymbol{\sigma}(\boldsymbol{x})$ tend to $\boldsymbol{u}(\boldsymbol{y})$ and $\boldsymbol{\sigma}(\boldsymbol{y})$ respectively and $(\boldsymbol{x}-\boldsymbol{y})$ and $\boldsymbol{\sigma}(\boldsymbol{x})$ decay linearly giving

$$\int_{\partial D} \left[S_{ij}(\boldsymbol{x},\boldsymbol{y})\sigma_{ik}(\boldsymbol{x}) - \mu u_i(\boldsymbol{x})T_{ijk}(\boldsymbol{x},\boldsymbol{y})\right] n_k(\boldsymbol{x})\mathrm{d}S(\boldsymbol{x}) = -8\pi\mu u_j(\boldsymbol{y}) \tag{2.30}$$

hence,

$$u_j(\boldsymbol{y}) = -\frac{1}{8\pi\mu}\int_{\partial D} \left[f_i(\boldsymbol{x})S_{ij}(\boldsymbol{x},\boldsymbol{y}) - \mu u_i(\boldsymbol{x})T_{ijk}(\boldsymbol{x},\boldsymbol{y})n_k(\boldsymbol{x})\right] \mathrm{d}S(\boldsymbol{x}) \tag{2.31}$$

where $f_i = \sigma_{ik}n_k$ is a surface traction. Equation (2.31) is termed the *boundary integral equation* and the first and second terms are called the *single-* and *double-layer potentials* respectively. These names are used because the single-layer potentials are superpositions of the hydrodynamic potentials of a point force and the double-layer potentials are caused by a layer of sources or sinks and doublets of point forces [44].

In some circumstances it is convenient to use a simplified boundary integral equation by removing the double-layer potential [68]. If $\boldsymbol{u}$ is an interior flow of a closed domain V, a complementary flow $\boldsymbol{u}'$ can be introduced exterior to the domain that vanishes at infinity and satisfies $\boldsymbol{u} = \boldsymbol{u}'$ on the boundary ∂D. By choosing a point $\boldsymbol{y}$ in the domain of $\boldsymbol{u}$ the flow $\boldsymbol{u}'$ then satisfies

$$0 = -\frac{1}{8\pi\mu}\int_{\partial D} \left[f_i'(\boldsymbol{x})S_{ij}(\boldsymbol{x},\boldsymbol{y}) - \mu u_i'(\boldsymbol{x})T_{ijk}(\boldsymbol{x},\boldsymbol{y})n_k(\boldsymbol{x})\right] \mathrm{d}S(\boldsymbol{x}). \tag{2.32}$$

Combining (2.32) with (2.31) gives

$$u_j(\boldsymbol{y}) = -\frac{1}{8\pi\mu}\int_{\partial D} q_i(\boldsymbol{x})S_{ij}(\boldsymbol{x},\boldsymbol{y})\mathrm{d}S(\boldsymbol{x}) \tag{2.33}$$

where $\boldsymbol{q} = \boldsymbol{f} - \boldsymbol{f}'$ is a modified single-layer density. The internal or external flow, $\boldsymbol{u}'$, can be found provided there is no net flux through the boundary,

$$\int_{\partial D} (\boldsymbol{u}\cdot\boldsymbol{n})\mathrm{d}S(\boldsymbol{x}) = 0. \tag{2.34}$$

However, if $\boldsymbol{u}$ consists entirely of rigid body motion then the double-layer term is automatically zero and $\boldsymbol{q} = \boldsymbol{f}$.

A method to avoid integrals of singular or near-singular quantities is to use regularised singularities instead. For this Cortez *et al.* [21] showed how a regularised boundary integral equation is convenient and can be derived from a modified Lorentz reciprocal identity with $\boldsymbol{u}'$ associated with a regularised, rather than a point, force.

Considering a solid body, D, with a point $\boldsymbol{x}$ outside D, the velocity $\boldsymbol{u}$ and pressure p satisfy Stokes' equations with zero body force. The regularised velocity, $\boldsymbol{u}^\epsilon$, and pressure, p^ϵ, are solutions of Stokes' equations with a regularised force (2.13) and have associated regularised stress given by $(2.15)_2$. Because $\partial\sigma_{ik}(\boldsymbol{x})/\partial x_k = 0$, $\partial\sigma^\epsilon_{ik}(\boldsymbol{x})/\partial x_k = -F_i(\boldsymbol{x})\psi_\epsilon(\boldsymbol{x}-\boldsymbol{y})$, $\partial u^\epsilon_i(\boldsymbol{x})/\partial x_k = 0$ and $\partial u_i(\boldsymbol{x})/\partial x_k = 0$

$$\frac{\partial}{\partial x_k}\left[u^\epsilon_i(\boldsymbol{x})\sigma_{ik}(\boldsymbol{x}) - u_i(\boldsymbol{x})\sigma^\epsilon_{ik}(\boldsymbol{x})\right] = u_j(\boldsymbol{x})F_j(\boldsymbol{x})\psi_\epsilon(\boldsymbol{x}-\boldsymbol{y}). \tag{2.35}$$

Substituting the regularised velocity solution (2.14) and regularised stress $(2.15)_2$ into (2.35) gives

$$\frac{1}{8\pi\mu}\frac{\partial}{\partial x_k}\left[S^\epsilon_{ij}(\boldsymbol{x},\boldsymbol{y})\sigma_{ik}(\boldsymbol{x}) - \mu u_i(\boldsymbol{x})T^\epsilon_{ijk}(\boldsymbol{x},\boldsymbol{y})\right] = u_j(\boldsymbol{x})\psi_\epsilon(\boldsymbol{x}-\boldsymbol{y}) \tag{2.36}$$

as F_j is constant for all j and forms the regularised equivalent of the Lorentz reciprocal identity given by Cortez *et al.* [21].

Considering a spherical volume, Ω, exterior to and containing a domain D as shown in figure 2.6

$$\frac{1}{8\pi\mu}\int\limits_{\partial\Omega}\left[S^\epsilon_{ij}(\boldsymbol{x},\boldsymbol{y})\sigma_{ik}(\boldsymbol{x}) - \mu u_i(\boldsymbol{x})T^\epsilon_{ijk}(\boldsymbol{x},\boldsymbol{y})\right]n_k\mathrm{d}S(\boldsymbol{x}) = \int\limits_{\Omega} u_j(\boldsymbol{x})\psi_\epsilon(\boldsymbol{x}-\boldsymbol{y})\mathrm{d}V(\boldsymbol{x}) \tag{2.37}$$

where $\boldsymbol{n}$ is the outward normal to the boundary $\partial\Omega$. Since $\partial\Omega$ contains ∂D and by taking the limit as the radius of the ball, Ω, tends to infinity the only contributions that remain

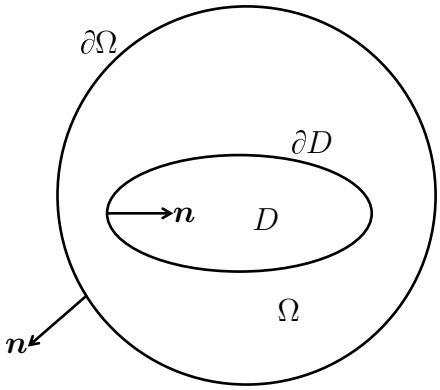

Figure 2.6: A schematic of the volume used to derive the regularised boundary integral equation for Stokes flow where Ω is a ball with boundary $\partial\Omega$ and outward pointing normal $\boldsymbol{n}$; D is a solid body with boundary ∂D and inward pointing normal $\boldsymbol{n}$. Redrawn from Cortez *et al.* [21].

are those on ∂D. Therefore, with $f_i = -\sigma_{ik}n_k$, as the normal is pointing into D,

$$-\frac{1}{8\pi\mu}\int_{\partial D}\left[S_{ij}^{\epsilon}(\boldsymbol{x},\boldsymbol{y})f_i(\boldsymbol{x}) + \mu u_i(\boldsymbol{x})T_{ijk}^{\epsilon}(\boldsymbol{x},\boldsymbol{y})n_k\right]\mathrm{d}S(\boldsymbol{x}) = \int_{\Omega} u_j(\boldsymbol{x})\psi_{\epsilon}(\boldsymbol{x}-\boldsymbol{y})\mathrm{d}V(\boldsymbol{x}) \quad (2.38)$$

and because D is a solid body the surface integral $\int_D \partial/\partial x_k \left(S_{ij}^{\epsilon}(\boldsymbol{x},\boldsymbol{y})\sigma_{ik}(\boldsymbol{x})\right)\mathrm{d}V(\boldsymbol{x})$ is zero by (2.17) as $\sigma_{ik} = -p\delta_{ik}$, giving

$$\frac{1}{8\pi}\int_{\partial D} u_i(\boldsymbol{x})T_{ijk}^{\epsilon}(\boldsymbol{x},\boldsymbol{y})n_k\mathrm{d}S(\boldsymbol{x}) = \int_{D} u_j(\boldsymbol{x})\psi_{\epsilon}(\boldsymbol{x}-\boldsymbol{y})\mathrm{d}V(\boldsymbol{x}) \quad (2.39)$$

as $-\boldsymbol{n}$ is the inward normal to D. The double-layer term is zero over the boundary as D is a solid body and by adding (2.38) and (2.39) gives

$$\int_{\mathbb{R}^3} u_j(\boldsymbol{x})\psi_{\epsilon}(\boldsymbol{x}-\boldsymbol{y})\mathrm{d}V(\boldsymbol{x}) = -\frac{1}{8\pi\mu}\int_{\partial D} S_{ij}^{\epsilon}(\boldsymbol{x},\boldsymbol{y})f_i(\boldsymbol{x})\mathrm{d}S(\boldsymbol{x}). \quad (2.40)$$

Equation (2.40) is the basis of the regularised boundary integral equation that is used to solve the Stokes flow equations for a regularised force.

There is a regularisation error associated with the evaluation of regularised singularities when compared to normal singularities. The regularisation error is brought in by the

approximation of the left hand side of (2.40), full details can be found in [21]. The cut-off function $\psi_\epsilon(\boldsymbol{x}-\boldsymbol{y})$ chosen above is positive giving

$$\int_{\mathbb{R}^3} u_j(\boldsymbol{x})\psi_\epsilon(\boldsymbol{x}-\boldsymbol{y})\mathrm{d}V(\boldsymbol{x}) = \int_{|\boldsymbol{x}|\leqslant R_c} u_j(\boldsymbol{x})\psi_\epsilon(\boldsymbol{x}-\boldsymbol{y})\mathrm{d}V(\boldsymbol{x}) + \mathcal{O}(\epsilon^2) \tag{2.41}$$

where $R_c = \sqrt{5\epsilon/2}$. The integral on the right hand side of (2.41) is given by

$$\int_{|\boldsymbol{x}|\leqslant R_c} u_j(\boldsymbol{x})\psi_\epsilon(\boldsymbol{x}-\boldsymbol{y})\mathrm{d}V(\boldsymbol{x}) = u_j(\boldsymbol{y}) + \mathcal{O}(\epsilon^2), \tag{2.42}$$

leading to the regularised boundary integral equation

$$u_j(\boldsymbol{y}) = -\frac{1}{8\pi\mu}\int_{\partial D} S^\epsilon_{ij}(\boldsymbol{x},\boldsymbol{y})f_i(\boldsymbol{x})\mathrm{d}S(\boldsymbol{x}) + \mathcal{O}(\epsilon^2) \tag{2.43}$$

that will be used to model the fluid flow inside the embryonic mouse node and the zebrafish Kupffer's vesicle.

2.7 Summary

In this chapter the singular and regularised solutions of Stokes' equations were discussed for both an infinite and semi-infinite fluid domain. The singular solutions can be used to gain an initial insight into the flow fields found in the organising structure of many species predicting a 'loopy drift' motion of particles. For both singular and regularised solutions the integral representations of flows were also discussed. Singular solutions of Stokes' equations have been used in models of the embryonic mouse node and these models will be reviewed in chapter 3 where the aspects of each model that contribute to our understanding of the flows in the embryonic node are described. Some of these models will also be expanded for the first time. To model flows in the node as accurately as possible, line distributions of singularities can be used along with the regularised boundary

integral equation. Methods and models of this nature will be discussed in chapters 4, 5 and 6.

CHAPTER 3

EXISTING MATHEMATICAL MODELS OF CILIA SHAPE, MOTION AND FLUID FLOW

3.1 Introduction

In this chapter a selection of models for cilia-driven fluid flow in the embryonic mouse node will be reviewed. The models discussed here use singularity and geometric techniques to gain insight into the flows in the node and the cilia mechanisms which generate them. Aspects of these models will then be used in further study of the embryonic mouse node and a singularity model of the zebrafish Kupffer's vesicle.

3.2 Singularity model: a rotlet

Cartwright *et al.* [15] modelled the flow inside the mouse node using the rotlet singularity of Stokes flow in an infinite domain (2.8). The rotlet singularity represents the rotational motion of fluid and is the natural choice of singularity as nodal cilia perform a conical rotation. The velocity due to a rotlet is given by

$$\boldsymbol{u} = \frac{\boldsymbol{\Omega} \wedge \boldsymbol{r}}{8\pi\mu r^3} \tag{3.1}$$

as described in chapter 2. The strength of the rotation is given by $\Omega = |\boldsymbol{\Omega}|$ where $\boldsymbol{\Omega}$ is the applied torque and $r = (r_1^2 + r_2^2 + r_3^2)^{1/2}$ is the distance from the origin. Because Stokes' equations are linear, a combination of rotlet solutions is also a solution. For example, if $\boldsymbol{u}_1$ and $\boldsymbol{u}_2$ are solutions to (2.3) then $\boldsymbol{u}_1 + \boldsymbol{u}_2$ is also a solution. The velocity due to an array of rotlets can then be represented as a sum of their velocities

$$\boldsymbol{u}_{\text{total}} = \sum_{i=1}^{N} \boldsymbol{u}_i \tag{3.2}$$

where N is the total number of rotlets used to model nodal cilia and $\boldsymbol{u}_i$ is the velocity solution given by (3.1) for the ith rotlet. A case for $N = 5$ is shown in figure 3.1.

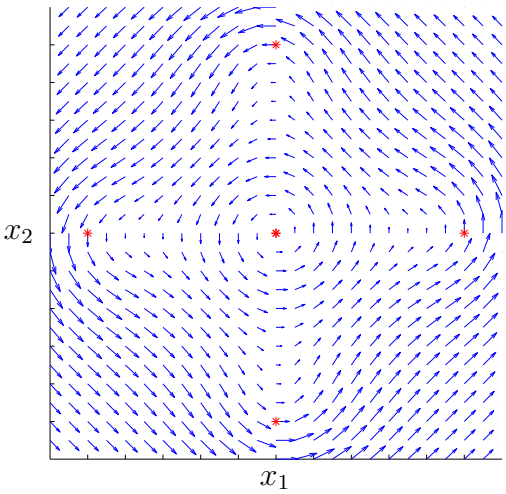

Figure 3.1: Five rotlets combine to give a larger rotlet flow field. Rotlet locations are indicated by ✳.

To model cilia in an upright configuration the rotlet has an applied torque given by $\boldsymbol{\Omega} = (0, 0, \Omega)$ and there is no directional right to left flow above or below the rotlet location, see figure 3.2.

For a directional flow towards the 'left' of the node Cartwright *et al.* proposed that a tilt relative to the node boundary was needed by the cilia and that the tilt should be towards the already-established posterior direction. The need for tilted cilia rotation should be expected from the nature of Stokes' equations because they are time reversible meaning that there must be an asymmetric rotation of the cilia for any net transport of

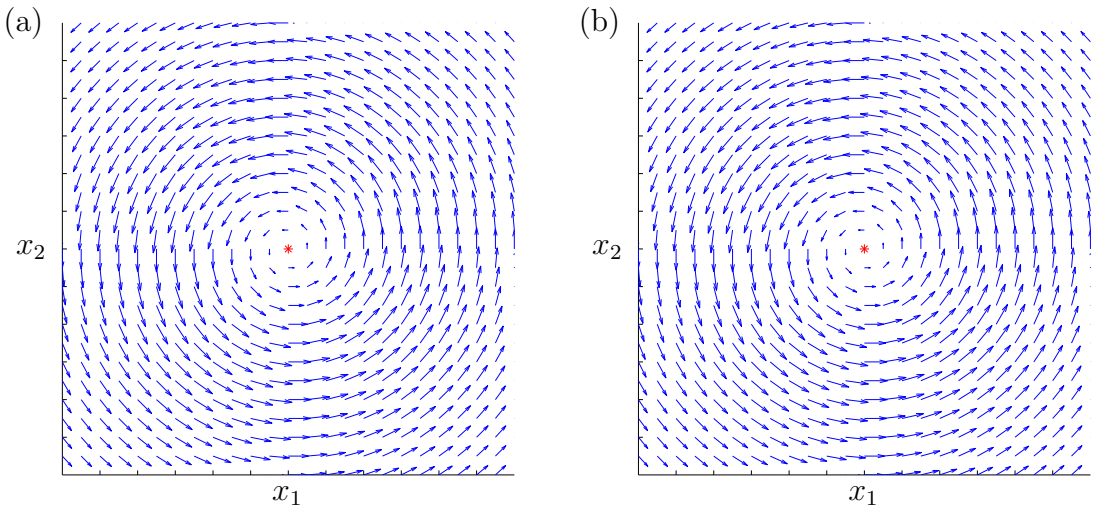

Figure 3.2: The flow field (a) above, $x_3 = 1$ and (b) below, $x_3 = -1$, an upright rotlet in an infinite fluid domain. The rotlet is located at $(0, 0, 0)$ shown by $*$.

fluid to occur. When a posterior tilt is incorporated into this model the applied torque is given by $\mathbf{\Omega} = (0, -\Omega \sin\theta, \Omega \cos\theta)$ where θ is the tilt angle. This results in a directional flow above and below the rotlet location, see figure 3.3.

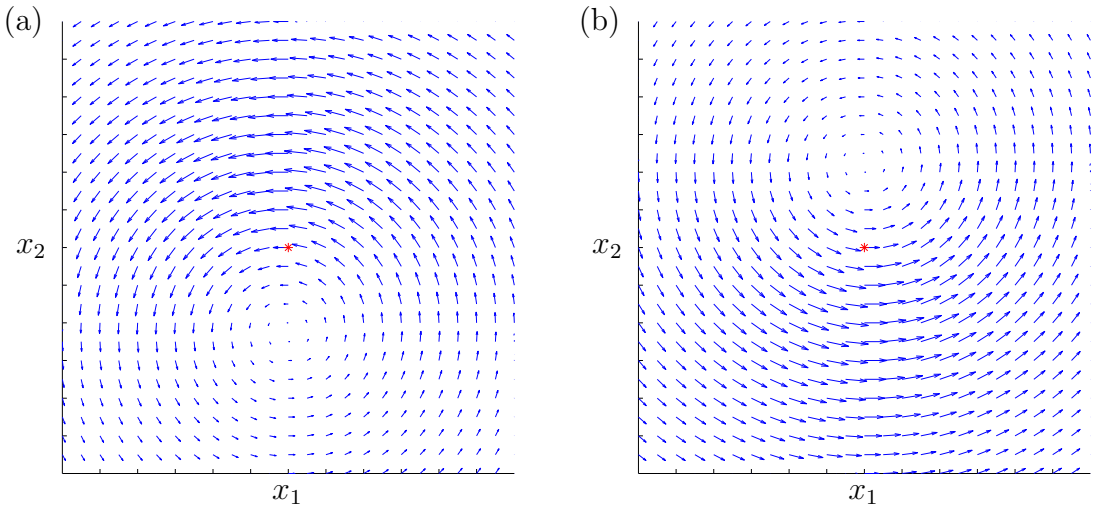

Figure 3.3: The flow field (a) above, $x_3 = 1$ and (b) below, $x_3 = -1$, a tilted rotlet with $\theta = 24°$ in an infinite fluid domain. The rotlet is located at $(0, 0, 0)$ shown by $*$.

Whilst a rotlet in an infinite fluid led Cartwright *et al.* to postulate a tilted rotation it does not take into account any boundary effects. An extension of this model is to use the rotlet image system (2.12) to incorporate a no-slip boundary at $x_3 = 0$. Maintaining $\theta = 24°$ and using the rotlet image system the flow fields are suitably modified. There is a

vortical flow close to the rotlet location (figures 3.4(a,b)) changing to a straining motion in the far-field (figure 3.4(c)) and finally to a directional flow very far from the rotlet (figure 3.4(d)) highlighting the importance of the domain boundaries.

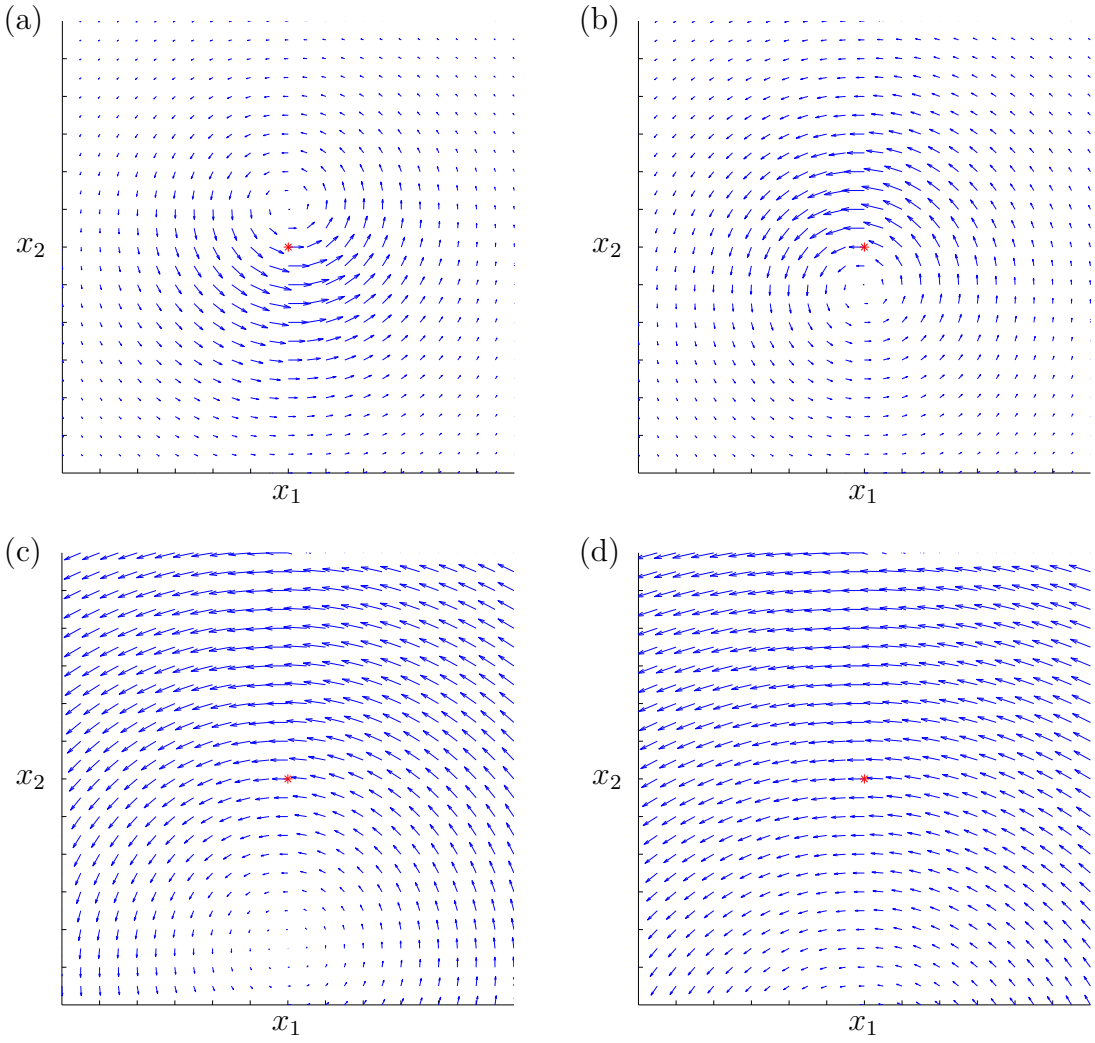

Figure 3.4: Flow fields due to a rotlet in the presence of a plane boundary at $x_3 = 0$. The rotlet is located at $(0, 0, 1)$ shown by $*$. (a) $x_3 = 0.5$, (b) $x_3 = 1.5$, vortical flow close to the rotlet location. (c) $x_3 = 3$, onset of a stresslet far-field. (d) $x_3 = 5$, stresslet far-field showing unidirectional flow. In all panels $\theta = 24°$.

3.3 Geometric model: a string of spheres

Buceta *et al.* [13] modelled cilia movements using a geometric model of a string of spheres based on polymer hydrodynamics [23] and a phenomenological two-phase angular veloc-

ity. This approach allows bending of cilia to be incorporated into the model, a possible mechanism for producing an asymmetric flow. Each cilium was modelled as a string of n spheres of radius a connected by massless rods, see figure 3.5.

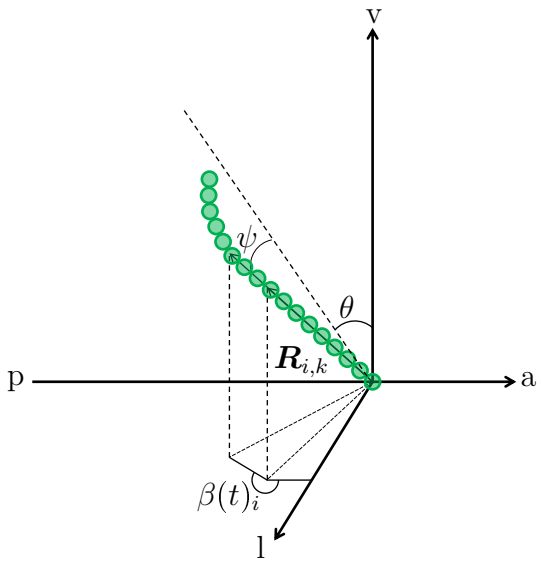

Figure 3.5: Each cilium is modelled as a string of spheres. The position of sphere i on cilium k is given by $\boldsymbol{R}_{i,k}$ and ψ, θ and $\beta(t)_i$ represent the apical, tilt and rotational angles respectively. Redrawn from Buceta *et al.* [13]. Axis notation, v, ventral; a, anterior; p, posterior and l, left.

Based on experimental observations of bending cilia at different stages of a rotation cycle, Buceta *et al.* used different angular velocities for each stage of a rotation cycle to replicate this behaviour; one angular velocity for when a cilium is approximately straight and a different angular velocity for when the cilium is bending. As part of the modelling the two-phase angular velocity introduces a phenomenological relaxation time such that when it is zero a cilium does not bend at any stage of a rotation cycle.

A cilium bends when it is close to the ciliated surface and Buceta *et al.* tested how much of the bend is due to the cilium-surface interaction. For this a cilium was treated as a massless cantilevered beam in a flow that exerts a force along the beam, F_b, parallel to the base where it is attached. The force is approximated by the low Reynolds number drag on a cylinder [37] of radius a and length L in a fluid with velocity u, dynamic viscosity, μ and kinematic viscosity, ν. This force is given by $F_\mathrm{b} = 8\pi\mu Lu/(1-2[\gamma+\ln(au/(4\nu))])$ where $\gamma \approx 0.577$ is the Euler-Mascheroni constant. Using this method, the bend is approximated

as $\Lambda_{\text{beam}} \approx 0.01\,\mu$m due to the fluid flow. An estimation of the effect of Brownian motion in a viscous fluid on particles can be acheived using Langevin's equation [70]. For a sphere of mass m, radius a the Langevin equation is given by,

$$m\frac{\mathrm{d}\boldsymbol{u}}{\mathrm{d}t} = -6\pi\mu a\boldsymbol{u} + \boldsymbol{F}(t) \tag{3.3}$$

where $6\pi\mu a\boldsymbol{u}$ is the Stokes drag on a sphere and $\boldsymbol{F}(t)$ are the random Brownian forces, $< \boldsymbol{F}(t) >= 0$. Integrating (3.3) with $\boldsymbol{x}(0) = \boldsymbol{x}_0$ and $\boldsymbol{u}(-\infty) = \boldsymbol{0}$ gives the autocorrelation function [70]

$$\boldsymbol{R}(\tau) = \frac{\boldsymbol{F}}{12\pi\mu am}\exp\left(\frac{-6\pi\mu a}{m}\tau\right). \tag{3.4}$$

This function states that the energy imparted by a thermal impulse decays exponentially on the timescale $m/6\pi\mu a$. For example, the energy given to a sphere of radius $a = 0.1\,\mu$m in water decays in approximately 10^{-9} s. The random forcing has no coherent effect on the sphere [70] and therefore no effect on the string of spheres that model the cilium. This means that any bend in cilia is from the fluid flow rather than Brownian motion. For a cilium of length $L = 5\,\mu$m the deflection is approximately $L/500\,\mu$m which is low for a fluid velocity of $10\,\mu\text{ms}^{-1}$.

Buceta *et al.* [13] showed that cilia only bend a fraction of their length. A similar phenomena has been shown in flagella that share the same internal structure to cilia, that of the axoneme. Ishijima *et al.* [39] showed that flagella much longer than nodal cilia only bend at lengths greater than $5\,\mu$m from their base. Ishijima *et al.* demonstrated that an applied flow of up to $400\,\mu\text{ms}^{-1}$ had little effect on the curvature of the flagellum below $5\,\mu$m. Therefore, flagella and indeed nodal cilia have a high rigidity below $5\,\mu$m and can be considered as straight.

3.4 Geometric model: a straight rod

An alternative method to a string of spheres is to model a cilium as a straight rod. Smith *et al.* [75] modelled the rotation of a cilium as a straight rod in combination with image singularities of Stokes flow to investigate the optimum semi-cone and tilt angles for maximum flow in a semi-infinite domain.

The position of an upright rotating rod which traces out a cone with its base at the origin, $\hat{\boldsymbol{\xi}} = \mathbf{0}$, is given by

$$\left.\begin{aligned} \xi_1(s,t) &= s\sin\psi\cos\omega t, \\ \xi_2(s,t) &= -s\sin\psi\sin\omega t, \\ \xi_3(s,t) &= s\cos\psi, \end{aligned}\right\} \tag{3.5}$$

where s is the arclength along a cilium of length l, ψ is the semi-cone angle, ω is the angular frequency and $t \geqslant 0$ is time, see figure 3.6(a).

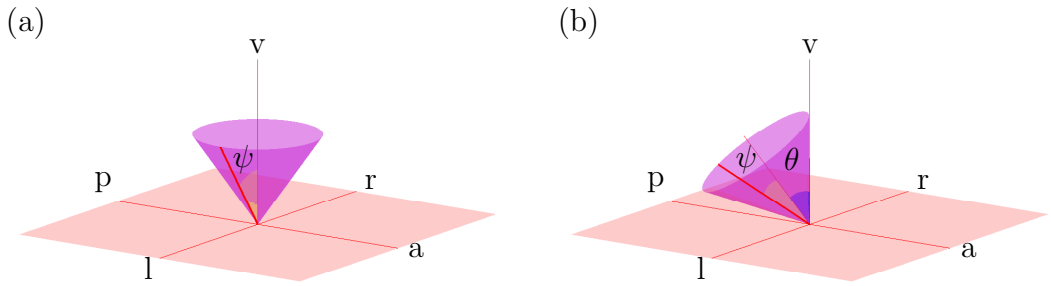

Figure 3.6: The configuration of an (a) upright straight rod with semi-cone angle ψ and (b) a tilted straight rod by an angle θ towards the posterior direction with base at $\hat{\boldsymbol{\xi}} = \mathbf{0}$. Axis notation, v, ventral; a, anterior; p, posterior; l, left and r, right.

In this model the x_1-axis is the L-R axis with positive x_1 in the 'left' direction, the x_2-axis is the A-P axis with negative x_2 in the posterior direction and the x_3-axis is the D-V axis with positive x_3 in the ventral direction. The plane $x_3 = 0$ represents the cell surface and the region $x_3 > 0$ is filled with fluid. Tilting the rod towards the posterior by an angle θ means premultipying (3.5) by a rotation matrix about the x_1-axis through an

angle of $-\theta$. For generality the base of the rod is at $\hat{\boldsymbol{\xi}} \neq \mathbf{0}$ giving,

$$\left.\begin{aligned} \xi_1(s,t) &= s\sin\psi\cos\omega t + \hat{\xi}_1, \\ \xi_2(s,t) &= -s\sin\psi\sin\omega t\cos\theta - s\cos\psi\sin\theta + \hat{\xi}_2, \\ \xi_3(s,t) &= -s\sin\psi\sin\omega t\sin\theta + s\cos\psi\cos\theta + \hat{\xi}_3, \end{aligned}\right\} \tag{3.6}$$

where $0^\circ < \theta + \psi < 90^\circ$, see figure 3.6(b). When $\theta = 0^\circ$ the upright parameterisation is restored and the cilium tip rotates with circular orbit at constant height $l\cos\psi$. When $\theta + \psi = 90^\circ$ the cilium is in direct contact with the surface of the node at the bottom of its conical sweep.

The velocity of a cilium, $\boldsymbol{u}(s,t)$, is obtained by taking the time derivative of the tilted parameterisation (3.6) and the normal, $\boldsymbol{n}(t)$, to the cilium centreline is given by

$$\left.\begin{aligned} n_1(t) &= -\sin\omega t, \\ n_2(t) &= -\cos\omega t\cos\theta, \\ n_3(t) &= -\cos\omega t\sin\theta. \end{aligned}\right\} \tag{3.7}$$

The velocity is then $\boldsymbol{u}(s,t) = \omega s\boldsymbol{n}(t)$. In resistive force theory the force per unit length, $\boldsymbol{f}(s,t)$, exerted by a cilium on a fluid at s is proportional to the centreline velocity $\boldsymbol{u}(s,t)$ [41] and thus $\boldsymbol{f}(s,t) \propto \omega s\boldsymbol{n}(t)$ meaning that only normal motion and not tangential motion needs to be considered. A point force in the x_1-direction is then $f_1(s,t) = C_N\omega s n_1(t)$, where C_N is a normal resistance coefficient.

Liron [52] calculated the volume flow rate in the x_1-direction produced by a line distribution of Stokeslets and source-doublets in a semi-infinite domain bounded by a no-slip boundary. The source-doublet produces zero flow in the half plane, $x_3 > 0$, $-\infty < x_2 < \infty$ and a Stokeslet pointing in the x_1-direction located at a height h above a plane boundary produces a volume flow rate of $h/(\pi\mu)$. Therefore, a point force with strength $f_1(s,t)$ at a distance $\xi_3(s,t)$ above a no-slip boundary has an instantaneous volume flow rate $f_1(s,t)\xi_3(s,t)/(\pi\mu)$ [75, Supp. Mat.] with point forces acting in the x_2- and x_3-directions producing zero flow due to symmetry and inverse cubic decay respectively. The

volume flow rate produced by $f_1(s,t)$ is $C_N\omega s n_1(t)\xi_3(s,t)/(\pi\mu)$ and the mean flow, Q, is calculated by integrating along a cilium of length l and averaging over a beat cycle of length $T = 2\pi/\omega$,

$$Q = \frac{1}{T}\int_0^T \int_0^l \frac{\xi_3(s,t)}{\pi\mu} f_1(s,t)\mathrm{d}s\mathrm{d}t = \frac{C_N\omega l^3}{6\pi\mu}\sin^2\psi\sin\theta. \tag{3.8}$$

To investigate maximum flow the bivariate mean volume flow rate, (3.8), is optimised. In the region $0° < \theta, \psi < 90°$ both $\sin^2\psi$ and $\sin\theta$ are non-decreasing functions and $\sin^2\psi\sin\theta$ will have a maximum at $\theta + \psi = 90°$. Substituting $\theta + \psi = 90°$ into (3.8) and imposing $\partial Q/\partial\psi = 0$ or $\partial Q/\partial\theta = 0$ for a maximum gives

$$\left.\begin{aligned} \psi &= \arctan\sqrt{2} \approx 54.7°, \\ \theta &\approx 35.3°. \end{aligned}\right\} \tag{3.9}$$

The values of ψ and θ predicted by this model agree well with the experimental values for the mouse given by Okada *et al.* [65], see figure 3.7.

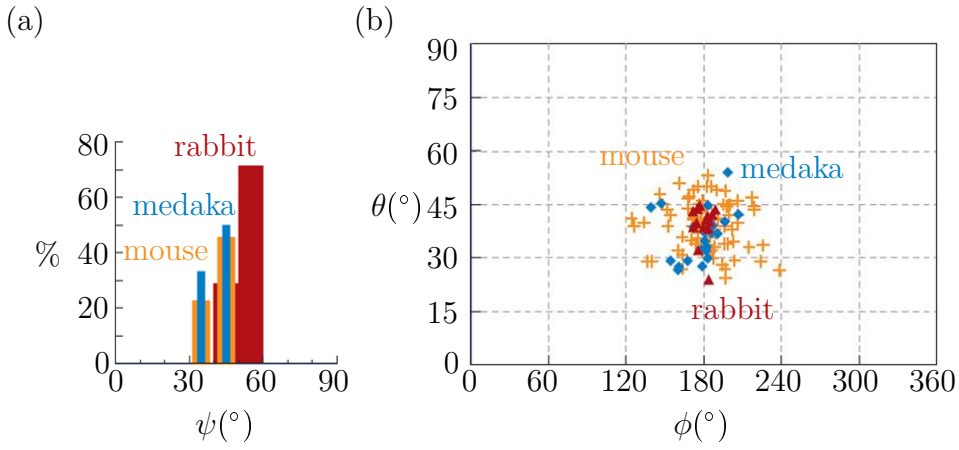

Figure 3.7: Experimental data. Distribution of parameters, (a) semi-cone angle ψ and (b) tilt angle θ where ϕ is the angle of the rotation axis from the posterior. Figure originally in Okada *et al.* [65], this version is taken from Hirokawa *et al.* [33]. Reprinted with permission from Elsevier, Okada *et al.* [65] (2005), *Cell*.

When $\theta + \psi = 90°$ the cilium comes into contact with the surface and this is not observed in experiment. Therefore the case $0° < \theta + \psi \leqslant \alpha < 90°$ should be considered.

The mean volume flow rate now has a maximum when $\theta + \psi = \alpha$, hence,

$$\left.\begin{aligned} \psi &= \arctan\left[\frac{-3+\sqrt{9+8\tan^2\alpha}}{2\tan\alpha}\right], \quad \alpha \neq 90^\circ, \\ \theta &= \alpha - \psi. \end{aligned}\right\} \tag{3.10}$$

Values of ψ and θ for all values of α can be taken from figure 3.8.

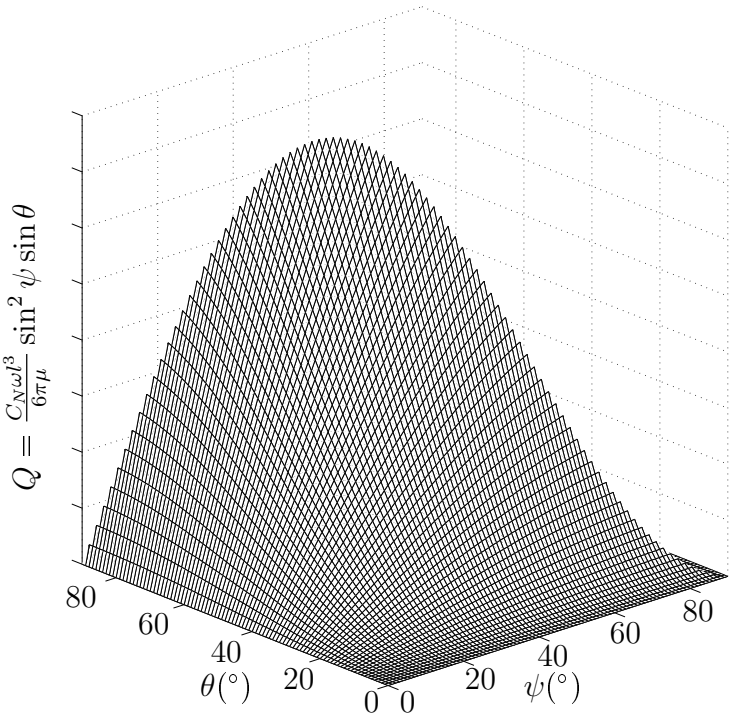

Figure 3.8: Optimal angle plot for $\theta+\psi = 90^\circ$ showing that a maximum occurs at $\psi \approx 55^\circ$ and $\theta \approx 35^\circ$. The mean volume flow rate in this plot is scaled such that $C_N\omega l^3 = 6\pi\mu$. All other values of θ, ψ for $0^\circ \leqslant \theta + \psi = \alpha < 90^\circ$ can also be read off this plot.

3.5 Summary

The rotlet singularity model led Cartwright *et al.* [15] to propose a posterior tilt in nodal cilia that was later verified in experiment [65] and is now incorporated into subsequent models. Buceta *et al.* [13] touched upon the importance of cilium-surface interactions and how the surface effect does not significantly contribute to cilia bending. In terms of asymmetric right to left flow, cilium-surface interactions are very important as they

provide the asymmetry required by Stokes' equations to give a directional flow. Using the image system formulation of a point force in the presence of a plane boundary, Smith *et al.* [75] were able to predict the optimal angle configuration for maximum flow, agreeing well with experimental values as their prediction lies in the centre of the experimentally observed values. Their work also forms part of the basis of accurate cilia modelling to calculate particle paths from the action of multiple cilia which was started in Smith *et al.* [76]. The studies of Cartwright *et al.* and Smith *et al.* show how useful singularities of Stokes flow, in particular image systems, are in predicting cilium properties and flow characteristics. The studies of Smith *et al.* use accurate slender body modelling for each cilium and this technique will be discussed in chapter 4.

CHAPTER 4

MODELLING SLENDER CILIA

4.1 Introduction

In this chapter the shape of a moving cilium is discussed with regard to using slender body theory to calculate the surrounding velocity field as a result of its motion. Slender body theory utilises the low slenderness ratio (diameter/length) of a body to calculate an approximation to the surrounding velocity field. The appropriate Green's functions for modelling cilia as slender cylinders and ellipsoids will be described and how the two approaches differ concluding with the shape that is used to model nodal cilia in the mouse node.

4.2 Slender body calculation

An average nodal cilium in the mouse node has a slenderness ratio of approximately $\eta = 0.1$, calculated using data from Hirokawa *et al.* [33]. Nodal cilia can therefore be characterised as slender bodies and as such the flow field can be modelled using slender body theory. This technique involves representing the effect of a slender body by a distribution of Stokeslets and higher order singularities along the axis, presented in chapter 2, to satisfy the no-slip boundary condition on the surface of the body as well as any present boundaries. The advantage of using slender body theory is that a problem can

be reduced from a three-dimensional partial differential equation to a one-dimensional integral equation [76]. Moving boundaries of slender bodies and surfaces can be modelled by choosing the appropriate singularity [7, 54].

Flow past a slender body of circular cross-section with an arbitrary centreline parameterisation was studied in detail by Johnson [40]. Johnson showed that the velocity can be calculated up to an $\mathcal{O}(\eta^2)$ error in the no-slip boundary condition and in the force per unit length solution along the full length of the body using a distribution of singularities. Johnson's approach is an improvement over both Gray and Hancock's resistive force theory [29] and Lighthill's method [51]. This is because the method used by Gray and Hancock underestimates the force per unit length and Lighthill's is only applicable away from the body ends. As the error is $\mathcal{O}(\eta^2)$ this approach is best applied to long, thin shapes or slender bodies. When a body is shorter or wider then this error increases rapidly. For example, if a body is twice as wide or half as long then the error increases four fold. The velocity of fluid under the influence of a moving slender body of normalised length $l = 1$ is given by the integral of appropriately weighted singularities

$$u_i(\boldsymbol{x}, t) = \int_0^1 G_{ij}(\boldsymbol{x}, \boldsymbol{\xi}(s,t)) f_j(s,t) \mathrm{d}s + \mathcal{O}(\eta^2) \tag{4.1}$$

where $G_{ij}(\boldsymbol{x}, \boldsymbol{\xi}(s,t))$ is an appropriate Green's function, $\boldsymbol{\xi}(s,t)$ is the centreline parameterisation of the slender body, $f_j(s,t)$ is the force per unit length, s is arclength and t is time. The force per unit length varies over lengths much larger than a, the radius of the cilium halfway along the slender body length ($s = 1/2$), meaning that the velocity at the surface is well approximated by the velocity of the centreline, $\partial \xi_i(s,t)/\partial t$. The problem is to find a distribution of singularities such that the velocity field on the surface, $u_i(\boldsymbol{X}(s,t)) = \int_0^1 G_{ij}(\boldsymbol{X}, \boldsymbol{\xi}(\hat{s},t)) f_j(\hat{s}) \mathrm{d}\hat{s}$, satisfies $u_i(\boldsymbol{X}(s,t)) = \partial \xi_i(s,t)/\partial t$ as accurately as possible where $\boldsymbol{X}(s,t)$ is the surface parameterisation of the slender body, see figure 4.1.

Equation (4.1) could be solved by implementing a constant force discretisation and integrating along the cilium length as a whole. However, $G_{ij}(\boldsymbol{x}, \boldsymbol{\xi}(s,t))$ varies rapidly

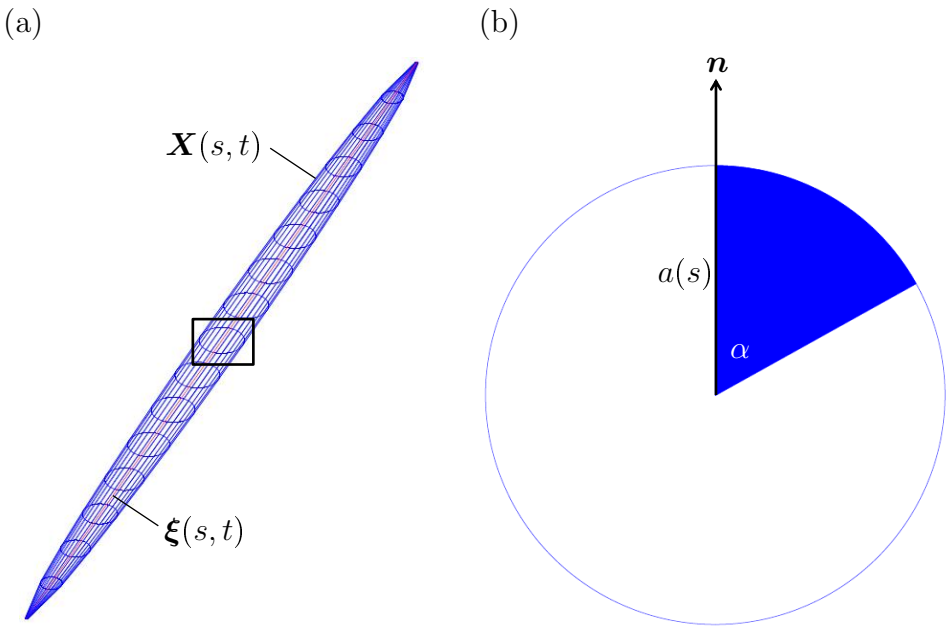

Figure 4.1: (a) Geometry of a slender body where $\boldsymbol{X}(s,t)$ is the surface parameterisation, $\boldsymbol{\xi}(s,t)$ is the centreline parameterisation at arclength s and time t. The black box is magnified in (b) showing the centre cross-section of the slender body where $\boldsymbol{n}$ is the normal, $\alpha \in (0, 2\pi]$ is the angle around the centreline and $a(s)$ is the radius of the slender body.

when $\boldsymbol{x}$ is close to $\boldsymbol{\xi}$ such that the surface velocity unacceptably oscillates between end points [76]. To circumvent this problem the cilium can be divided into N intervals $((q-1)/N, q/N)$, $q = 1, \ldots, N$ with midpoints $s_q = (q - 1/2)/N$. Assuming the force per unit length can be well approximated by a constant value at the midpoint, $f_j(s_q) \equiv f_j^q$, (4.1) becomes

$$\frac{\partial \xi_i(s,t)}{\partial t} = \sum_{q=1}^{N} f_j^q \int_{(q-1)/N}^{q/N} G_{ij}(\boldsymbol{X}, \boldsymbol{\xi}(\hat{s},t))\mathrm{d}\hat{s}. \tag{4.2}$$

Collocation at the midpoint of each cilium interval discretises the integral equation as

$$\frac{\partial \xi_i(s_p,t)}{\partial t} = \sum_{q=1}^{N} f_j^q \int_{(q-1)/N}^{q/N} G_{ij}(\boldsymbol{X}^p, \boldsymbol{\xi}(\hat{s},t))\mathrm{d}\hat{s}, \tag{4.3}$$

where $\boldsymbol{X}^p = \boldsymbol{X}(s_p,t)$ and the integrals are evaluated analytically wherever possible and with an appropriate numerical quadrature rule otherwise [1]. Evaluation technique depends on which singularities are in the Green's function $G_{ij}(\boldsymbol{x}, \boldsymbol{\xi}(s,t))$. The integral equation (4.3) can now be written as a $3N$-dimensional matrix equation $\boldsymbol{A}\boldsymbol{f} = \dot{\boldsymbol{\xi}}$ where

the matrix entries of $\boldsymbol{A}$ are given by $A_{3(p-1)+i,3(q-1)+j} = \int_{(q-1)/N}^{q/N} G_{ij}(\boldsymbol{X}^p, \boldsymbol{\xi}(\hat{s},t))\mathrm{d}\hat{s}$, the entries of $\boldsymbol{f}$ are the unknown constants f_j^q and $\dot{\boldsymbol{\xi}}$ are the velocities of each centreline interval evaluated at s_p where $i,j = 1,2,3$ and $p,q = 1,\ldots,N$. The matrix equation, $\boldsymbol{A}\boldsymbol{f} = \dot{\boldsymbol{\xi}}$, can be solved for $\boldsymbol{f}$ using direct or iterative methods provided that the condition number of $\boldsymbol{A}$ is small. After the constant force distribution, f_j^q, is known the velocity at any position in the flow domain can be found by reapplying (4.3).

4.3 Geometry of a single cilium

Modelling cilia as a straight slender body means that the centreline parameterisation is given by (3.6). In general the surface of a slender body is given by

$$\boldsymbol{X}(s,t) = \boldsymbol{\xi}(s,t) + a(s)(\boldsymbol{n}\cos\alpha + \boldsymbol{b}\sin\alpha), \tag{4.4}$$

where $\boldsymbol{n}$ and $\boldsymbol{b}$ are the normal and binormal respectively. When $a(s) = a_0$, where a_0 is a constant, the surface is represented by a cylinder which has weighted Green's function

$$G_{ij}(\boldsymbol{x},\boldsymbol{\xi}(s,t))f_j(s) = S_{ij}(\boldsymbol{x},\boldsymbol{\xi}(s,t))f_j(s) - \frac{a_0^2}{4\mu}D_{ij}(\boldsymbol{x},\boldsymbol{\xi}(s,t))f_j^{\perp}(s), \tag{4.5}$$

where $\boldsymbol{f}^{\perp}(s) = [\boldsymbol{f}(s)\cdot\boldsymbol{n}(s)]\boldsymbol{n}(s)$ is the normal component of the force per unit length, $S_{ij}(\boldsymbol{x},\boldsymbol{\xi}(s,t))$ is a Stokeslet and $D_{ij}(\boldsymbol{x},\boldsymbol{\xi}(s,t))$ is a source-doublet as described in chapter 2. The weighting on the source-dipole is chosen to satisfy the no-slip boundary condition on the surface of the slender body. Unfortunately, this method has 'end errors' that extend along the cilium length [5, 53] meaning that a cylinder representation is not good for modelling nodal cilia because an accurate solution is needed along the full length of the slender body, including the end points.

If however the surface is represented by a prolate ellipsoid [76],

$$a(s) = a_0\sqrt{1 - \frac{(s-1/2)^2}{a_0^2 + 1/4}}, \tag{4.6}$$

accurate solutions can be found along the length of the cilium, including the end points. Based on the analytic solution of Chwang & Wu [18] the weighted Green's function is given by

$$G_{ij}(\boldsymbol{x}, \boldsymbol{\xi}(s,t))f_j(s,t) = S_{ij}(\boldsymbol{x}, \boldsymbol{\xi}(s,t))f_j(s,t) - \frac{a(s)^2}{\mu}s(1-s)D_{ij}(\boldsymbol{x}, \boldsymbol{\xi}(s,t))f_j(s,t). \tag{4.7}$$

For a semi-infinite domain $S_{ij}(\boldsymbol{x}, \boldsymbol{\xi}(s,t))$ is replaced with the Stokeslet image system $B_{ij}(\boldsymbol{x}, \boldsymbol{\xi}(s,t))$ given by (2.11) to satisfy the no-slip boundary condition on the plane boundary as well as on the slender body surface.

4.4 Summary

Due to their low slenderness ratio, η, nodal cilia can be accurately modelled using slender body theory up to an $\mathcal{O}(\eta^2)$ error. Of the two cilia shapes considered here, cylinders and ellipsoids, a slender prolate ellipsoid provides accurate solutions along the length of the body. For each shape the appropriate Green's function is given in terms of a Stokeslet and quadratically weighted source-doublet. Slender body modelling of cilia forms part of the computational model of Smith *et al.* [77] which will be reviewed and expanded in chapter 5.

CHAPTER 5

COMPUTATIONAL MODEL OF FLOW IN THE EMBRYONIC MOUSE NODE

5.1 Introduction

In this chapter the computational model outlined in Smith *et al.* [77] will be discussed and further developed. This model combines slender body modelling of cilia, discussed in chapter 4, with a regularised Stokeslet representation of the covering membrane via the regularised boundary integral equation, discussed in chapter 2. This is the first singularity model of the mouse node to include the covering membrane to make the node a closed domain. This model has been published in the Journal of Engineering Mathematics [77] and a copy of this publication is included in appendix A.

By varying the cilia parameters, upright, immotile and missing cilia can be included in this model. Similarly, using experimental observations [32] of cilia at different stages of development, this model has been adapted to study each stage separately by varying the cilia parameters. The results from each of the developmental stages considered has been published in the European Physical Journal E [58] and a copy of this publication is included in appendix C.

5.2 Slender body and regularised Stokeslet model

In this model the ciliated surface is modelled as a plane boundary at $x_3 = 0$ meaning the image singularities discussed in chapter 2 can be used. Each cilium is modelled as a straight slender ellipsoid with weighted Green's function given by (4.7) with $B_{ij}(\boldsymbol{x}, \boldsymbol{\xi}(s,t))$ instead of $S_{ij}(\boldsymbol{x}, \boldsymbol{\xi}(s,t))$ because of the plane boundary. Due to the linearity of Stokes' equations the contribution to the velocity field from each cilium is given by the sum of slender body integrals

$$u_i^{\text{cilia}}(\boldsymbol{x}, t) = \sum_{m=1}^{M} \int_0^L G_{ij}(\boldsymbol{x}, \boldsymbol{\xi}^{(m)}(s,t)) f_j^{(m)}(s,t) \mathrm{d}s + \mathcal{O}(\eta^2) \tag{5.1}$$

where M is the total number of cilia, L is the length of each cilium, $\boldsymbol{\xi}^{(m)}(s,t)$ is the centreline of the m^{th} cilium given by (3.6) with a range of base positions $(\hat{\xi}_1, \hat{\xi}_2, \hat{\xi}_3 = 0)$, $G_{ij}(\boldsymbol{x}, \boldsymbol{\xi}(s,t))$ is the Green's function given by (4.7), $f_j^{(m)}(s,t)$ is the unknown force per unit length on the m^{th} cilium and η is the slenderness ratio.

To incorporate the covering membrane of the mouse node a mesh of a sphere taken from a cube is deformed initially into a hemisphere and then into an approximate triangular hemisphere using the transformation

$$\left.\begin{aligned} \hat{x}_1 &= x_1 \left(1 - \frac{x_2}{2}\right), \\ \hat{x}_2 &= x_2, \\ \hat{x}_3 &= \frac{3}{4} x_3^{1/2}, \end{aligned}\right\} \tag{5.2}$$

where (x_1, x_2, x_3) are the co-ordinates of the hemispherical surface $x_1^2 + x_2^2 + x_3^2 = A^2$, $x_3 > 0$, $A = 6$, see figure 5.1. The contribution to the velocity field from the membrane is given by a single-layer boundary integral of regularised image Stokeslets over a surface S,

$$u_i^{\text{mem}}(\boldsymbol{x}, t) = \iint_S B_{ij}^{\epsilon}(\boldsymbol{x}, \boldsymbol{y}) \phi_j(\boldsymbol{y}, t) \mathrm{d}S_{\boldsymbol{y}} + \mathcal{O}(\epsilon^2), \tag{5.3}$$

where $B_{ij}^{\epsilon}(\boldsymbol{x}, \boldsymbol{y})$ is the regularised image Stokeslet given by (2.24) so as to satisfy the no-

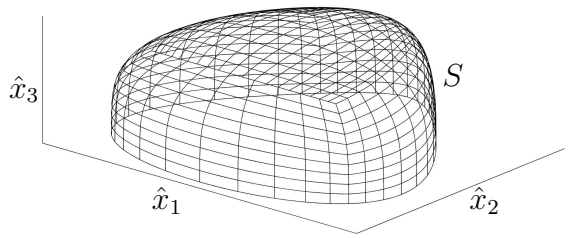

Figure 5.1: A view of the mesh used to enclose the mouse node denoted by S. The $\hat{x}_1$ axis represents the left-right axis with positive $\hat{x}_1$ being towards the left of the embryo. The $\hat{x}_2$ axis represents the anterior-posterior axis with negative $\hat{x}_2$ being towards the posterior. The $\hat{x}_3$ axis represents the dorsal-ventral axis with positive $\hat{x}_3$ being towards the ventral direction.

slip boundary condition on the plane boundary, $\phi_j(\boldsymbol{y}, t)$ is the unknown j^{th} component of the stress on the membrane at $\boldsymbol{y}$ and ϵ is the regularisation parameter. The velocity in the domain is then given by $u_i(\boldsymbol{x}, t) = u_i^{\text{mem}}(\boldsymbol{x}, t) + u_i^{\text{cilia}}(\boldsymbol{x}, t)$,

$$u_i(\boldsymbol{x}, t) = \iint_S B_{ij}^{\epsilon}(\boldsymbol{x}, \boldsymbol{y})\phi_j(\boldsymbol{y}, t)\mathrm{d}S_{\boldsymbol{y}} + \mathcal{O}(\epsilon^2) + \sum_{m=1}^{M}\int_0^L G_{ij}(\boldsymbol{x}, \boldsymbol{\xi}^{(m)}(s, t))f_j^{(m)}(s, t)\mathrm{d}s + \mathcal{O}(\eta^2). \quad (5.4)$$

The mathematical task is to find the unknowns $\phi_j(\boldsymbol{y}, t)$ and $f_j^{(m)}(s, t)$ for each timestep comprising a beat cycle. Implementing a constant stress and force per unit length on each element effectively decouples the numerical quadrature of the kernel and the discretisation of the unknowns [74, 77]. The membrane is decomposed into elements $S[1], \ldots, S[N_S]$, where $S = S[1] \cup \cdots \cup S[N_S]$, on which the stress can be approximated by $\phi_j[1], \ldots, \phi_j[N_S]$. The m^{th} cilium is decomposed into intervals $I^{(m)}[1], \ldots, I^{(m)}[N_C]$ on which the force per unit length is approximated by $f_j^{(m)}[1], \ldots, f_j^{(m)}[N_C]$. This gives the discrete system at time t as

$$u_i(\boldsymbol{x}, t) = \sum_{\nu=1}^{N_S}\phi_j[\nu]\iint_{S[\nu]} B_{ij}^{\epsilon}(\boldsymbol{x}, \boldsymbol{y})\mathrm{d}S_{\boldsymbol{y}} + \sum_{m=1}^{M}\sum_{q=1}^{N_C} f_j^{(m)}[q]\int_{I[q]} G_{ij}(\boldsymbol{x}, \boldsymbol{\xi}^{(m)}(s, t))\mathrm{d}s. \quad (5.5)$$

Using collocation at midpoints of cilium intervals and approximate centroids of surface

elements, $\boldsymbol{x} = \boldsymbol{x}^l$ for $l = 1 \ldots N$, where $N = M \times N_C + N_S$, (5.5) can be written as a $3N$-dimensional matrix equation or equivalently $3N$ scalar equations for $3N$ unknowns.

To calculate $\phi_j[\nu]$ and $f_j^{(m)}[q]$ the velocity, $u_j(\boldsymbol{x}^l, t)$, is needed for all l. For surface elements the velocity is zero and for the cilium intervals the velocity is given by the time derivative of (3.6) evaluated at $s = s_q = (q - 1/2)/N_C$. The matrix entries are calculated by choosing an $\boldsymbol{x}^l$ and integrating across all the cilium intervals and surface elements for each $\boldsymbol{x}^l$ for all l. Evaluation of the matrix entries is done analytically [74, App. B] wherever possible and numerically otherwise using standard Gauss-Legendre quadrature [1].

Smith [74, App. B] demonstrated the analytical integration of Green's functions and this will be briefly reviewed here. The integral of a regularised Stokeslet along a straight cilium interval is given by

$$\mathcal{S}_{ij}(\boldsymbol{x}, s_r) = \int_{s_r - \delta s}^{s_r + \delta s} S_{ij}^{\epsilon}(\boldsymbol{x}, \boldsymbol{\xi}(s)) \mathrm{d}s. \tag{5.6}$$

Performing a co-ordinate transformation $x_i^{\mathrm{L}} = (x_j - \xi_j(s_r))\Theta_{ij}$, where $\boldsymbol{\Theta}$ is a rotation matrix given by

$$\boldsymbol{\Theta} = \begin{pmatrix} t_1 & t_2 & t_3 \\ n_1 & n_2 & n_3 \\ b_1 & b_2 & b_3 \end{pmatrix}, \tag{5.7}$$

places a line segment onto the x_1-axis centred at the origin with tangent, normal and binormal

$$\left.\begin{aligned} \boldsymbol{t} &= \begin{pmatrix} \cos(2\pi t)\sin\psi \\ -\sin(2\pi t)\sin\psi\cos\theta - \cos\psi\sin\theta \\ -\sin(2\pi t)\sin\psi\sin\theta - \cos\psi\cos\theta \end{pmatrix}, \\ \boldsymbol{n} &= \begin{pmatrix} -\sin(2\pi t) \\ -\cos(2\pi t)\cos\theta \\ -\cos(2\pi t)\sin\theta \end{pmatrix}, \\ \boldsymbol{b} = \boldsymbol{t} \wedge \boldsymbol{n} &= \begin{pmatrix} \cos(2\pi t)\cos\psi \\ -\sin(2\pi t)\cos\psi\cos\theta + \sin\psi\sin\theta \\ -\sin(2\pi t)\cos\psi\sin\theta - \sin\psi\cos\theta \end{pmatrix}. \end{aligned}\right\} \tag{5.8}$$

The Stokeslet integral in local (L) co-ordinates is

$$\mathcal{S}_{ij}^{\mathrm{L}}(\boldsymbol{x}^{\mathrm{L}}, s_r) = \int_{-\delta s}^{\delta s} S_{ij}^{\epsilon}(\boldsymbol{x}^{\mathrm{L}}, s\boldsymbol{e}_1)\mathrm{d}s \tag{5.9}$$

and the original integral (5.6) is given by $\mathcal{S}_{ij}(\boldsymbol{x}, s_r) = \Theta_{ki}\mathcal{S}_{kl}^{\mathrm{L}}(\boldsymbol{x}^{\mathrm{L}}, s_r)\Theta_{lj}$ where the co-ordinate transformation does not affect $\mathcal{S}_{ij}$ because the integrand depends on $\boldsymbol{x}$ and $\boldsymbol{\xi}$ only through their difference.

The definite integrals in (5.9) are $\mathcal{S}_{ij}^{\mathrm{L}}(\boldsymbol{x}^{\mathrm{L}}, s_r) = \left[I_{ij}(\boldsymbol{x}^{\mathrm{L}}, s\boldsymbol{e}_1)\right]_{-\delta s}^{\delta s}$ in local co-ordinates where $I_{ij}(\boldsymbol{x}^{\mathrm{L}}, s\boldsymbol{e}_1)$ are the corresponding indefinite integrals. Written in a more compact notation with (x_1, x_2, x_3) for $(x_1^{\mathrm{L}}, x_2^{\mathrm{L}}, x_3^{\mathrm{L}})$ the indefinite integrals are

$$\left.\begin{aligned}
I_{11}^{\mathrm{L}} &= -\left(\frac{x_1 - s}{r_\epsilon}\right)\left(\frac{\epsilon^2}{x_2^2 + x_3^2 + \epsilon^2} - 1\right) + 2\log(s - x_1 + r_\epsilon), \\
I_{22}^{\mathrm{L}} &= -\left(\frac{x_1 - s}{r_\epsilon}\right)\left(\frac{\epsilon^2 + x_2^2}{x_2^2 + x_3^2 + \epsilon^2}\right) + \log(s - x_1 + r_\epsilon), \\
I_{33}^{\mathrm{L}} &= -\left(\frac{x_1 - s}{r_\epsilon}\right)\left(\frac{\epsilon^2 + x_3^2}{x_2^2 + x_3^2 + \epsilon^2}\right) + \log(s - x_1 + r_\epsilon), \\
I_{12}^{\mathrm{L}} &= I_{21}^{\mathrm{L}} = \frac{x_2}{r_\epsilon}, \quad I_{13}^{\mathrm{L}} = I_{31}^{\mathrm{L}} = \frac{x_3}{r_\epsilon}, \\
I_{23}^{\mathrm{L}} &= I_{32}^{\mathrm{L}} = -\left(\frac{x_1 - s}{r_\epsilon}\right)\left(\frac{x_2 x_3}{x_2^2 + x_3^2 + \epsilon^2}\right),
\end{aligned}\right\} \tag{5.10}$$

where $r_\epsilon^2 = (x_1 - s)^2 + x_2^2 + x_3^2 + \epsilon^2$.

To evaluate the diagonal entries of the matrix numerically would require a high-order numerical integration routine as these integrals are nearly singular. These integrals in particular benefit greatly from analytical evaluation.

Where analytical integration is not possible, numerical integration is used instead. The line integral of a general function, $f(x)$, can be evaluated numerically in an interval $a \leqslant x \leqslant b$ using Gauss-Legendre quadrature

$$\int_a^b f(x)\mathrm{d}x \approx \frac{(b-a)}{2}\sum_{i=1}^{N_q} w_i f\left(\frac{(\alpha_i + 1)(b-a)}{2} + a\right) \tag{5.11}$$

where N_q is the number of Gauss-Legendre points and w_i is the weight associated with

point α_i. The surface integral of $f(\boldsymbol{x})$ is given numerically using Gauss-Legendre quadrature in two-dimensions as

$$\int_c^d \int_a^b f(\boldsymbol{x}) \mathrm{d}x\mathrm{d}y \approx \frac{(b-a)}{2}\frac{(d-c)}{2} \sum_{i=1}^{N_q}\sum_{j=1}^{M_q} w_i w_j f(s_i,t_j) \left|\frac{\partial(x,y)}{\partial(s,t)}\right| \tag{5.12}$$

where M_q is the number of Gauss-Legendre points in the second direction, $s_i = (\alpha_i + 1)(b-a)/2 + a$, $t_j = (\alpha_j + 1)(d-c)/2 + c$ with w_i and w_j being the weights associated with points α_i and α_j and $|\partial(x,y)/\partial(s,t)|$ is the metric of the surface element being integrated over. An integral rule in two-dimensions will now be referred to as an $N_q \times M_q$ rule.

In the model of Smith *et al.* [77] the regularisation parameter for the surface elements was taken to be $\epsilon = 0.01A$, where $A = 6$ is the radius of the original hemispherical surface. This choice of regularisation parameter is based on previous numerical tests by Cortez *et al.* [21] and Smith [74]. To give a regular velocity field the Stokeslet integrals for the cilia contributions were evaluated using regularised Stokeslets with regularisation parameter $\epsilon = a(s)$.

From extensive numerical testing the surface integrals were performed using a 12×12 rule when the dimensionless distance between the evaluation point and the element centroid was less than 1.5. A 4×4 rule was used when the dimensionless distance was greater than 1.5. Cilia Stokeslet integrals were evaluated analytically as described earlier and the quadratically weighted source-doublet integrals were evaluated numerically. Numerical integrals of the source-doublets used a 12 point rule when dimensionless distances were less than 0.2 and a 4 point rule when dimensionless distances were between 0.2 and 1.0. For dimensionless distances greater than 1.0 the source-doublet contributions were neglected due to their rapid $\mathcal{O}((a/r)^3)$ decay.

Each cilium was decomposed into $N_C = 12$ elements and the covering membrane into $N_S = 6 \times 10 \times 10 = 600$ elements; for $M = 25$ cilia there are $3 \times (25 \times 12 + 600) = 2,700$ scalar degrees of freedom at each timestep. The choices of N_C and N_S come from the numerical tests shown in tables 5.1 and 5.2. There is no explicit time dependence

N_C	Final Position
1	$(-1.20, 1.92, 1.32)$
2	$(0.68, 1.95, 1.08)$
4	$(1.43, 1.93, 1.39)$
6	$(1.56, 1.89, 1.45)$
8	$(1.59, 1.87, 1.47)$
12	$(1.61, 1.86, 1.48)$
18	$(1.62, 1.86, 1.49)$
24	$(1.62, 1.86, 1.49)$

Table 5.1: Temporal convergence of a point particle started at $x_1 = 0.50$, $x_2 = 2.00$, $x_3 = 1.10$ for varying number of cilia segments, N_C, after $10,000$ timesteps. From these results, a suitable number of cilia segments is taken to be $N_C = 12$.

N_S	Final Position
$6 \times 1 \times 1$	$(-0.28, 4.85, 2.97)$
$6 \times 3 \times 3$	$(-2.88, 2.94, 2.66)$
$6 \times 5 \times 5$	$(-2.51, 2.98, 2.77)$
$6 \times 8 \times 8$	$(-2.30, 3.03, 2.89)$
$6 \times 10 \times 10$	$(-2.24, 3.04, 2.92)$

Table 5.2: Temporal convergence of a point particle started at $x_1 = 2.00$, $x_2 = 3.00$, $x_3 = 3.10$ for varying grid sizes, N_S, after $10,000$ timesteps. From these results, a suitable grid size is taken to be $N_S = 6 \times 10 \times 10$.

in Stokes' equations therefore there is no coupling between timesteps and as such each timestep can be solved independently from all others. Moreover it is only necessary to calculate the force density and stress distribution for one beat cycle due to periodicity of the problem and for this study a beat cycle is comprised of $n_{\text{beat}} = 60$ timesteps. Sixty timesteps is chosen because of the good temporal convergence of a point particle for a range of timesteps used in the numerical test, see table 5.3. The linear system is solved

n_{beat}	Final Position
60	$(-3.77, -3.64, 0.08)$
120	$(-3.76, -3.64, 0.08)$
240	$(-3.76, -3.64, 0.08)$
480	$(-3.75, -3.64, 0.08)$

Table 5.3: Temporal convergence of a point particle started at $x_1 = -4.00$, $x_2 = -4.00$, $x_3 = 0.10$ for varying number of timesteps per rotation, n_{beat}, after $10,000$ timesteps. From these results, a suitable number of timesteps to be used is $n_{\text{beat}} = 60$.

for $f_j^{(m)}[q]$ and $\phi_j[\nu]$ using LU-decomposition and once these are known the velocity at any position in the domain can be calculated by reapplying (5.5).

To analyse the effect of cilia on point particles in the fluid domain a particle tracking

algorithm based on Heun's second order method was used [76]. The algorithm works, assuming that the force density and stress distributions have already been calculated for all timesteps in a beat cycle, by first considering timestep i with position $\boldsymbol{x}_i$ at time t_i and calculating the velocity $\boldsymbol{u}(\boldsymbol{x}_i, t_i)$ using (5.5). Then, an intermediate position is given by $\boldsymbol{x}_i^* = \boldsymbol{x}_i + (\Delta t)\boldsymbol{u}(\boldsymbol{x}_i, t_i)$ where $(\Delta t) = 1/n_{\text{beat}}$ and the velocity is calculated here at time t_{i+1}, $\boldsymbol{u}(\boldsymbol{x}_i^*, t_{i+1})$. The new particle position is then given by $\boldsymbol{x}_{i+1} = \boldsymbol{x}_i + (\Delta t)[\boldsymbol{u}(\boldsymbol{x}_i, t_i) + \boldsymbol{u}(\boldsymbol{x}_i^*, t_{i+1})]/2$ thus completing timestep i.

This algorithm shows the flexibility of using singularities, which is that the flow in the entire domain does not need to be calculated at each timestep. Only the strength of the force density and stress distribution are needed to calculate the fluid velocity on the particle that is being tracked.

5.3 Particle tracking in the mouse node

The results from the regularised Stokeslet model of Smith *et al.* [77] are for an array of cilia all with the same parameters; semi-cone angle, tilt angle and angular frequency. As the node develops the cilia configurations change [32] and varying the cilia parameters allows different stages of development to be modelled. The results discussed in section 5.3.1 are published in the Journal of Engineering Mathematics and those in sections 5.3.2-5.3.4 are new results from extending this model and are published in the European Physical Journal E [58]. As with convention the 'left' of the node is on the right of each figure in this chapter.

5.3.1 Identical cilia

The model by Smith *et al.* [77] uses 25 cilia all with the same semi-cone angle, $\psi = 35°$, tilt angle, $\theta = 45°$, and angular frequency, $\omega = 2\pi\,\text{rad}\cdot\text{s}^{-1}$, meaning that the cilia rotate in synchrony. Particle transport simulations were carried out for $20,000$ timesteps or approximately 333 beat cycles as one beat cycle is made up of 60 timesteps. Particles

were started in a range of positions in the x_1x_2-plane and for a range of heights ($x_3 = 0.10, 0.30, 0.50, 1.10$) above the plane boundary representing the ciliated surface at $x_3 = 0.00$. All particles started amongst the cilia array (figure 5.2(a)) are initially swept to the 'left' of the node before being lifted above the cilia tips into a return flow due to mass conservation. Interestingly, the closer to the ciliated surface particles are released the higher they emerge above the cilia tips. In general particles were not transported beyond the edge of the cilia array, suggesting that if a particle is to reach the edge of the domain, cilia are required across the entire width of the node. Particles started above the cilia tips remained above the cilia tips.

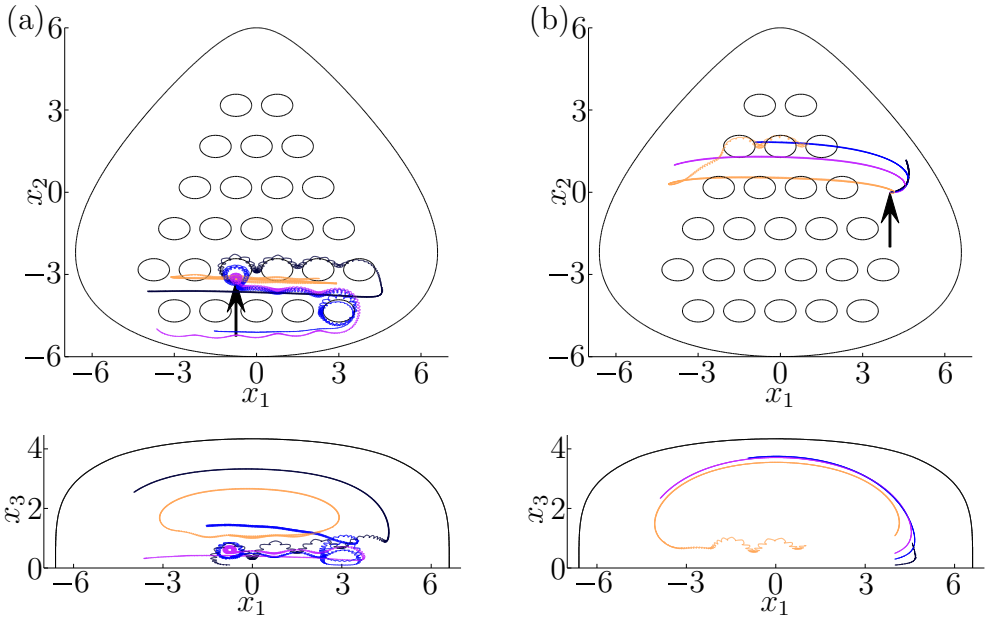

Figure 5.2: Replotted particle paths from Smith *et al.* [77], initial particle positions are indicated with an arrow. Ellipses indicate the trajectory of the cilia tips. Particles are all started at (a) $x_1 = -0.75$, $x_2 = -3.25$ and (b) $x_1 = 4.00$ and $x_2 = 0.00$. Particle paths depend on the height above the ciliated surface $x_3 = 0.10$ (—), $x_3 = 0.30$ (—), $x_3 = 0.50$ (—), $x_3 = 1.10$ (—).

Particles started in the 'left' of the node (figure 5.2(b)) are swiftly captured by the return flow close to the covering membrane unless started away from the cilia array close to the node floor. Particles started at the 'right' of the node (figure 5.3(a)) are all initially swept leftward along cilia envelopes whilst occasionally being trapped in single cilium vortices. Particles started in the posterior region (figure 5.3(b)) are initially swept

rightward due to the region of negative mean flow. Once the particles reach the 'right' edge of the cilia array they are transported leftward. Particles started at the anterior edge (figure 5.4) undergo very little transport at all heights.

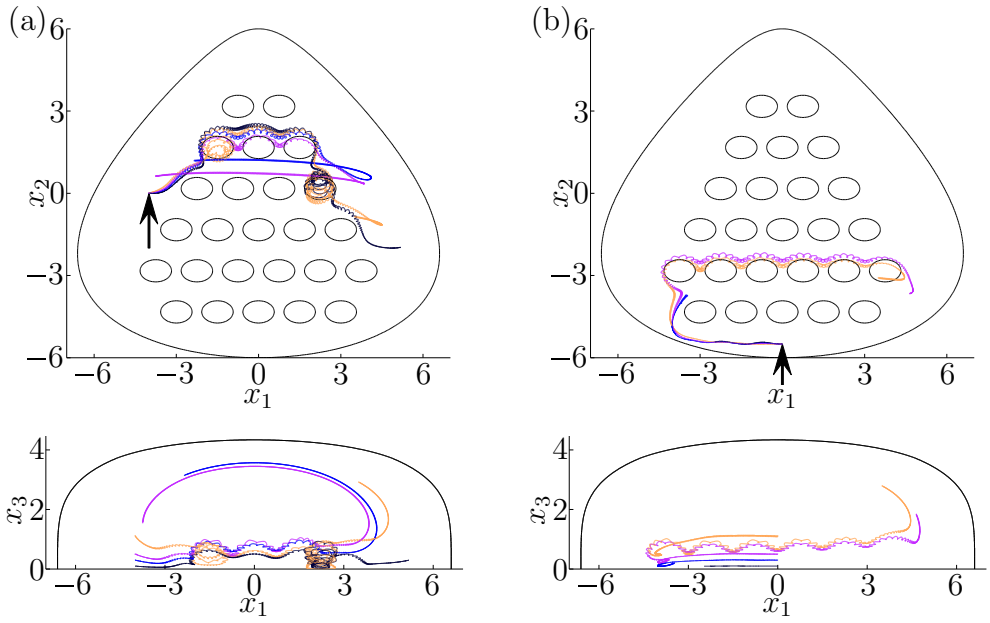

Figure 5.3: Replotted particle paths from Smith *et al.* [77] with (a) $x_1 = -4.00$ and $x_2 = 0.00$ and (b) $x_1 = 0.00$ and $x_2 = -5.50$. All other details are as in figure 5.2.

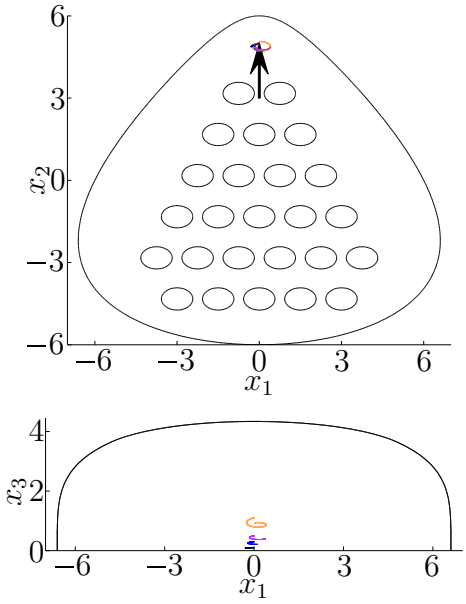

Figure 5.4: Replotted particle paths from Smith *et al.* [77] with $x_1 = 0.00$ and $x_2 = 5.00$. All other details are as in figure 5.2.

In general it is not possible to predict where particles will finish at the end of a

simulation as it is not possible to know whether a particle will become trapped in a cilium vortex or not. Similarly, particles starting initially close together will finish significantly far apart, suggesting the possible existence of chaotic advection [76, 81].

5.3.2 Upright cilia

In section 3.2 a group of rotlets all with a zero tilt angle produced a 'global vortex' (figure 3.1). Setting the tilt angle to zero, $\theta = 0°$, and keeping the semi-cone angle as $\psi = 35°$ in this model allows different flow behaviours to be predicted by analysing particle paths. The flows exhibit a range of features depending on the height above the plane boundary that they start (figure 5.5).

In the region $0.10 \leqslant x_3 < 0.40$, a leftward flow is observed, until the particle reaches the edge of the cilia array. As x_3 increases to 0.40 particles can become trapped in a single cilium vortex. In the region $0.40 \leqslant x_3 < x_3^{\mathrm{ct}}$, where x_3^{ct} is the cilium tip height given by $x_3^{\mathrm{ct}} = l\cos\psi = 1 \cdot \cos 35° \approx 0.82$, particles are transported in a 'global vortex'. A particle is initially transported leftward to the edge of the cilia array and then into a clockwise 'global vortex'. For the region $x_3 > x_3^{\mathrm{ct}}$ a 'drifting global vortex' is observed where the oscillations in the x_3-direction are greater than for $x_3 < x_3^{\mathrm{ct}}$ regions. When $x_3 \geqslant 1.10$ all 'global vortex' characteristics are lost as the particle does not reach the edge of the cilia array. The particle is captured by a weak recirculation around the top of the node.

5.3.3 Immotile and missing cilia

Immotile cilia can be introduced by setting the angular frequency to zero, $\omega = 0\,\mathrm{rad}\cdot\mathrm{s}^{-1}$ (figure 5.6(a), red ellipses) for the cilia chosen to be stationary, whilst keeping $\omega = 2\pi\,\mathrm{rad}\cdot\mathrm{s}^{-1}$ in all other cilia (figure 5.6(a), black ellipses). Particles are started in the same positions as in figure 5.2(a). Particle paths still generally show leftward advection, however with a greatly altered path. Interestingly when particles reach the 'left' they are returned close to the node floor instead of the covering membrane due to the region of

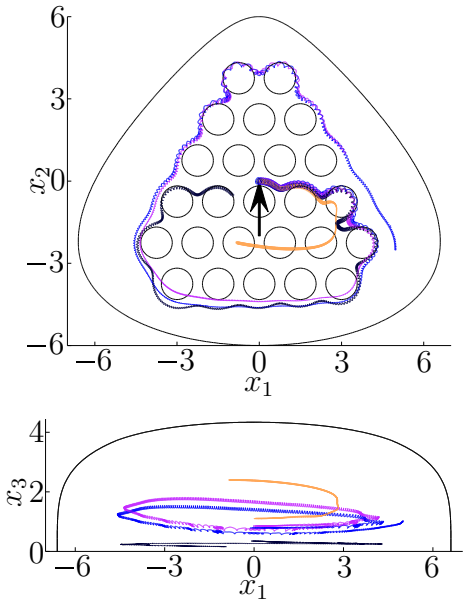

Figure 5.5: Particle paths for a configuration of upright cilia, initial positions are indicated by an arrow. Circles indicate the trajectory of the cilia tips. Particles are all started at $x_1 = 0.00$, $x_2 = 0.00$. Particle paths depend on the height above the ciliated surface $x_3 = 0.35$ (—), $x_3 = 0.78$ (—), $x_3 = 0.85$ (—), $x_3 = 1.10$ (—). Chance of trapping as x_3 increases to 0.40 (—). 'Global vortex' observed at approximate cilia tip height $x_3^{\text{ct}} \approx 0.82$ (—). 'Drifting global vortex' observed immediately above cilia tips (—). Recirculation observed for particles high above the node floor, $x_3 \geqslant 1.10$ (—).

negative mean flow at the posterior edge of the node. Particles are also trapped in single cilium vortices in more instances when neighbouring cilia are immotile. This is because the immotile cilia have far less influence on the particle paths (figure 5.6(a)).

To test the effect of immotile cilia they were removed and the particle paths were recalculated (figure 5.6(b)). The greatest difference is for the case of a particle started close to the node floor. When the cilia are immotile the particle is returned in the bottom return flow close to the posterior edge as opposed to the top return flow in the missing cilia case. However, for the majority of simulations particle paths do not differ greatly between simulations with immotile and missing cilia. For both immotile and missing cilia, particles started above the cilia tips remained above the cilia tips.

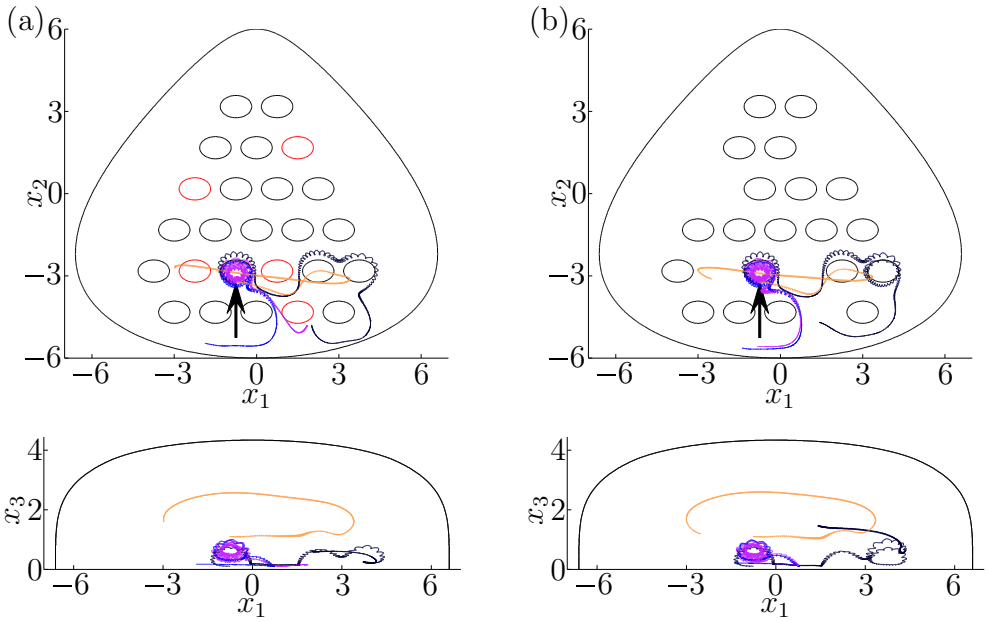

Figure 5.6: Particle paths for a configuration of cilia with some (a) immotile and (b) missing. (a) Black ellipses indicate the trajectory of motile cilia tips whereas red ellipses indicate immotile cilia positions. (b) Black ellipses indicate the trajectory of motile cilia tips. Initial positions are indicated by an arrow and are as figure 5.2.

5.3.4 Cilia configurations of developmental stages: late bud, early headfold, late headfold, 1 somite and 3 somite

Using the observations of Hashimoto *et al.* [32] it is possible to simulate the particle paths generated by an array of cilia that represents each stage of development; this is achieved by varying the cilia parameters. The cilia parameters for each stage of development can be found in table 5.4, the semi-cone angle is $\psi = 35^\circ$ and angular frequency is $\omega = 2\pi\,\mathrm{rad}\cdot\mathrm{s}^{-1}$ for all stages.

Stage	Number of Cilia	Number Tilted Anteriorly	Tilt Angle Range
late bud	17	7/17	$-10^\circ \leqslant \theta \leqslant 10^\circ$
early headfold	21	3/21	$-10^\circ \leqslant \theta \leqslant 15^\circ$
late headfold	15	1/25	$-5^\circ \leqslant \theta \leqslant 20^\circ$
1 somite	28	0/28	$20^\circ \leqslant \theta \leqslant 35^\circ$
3 somite	28	0/28	$35^\circ \leqslant \theta \leqslant 45^\circ$

Table 5.4: Cilia parameters for different stages of development. A negative tilt angle denotes a tilt towards the anterior.

Particles in the late bud and early headfold stages of development are swept around the node in a clockwise 'global vortex' when viewed from the ventral side. Particle paths

in the late headfold stage vary with starting position in the node. A particle released in the 'right' of the node is advected initially to the right and then leftward by neighbouring cilia for initial height $x_3 = 1.10$. If however a particle has initial height $x_3 = 0.50$ it is advected via a 'global vortex'. This is because cilia positioned centrally have a lesser tilt angle towards the posterior than those cilia located posteriorly. All particles released in the 1 and 3 somite stages are advected leftward by a succession of cilia. Once the particle paths reach the edge of the cilia array at the 'left' of the node they return via a rightward path close to the covering membrane. A leftward particle path is observed because all cilia are tilted towards the posterior at the 1 and 3 somite stages of development (figure 5.7).

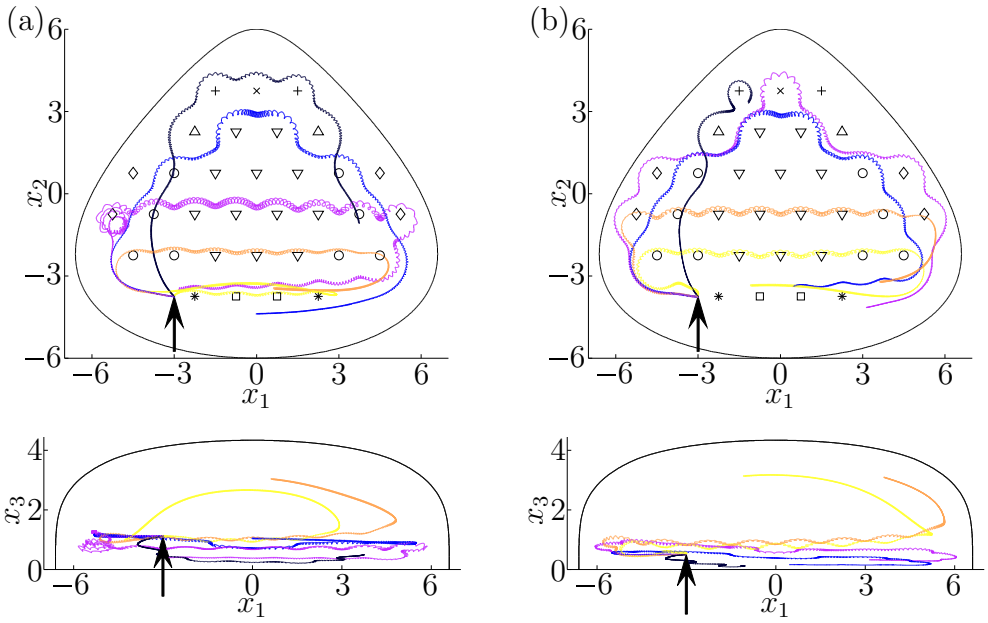

Figure 5.7: Replotted particle paths from Montenegro-Johnson *et al.* [58] for the late bud (—), early headfold (—), late headfold (—), 1 somite (—) and 3 somite (—) stages of development. Cilia positions are denoted by $\triangledown$, $+$, $\times$, $\triangle$, $\circ$, $\diamond$, $\square$, $*$, where $\triangledown$ are present at all stages, $+$, late bud only, $\times$, late bud, early headfold, late headfold only, $\triangle$, late bud, 1 somite only, $\circ$, early headfold, late headfold, 1 somite, 3 somite only, $\diamond$, late headfold, 1 somite, 3 somite only, $\square$, 1 somite, 3 somite only, $*$, 3 somite only. The initial particle position is marked with an arrow at (a) $x_1 = -3.00$, $x_2 = -3.75$, $x_3 = 1.10$ and (b) $x_1 = -3.00$, $x_2 = -3.75$, $x_3 = 0.50$.

Particles started at the 'left' of the node are returned in a rightward flow close to the covering membrane at all stages of development (figure 5.8).

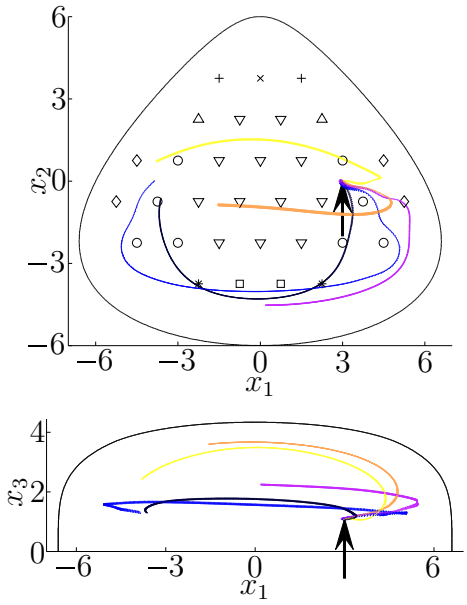

Figure 5.8: Replotted particle paths from Montenegro-Johnson *et al.* [58]. Cilia positions and track colours as figure 5.7. The initial particle position is marked with an arrow at $x_1 = 3.00$, $x_2 = 0.00$, $x_3 = 1.10$.

5.4 Summary

In this chapter a computational model of the mouse node including the covering membrane using singularities of Stokes flow was reviewed and developed. This was achieved by utilising the linearity of Stokes' equations by summing the solutions due to each cilium with the solution from the membrane and solving the resultant matrix equation. Furthermore, a predictor-corrector second order algorithm for particle tracking was described.

The results of the regularised Stokeslet model show that a posterior tilt combined with a clockwise rotation produces a dominant leftward flow due to cilium-surface interactions and the no-slip boundary condition. The inclusion of the covering membrane produces a rightward return flow due to mass conservation.

A 'global vortex' where particles circulate the domain forms when all cilia have a zero tilt angle. Immotile cilia are predicted to alter the flow by comparison to when they are missing, an important flow feature if considering the 'two-cilia' model of McGrath *et al.* [57] or Tabin & Vogan [84].

Experimental observations [32] showed that cilia positions and tilt angles change as

the node develops. Simulation results predict that the particle paths will also change. At early stages of development a 'global vortex' is predicted progressing to a 'left' directional flow as cilia tilt towards the posterior direction suggesting that the node has to develop first before a leftward flow is generated.

CHAPTER 6

COMPUTATIONAL MODEL OF FLOW IN THE ZEBRAFISH ORGANISING STRUCTURE

6.1 Introduction

In this chapter the computational model by Smith *et al.* [73] of the zebrafish organising structure, the Kupffer's vesicle, will be discussed in detail. This model takes the experimental observations of Kramer-Zucker *et al.* [46], Kreiling *et al.* [47], Lopes *et al.* [56], Okabe *et al.* [63] and Supatto *et al.* [81] for cilia length, tilt directions and angles as well as cilia positions and calculates time-averaged flow profiles for a single beat cycle of synchronised cilia. This is the first computational model of the zebrafish Kupffer's vesicle and it was developed in close collaboration with Thomas Montenegro-Johnson (né Johnson) and has been published in the Journal of Fluid Mechanics; a copy of this publication is included in appendix B. In this work Thomas developed the mesh that is used to represent the domain and the cilia and these details will be reviewed in this chapter.

This model has been further developed to incorporate additional cilia rotation mechanisms recently observed in experiment by Lopes and Rua *et al.* [personal communication] and to assess the effect of cilium length on the flow using cilia measurements for both wildtype and $DeltaD^{-/-}$ mutant embryos. Lopes and Rua provided the details of their experiments in November 2012. Their new observations showed that some cilia in the Kupffer's vesicle have more than one rotation frequency. This feature is incorporated into

this model as a 'wobble' and is discussed in section 6.4. A publication is currently being prepared with Lopes and Rua, CEDOC as well as with Smith and Montenegro-Johnson, University of Birmingham. At the time of submission of this work the manuscript was in the final stages of preparation for submission to the journal *Current Biology*.

6.2 Regularised Stokeslet model

In this model the computational domain representing the zebrafish Kupffer's vesicle (KV) and the cilia is constructed as one mesh comprised of both quadratic triangular and quadrilateral elements; to get the final mesh it is first constructed in pieces. The main part of each cilium is modelled as a cylinder with a circular cross-section of constant radius $a_0\,\mu$m as defined by (4.4) and length $\hat{\alpha}a_0\,\mu$m where $\hat{\alpha}$ depends on whether wildtype or $DeltaD^{-/-}$ mutant embryos are being studied. The end of each cilium is enclosed with a hemispherical cap of radius $a_0\,\mu$m and the base that contains the bend of each cilium connects smoothly with the rest of the domain mesh and has length $(a_0 + 0.5)\,\mu$m. The centreline of each cilium, $\boldsymbol{\xi}(s,t)$, at arclength s and time t in the cilium frame is given by

$$\boldsymbol{\xi}(s,t) = \begin{pmatrix} \cos(2\pi\hat{F}_1 t) & \sin(2\pi\hat{F}_1 t) & 0 \\ -\sin(2\pi\hat{F}_1 t) & \cos(2\pi\hat{F}_1 t) & 0 \\ 0 & 0 & 1 \end{pmatrix} \begin{pmatrix} 0 \\ \int_0^s \sin[\phi(s')]\mathrm{d}s' \\ \int_0^s \cos[\phi(s')]\mathrm{d}s' \end{pmatrix} \tag{6.1}$$

where $\phi(s)$ describes the shape of the cilium centreline about the rotational axis and $\hat{F}_1$ is the rotational frequency.

The general shape of the KV is given by a scalene ellipsoidal surface

$$\frac{x_1^2}{a_r^2} + \frac{x_2^2}{b_r^2} + \frac{x_3^2}{c_r^2} = 1 \tag{6.2}$$

where the x_1, x_2 and x_3 axes correspond to the L-R, A-P and D-V axes with positive x_1, x_2 and x_3 being towards the left, posterior and dorsal directions respectively. This choice of axis direction is made so as to match with the axis definitions in Supatto *et*

al. [81], see figure 1.8. The parameters $a_r = 35$, $b_r = 30$ and $c_r = 15$ define the radii of the ellipsoid and are taken from the experimentally observed dimensions by Kreiling *et al.* [47] for embryos at the 6 somite, 12 hours post-fertilisation, stage of development.

To produce a mesh of the ellipsoid surface that is representative of the observations for cilia positions a cell grid that defines the cilia positions as well as the cell boundaries using a Delaunay triangulation via DistMesh [67] is used. 'Every triangle in a triangulation spanning [a set of points] P satisfies the empty circumcircle criterion if and only if the triangulation is the Delaunay triangulation spanning P' [62] where the empty circumcircle criterion is when 'the circumcircle of a triangle in the triangulation is an empty circle' [62]. Once this surface triangulation is obtained, a cilium is placed at the vertex of each triangle, see figure 6.1. A triangulation of approximately uniform size will give an even

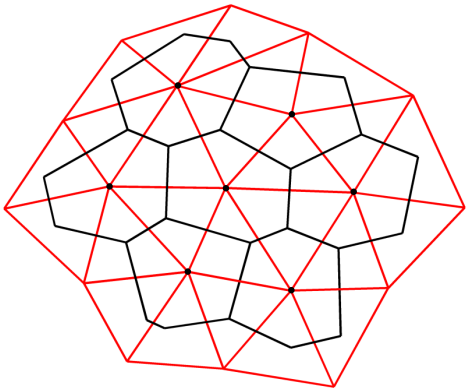

Figure 6.1: A section of the computational mesh showing the Delaunay triangulation of the surface (—), cilia positions (·) and the boundaries (—) of the Voronoi cells that are created by linking the circumcentres of the triangles that share vertices.

distribution of cilia, whereas a varying triangle size can be used to give the experimentally observed, asymmetric in the A-P and D-V axes, cilia distribution of Kreiling *et al.* [47], see figure 6.2. The cell boundaries and cilium positions are projected on to the ellipsoid surface and each cilium is then placed in position and rotated using the frame of reference for the Voronoi cell the cilium is to be part of using the Euler rotation matrix for that cell, see figure 6.2.

To test the seemingly conflicting observations of Kramer-Zucker *et al.* [46], Kreiling *et*

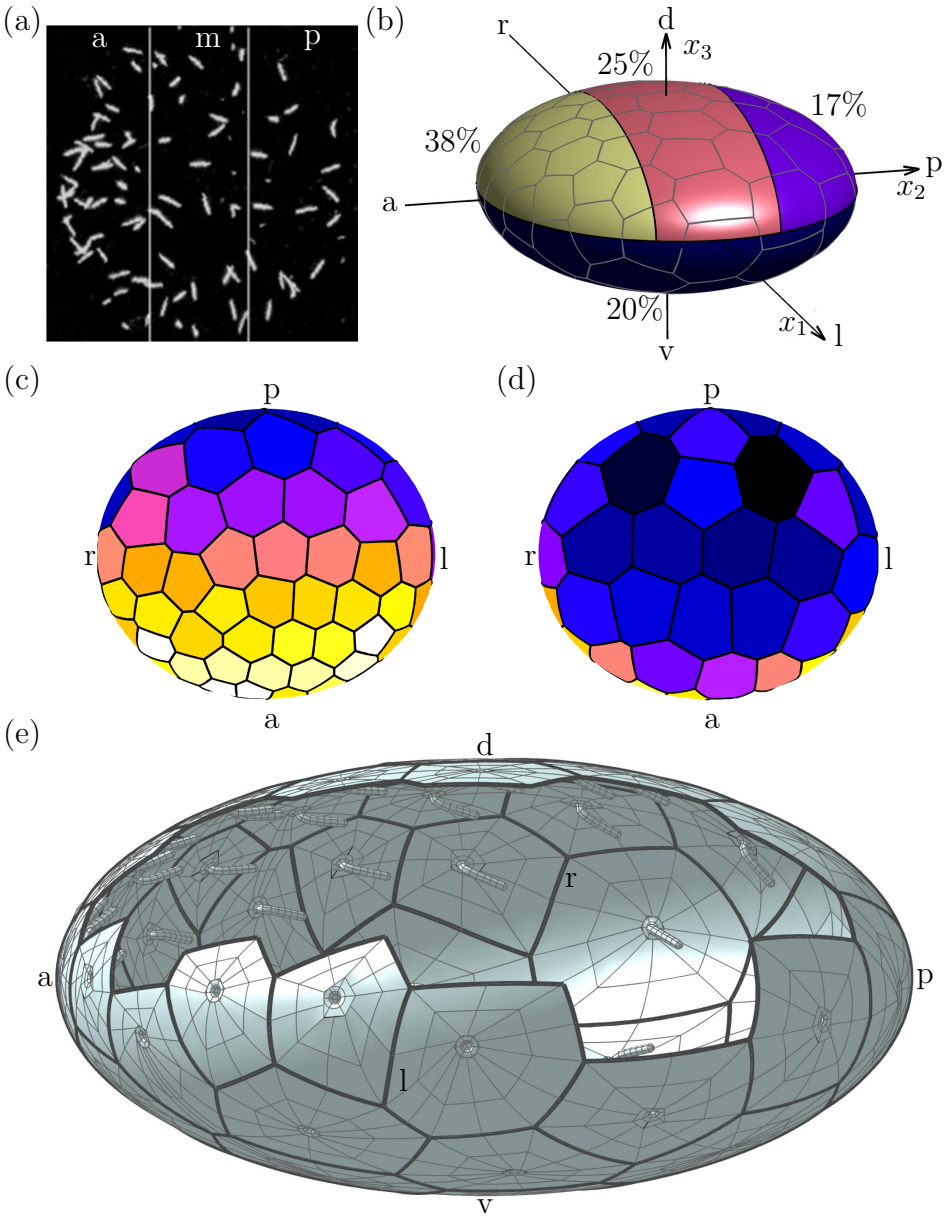

Figure 6.2: Cilia distribution in, and quadratic mesh for, the zebrafish Kupffer's vesicle. (a) Experimentally observed cilia distribution reprinted with permission from John Wiley and Sons, Kreiling *et al.* [47] (2007), *Developmental Dynamics*. (b,c,d,e) Computational mesh showing how the cilia are distributed within the Kupffer's vesicle, redrawn from Smith *et al.* [73]. Colours in (c,d) denote the area of each Voronoi cell with light colours showing the smallest cells, giving the highest cilia density, whereas dark colours show the largest cells and the lowest cilia density. (e) An example quadratic mesh of the Kupffer's vesicle. A section has been cut away for comparison with figure 1.7(d). Axis notation, d, dorsal; v, ventral; a, anterior; p, posterior; l, left; r, right and m, middle.

al. [47], Okabe *et al.* [63] and Supatto *et al.* [81] a computational mesh of an even and asymmetric cilia distribution for all cilia tilted towards the posterior or dorsal directions

and a combination of these tilt directions is produced. In each case the contribution to the velocity field is entirely from a surface mesh consisting almost completely of rigid surfaces. Thus, the velocity is given by the regularised boundary integral equation with the double-layer term neglected [21]. Because the single-layer potential from $S_{ij}^{\epsilon}(\boldsymbol{x},\boldsymbol{y})$ is continuous as $\boldsymbol{y}$ approaches the boundary, the approximation (2.43) is valid at time t

$$u_j(\boldsymbol{y},t) = \frac{1}{8\pi\mu}\int_D S_{ij}^{\epsilon}(\boldsymbol{x},\boldsymbol{y}) f_i(\boldsymbol{x},t)\mathrm{d}S(\boldsymbol{x}) + \mathcal{O}(\epsilon^2) \tag{6.3}$$

where $\boldsymbol{y}$ is a point in the fluid. The regularised Stokeslet, $S_{ij}^{\epsilon}(\boldsymbol{x},\boldsymbol{y})$, is given by (2.22) which does not have any additional terms in it for a plane boundary as there are none in this model, see figure 6.2(e), therefore the method of images is not applicable here. However, as the surface velocity is prescribed to calculate the unknown stress at the boundary and that there is no net flux through the boundary when deriving (6.3), see section 2.6, the no-slip boundary condition is satisfied as in the examples shown by Cortez *et al.* [20].

With a computational mesh generated, the mathematical problem is to solve (6.3) for the unknown stress, $f_i(\boldsymbol{y},t)$, for points $\boldsymbol{y}$ on the surface D from a prescribed velocity, $u_j(\boldsymbol{y},t)$, calculated from the centroid position change of mesh elements over a known small time interval given by $\boldsymbol{u}(\boldsymbol{y},t) = (\boldsymbol{y}(t+\delta) - \boldsymbol{y}(t-\delta))/2\delta$ for $\delta = 0.005$. The unknown stresses are calculated in a similar manner to the computational model of the embryonic mouse node outlined in chapter 5 by discretising the stress and applying collocation. Using a constant stress discretisation that takes values $f_i[1],\ldots,f_i[N]$ on surface elements $D[1],\ldots,D[N]$ where $D = D[1]\cup\cdots\cup D[N]$ and N is the total number of elements in the mesh gives the discrete form of (6.3) as

$$u_j(\boldsymbol{y}) = \sum_{n_e=1}^{N} f_i[n_e]\int_{D[n_e]} S_{ij}^{\epsilon}(\boldsymbol{x},\boldsymbol{y})\mathrm{d}S(\boldsymbol{x}) \quad \text{where} \quad \boldsymbol{y}\in D[m_e]. \tag{6.4}$$

Taking $\boldsymbol{y}$ as the centroid of $D[m_e]$ and allowing m_e to range from 1 to N and $j = 1,2,3$ gives a system of $3N$ equations for $3N$ unknown scalar stress variables, or a $3N$-

dimensional matrix equation. The integrals in (6.4) are calculated numerically as

$$\int_{D[n_e]} S_{ij}^{\epsilon}(\boldsymbol{x},\boldsymbol{y})\mathrm{d}S(\boldsymbol{x}) \approx \frac{1}{2}\sum_{k=1}^{N_q} S_{ij}^{\epsilon}[\boldsymbol{x}(\xi_k,\eta_k),\boldsymbol{y}]h_{D[n_e]}(\xi_k,\eta_k)w_k \tag{6.5}$$

where N_q is the number of quadrature points, (ξ_k,η_k) are the co-ordinates of the kth base point located inside or along the edge of the triangle or quadrilateral element in parametric space, $h_{D[n_e]}$ is the surface metric of element $D[n_e]$ and w_k is the integration weight associated with the kth base point. It should be noted that the sum of the integration weights for any value of N_q is always unity so that when integrating a constant function using this technique it will give an exact solution [69]. The mapping from physical to parameter space is given by

$$\boldsymbol{x} = \sum_{i=1}^{N_p} \boldsymbol{x}_i\phi_i(\xi,\eta) \tag{6.6}$$

where $N_p = 6$ for quadratic triangular elements and $N_p = 9$ for quadratic quadrilateral elements, $\boldsymbol{x}_i$ are the co-ordinates of the points at the corners and midpoints of edges for triangle and quadrilateral elements as well as the centre of quadrilateral elements and $\phi_i(\xi,\eta)$ are the element-node cardinal interpolation functions, see table 6.1. The surface metric is given by $h_{D[n]} = |\boldsymbol{e}_\xi \wedge \boldsymbol{e}_\eta|$ where $\boldsymbol{e}_\xi = \partial\boldsymbol{x}/\partial\xi$ and $\boldsymbol{e}_\eta = \partial\boldsymbol{x}/\partial\eta$ are the tangential vectors in physical space in the directions of ξ and η. For triangular elements the points (ξ_k,η_k) and weights w_k are taken from Taylor *et al.* [86] whereas for quadrilateral elements they can be found in Abramowitz & Stegun [1] for each number of quadrature points, N_q.

Triangular Elements		
$\phi_1 = \lambda(2\lambda-1)$	$\phi_2 = \xi(2\xi-1)$	$\phi_3 = \eta(2\eta-1)$
$\phi_4 = 4\xi\lambda$	$\phi_5 = 4\xi\eta$	$\phi_6 = 4\eta\lambda$
	$\lambda = 1-\xi-\eta$	
Quadrilateral Elements		
$\phi_1 = \xi\eta(1-\xi)(1-\eta)/4$	$\phi_2 = -\xi\eta(1+\xi)(1-\eta)/4$	$\phi_3 = \xi\eta(1+\xi)(1+\eta)/4$
$\phi_4 = -\xi\eta(1-\xi)(1+\eta)/4$	$\phi_5 = -\eta(1-\xi^2)(1-\eta)/2$	$\phi_6 = \xi(1+\xi)(1-\eta^2)/2$
$\phi_7 = \eta(1-\xi^2)(1+\eta)/2$	$\phi_8 = -\xi(1-\xi)(1-\eta^2)/2$	$\phi_9 = (1-\xi^2)(1-\eta^2)$

Table 6.1: The element-node cardinal interpolation functions for triangular ($N_p = 6$) and quadrilateral ($N_p = 9$) elements taken from Dhatt & Touzot [24].

To improve the computation time of the numerical integrals a switch between a low-order integration rule and an adaptive integration routine is used that is based upon the distance, d, between the evaluation point and the element centroid. If $d > \alpha L_e$, a low-order rule (3 point Fekete rule for triangle elements and a 3×3 Gauss quadrature rule for quadrilateral elements) is used, otherwise an adaptive routine is used, where L_e is the 'element length' and $\alpha = \sqrt{40}$ for triangular elements and $\alpha = \sqrt{21}$ for quadrilateral elements. The element length is taken to be the longest side of a triangular element and the greatest distance between opposing corner points of quadrilateral elements. The adaptive integration routine evaluates integrals for successive quadrature rules and compares the difference between results until it is within a chosen tolerance, taken here to be 10^{-7}, see table 6.2 for example evaluations of $\int S_{11}^{\epsilon}(\boldsymbol{x}, \boldsymbol{y}) \mathrm{d}S(\boldsymbol{x})$ for both quadrilateral and triangular elements. The values of α are calculated by using the adaptive integration routine on a

	Near		Far	
ϵ	Quadrilateral	Triangular	Quadrilateral	Triangular
10	0.3767673 $(3,4)$	0.3767675 $(28,55)$	0.4645104 $(3,4)$	0.4645104 $(28,55)$
1	0.3666618 $(3,4)$	0.3666619 $(28,55)$	0.4623200 $(3,4)$	0.4623200 $(28,55)$
0.1	0.3665495 $(3,4)$	0.3665497 $(28,55)$	0.4620956 $(3,4)$	0.4620956 $(28,55)$
0.01	0.3665383 $(3,4)$	0.3665384 $(28,55)$	0.4620731 $(3,4)$	0.4620731 $(28,55)$
0.001	0.3665371 $(3,4)$	0.3665373 $(28,55)$	0.4620708 $(3,4)$	0.4620708 $(28,55)$

Table 6.2: Example evalutions of $\int S_{11}^{\epsilon}(\boldsymbol{x}, \boldsymbol{y}) \mathrm{d}S(\boldsymbol{x})$ when the element centroid is near and far from the evaluation point. A random quadrilateral is used that is then decomposed into two triangular elements that when combined give the original quadrilateral element. Each column shows the result followed by the number of quadrature points used. For example, quadrilateral 3 means a 3×3 Gauss-Legendre rule and triangular 28 means a 28 point Fekete rule.

test mesh everywhere for one timestep so as to establish suitable values for this problem. Results in this chapter are for calculations performed with a regularisation of $\epsilon = 0.01$ as used in previous models of this kind [77]. Cortez [21] showed $\epsilon = 0.01$ is a suitable regularisation parameter for Stokes flow problems by calculating the drag on a sphere for different values of ϵ. The analytical solution is $\boldsymbol{F} = 6\pi\mu a\boldsymbol{u} \approx 18.85$ for $\mu = 1$, $a = 1$, $\boldsymbol{u} = \boldsymbol{e}_i$ for $i = 1$, 2 or 3. Table 6.3 shows the results for a range of mesh sizes for the sphere and the different regularisation parameters.

The full mesh for each cilia configuration in this chapter has $N = 6,252$ elements

	Grid Size			
ϵ	$6 \times 12 \times 12$	$6 \times 24 \times 24$	$6 \times 36 \times 36$	$6 \times 48 \times 48$
0.1	19.36	19.38	19.39	19.39
0.05	18.88	19.09	19.10	19.10
0.01	16.47	18.33	18.69	18.80

Table 6.3: Numerically calculated drag on a sphere for a range of mesh sizes and regularisation parameters [21]. Analytical solution, 18.85.

resulting in a large $3N$-dimensional dense matrix equation for unknown stress $f_i[n_e]$ at each timestep. A beat cycle is made up of $n_{\text{beat}} = N_I Q$ timesteps where N_I is the number of subintervals in an interval of length T and Q is the number of time quadrature points per subinterval. Because there is no time-dependence between timesteps each one can be solved separately. For this problem restarted GMRES was used to solve the linear system using the Numerical Algorithms Group (NAG, Oxford) Fortran library routines F11BDF, BEF, BFF, F11XAF and F11DBF. Once the discrete approximations, $f_i[n_e]$, are calculated, the velocity at any position in the domain can be found by reapplying (6.4). To calculate a time-averaged flow field in the zebrafish KV this process must first be completed for all n_{beat} timesteps. Once $f_i[n_e]$ is known for all n_e for each n_{beat} timesteps the time-averaged velocity, $\boldsymbol{u}^{\text{ave}}(\boldsymbol{x})$, at any position, $\boldsymbol{x}$, in the domain can be evaluated using an appropriate integration rule over the interval $t \in [t_0, t_0 + T]$

$$\boldsymbol{u}^{\text{ave}}(\boldsymbol{x}) = \frac{1}{T}\int_{t_0}^{t_0+T} \boldsymbol{u}(\boldsymbol{x}, t)\mathrm{d}t \approx \frac{1}{N_I}\sum_{n=1}^{N}\sum_{q=1}^{Q} \boldsymbol{u}\left(\boldsymbol{x}, t_{nq}\right) w_q \tag{6.7}$$

where $\boldsymbol{u}(\boldsymbol{x}, t)$ is given by (6.4). The results in the next section are all calculated using a left rectangle integration rule, $t_{nq} = (n-1)/N_I + (q-1)/N_I Q$ and $w_q = 1/Q$ for all q, with $N_I = 5$ and $Q = 12$ giving $n_{\text{beat}} = N_I Q = 60$ timepoints in the interval $[t_0, t_0 + T]$ for cilia with a rotational frequency $\hat{F}_1 = 30\,\text{Hz}$. The time interval is defined with $t_0 = 0.06$ and $T = 1$ because for a time interval of length one each cilium will complete a full rotation in non-dimensional time, $\hat{t} = \hat{F}_1 t$.

6.3 Time-averaged flow in the zebrafish Kupffer's vesicle

Each cilium used in this section is modelled with a centreline given by (6.1) with $\hat{F}_1 = 30\,\text{Hz}$ and $\phi(s) = a\tanh(bs)$ where the angle made by each cilium to the vertical is given by $a = 35°$ and the parameter $b = 5$ places the bend in the cilium base, see figure 6.3(a). Each cilium is modelled with $a_0 = 0.3\,\mu\text{m}$ and $\hat{\alpha} = 10$ making the length of each cilium $4.1\,\mu\text{m}$ from the tip of the hemispherical cap to the base that connectes smoothly with the domain mesh, see figure 6.3(b).

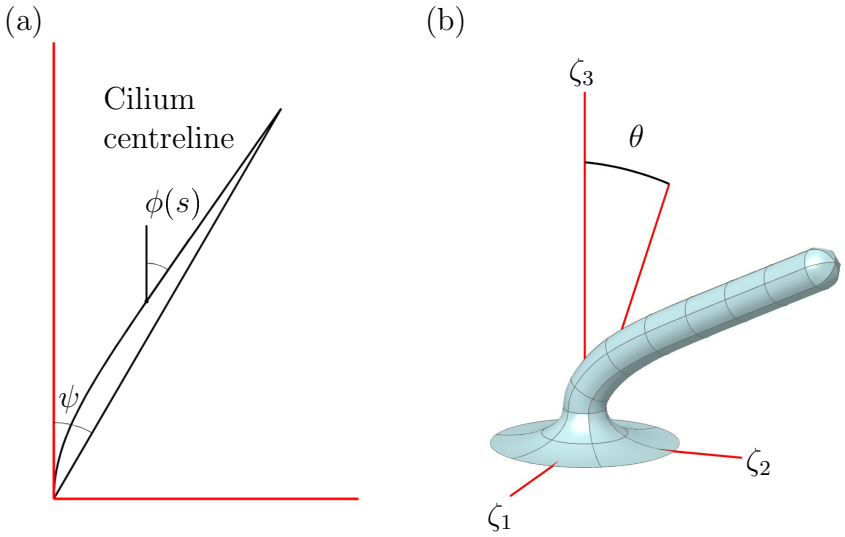

Figure 6.3: Geometry of a cilium in the computational mesh redrawn from Smith *et al.* [73]. (a) The cilium centreline is defined by $\phi(s) = a\tanh(bs)$ for $a = 35°$, $b = 5$ and semi-cone angle ψ. (b) Mesh of a cilium in the cilium co-ordinate frame $(\zeta_1, \zeta_2, \zeta_3)$. The tilt angle is denoted by θ and each cilium is tilted towards the ζ_2-axis and rotates clockwise when viewed from tip to base.

To enable direct comparison with the experimental observations of Supatto *et al.* [81], an anticlockwise swirl of fluid about the D-V axis with the centre of the swirl shifted towards the anterior edge, see figure 1.8, the flow fields are calculated in the AP-LR plane, x_1x_2-plane in this model, at $x_3 = 0$. The results are shown from the dorsal side looking in the ventral direction at an exact mid-plane between the dorsal roof and the ventral floor. Additionally, flow fields will be presented in the LR-DV plane, x_1x_3-plane, at $x_2 = 0$ to give further information about the overall flow field. To date there are no

experimental observations of flow in the LR-DV plane for these simulation results to be compared with; this is most likely because of the position of the yolk during development obscuring this view, see figure 1.7(a).

The results of this model are presented as time-averaged flow fields as opposed to particle tracking paths because the domain in this model is much larger than in previous organising structure models meaning that point particle tracking simulations do not offer the same level of information as they did before. To be able to offer useful information, the experimental observations [46, 47, 63, 81] are taken into consideration separately and as combinations of one another. The cases modelled here are as follows:

(a) all cilia tilted towards the posterior pole [46, 63],

(b) all cilia tilted towards the dorsal pole [81],

(c) a mix of cilia tilted towards the posterior and dorsal poles based on separate observations [47, 81].

For each of these cases the effect of an even and asymmetric cilia distribution [47] is examined giving six cases in total.

6.3.1 All cilia have a posterior tilt

For an even distribution of cilia, all with a posterior tilt, there is no evidence of an overall anticlockwise swirl about the D-V axis from the simulations (figure 6.4(a)). This is primarily because the cilia on the roof and the floor are producing opposite motions to one another which results in an almost complete cancellation at the mid-plane being examined. Also, because at the plane in question, $x_3 = 0$, the tilt angles will be small meaning little flow will be produced, as shown by Nonaka *et al.* [61] in a mechanical model of cilia in the mouse node.

In contrast, an asymmetric cilia distribution will produce a weak anticlockwise swirl about the D-V axis because there are now more cilia on the roof than on the floor which

now dominate the flow (figure 6.4(d)). However, the magnitude of the flow in this cilia configuration is significantly less than the reported value of 10 μms^{-1} by Supatto & Vermot [82]. An interesting feature of this simulation result for an asymmetric cilia distribution is that the centre of the swirl is shifted towards the anterior edge of the KV, which is one of the experimentally observed flow features, see figure 1.8(d).

6.3.2 All cilia have a dorsal tilt

When all cilia have a dorsal tilt and are distributed evenly throughout the KV the predicted flow is an anticlockwise swirl about the D-V axis that has an approximately equal magnitude at equivalent points from the centre (figure 6.5(a)). This is because a cilium located at the mid-plane of the D-V axis that is tilted in the dorsal direction will rotate like a cilium in the mouse node where the effective stroke moves a greater amount of fluid in one direction over the recovery stroke in the opposite direction. Placing multiple cilia with this action in a ring with an even distribution will produce an approximately uniform swirl. In general the direction of the swirl is determined by the rotation direction of the cilia and the tilt direction. The combination of a clockwise cilia rotation, when viewed from tip to base, with a dorsal tilt produces an anticlockwise swirl.

A similar result is found for the asymmetric cilia distribution for the same reason (figure 6.5(d)). The difference here though is that the flow is faster from anterior to left than it is from posterior to right in an anticlockwise motion. This is because there is now a greater number of cilia in the anterior region of the KV than the posterior region and that the cilia are tilted towards the dorsal direction. Again, the centre of the swirl has moved towards the anterior edge.

6.3.3 A combination of tilt directions

Applying a combination of tilt directions does not markedly alter the results for an even distribution of cilia compared to the dorsal tilt only case (figure 6.6(a)). This is because

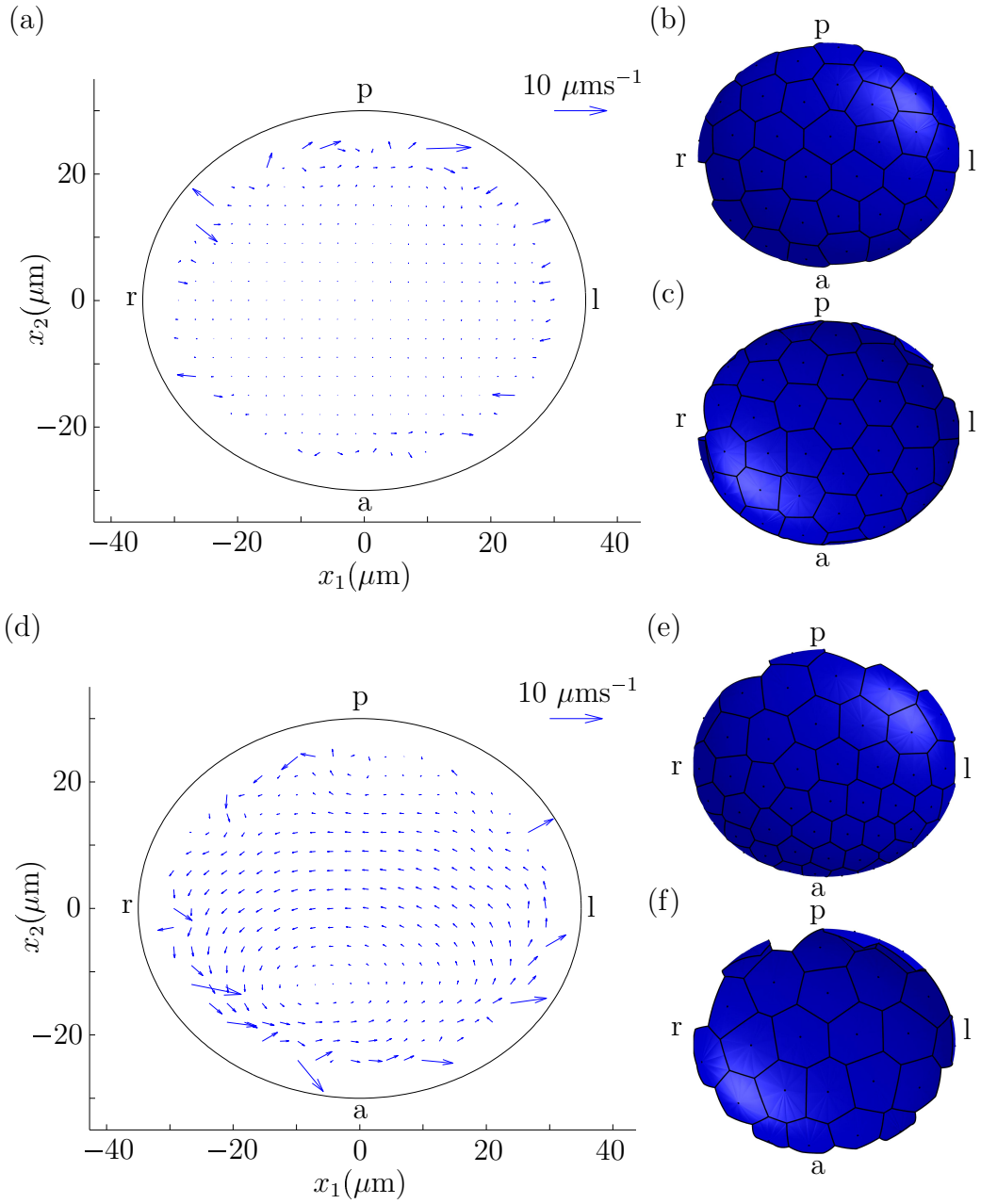

Figure 6.4: Time-averaged flow field $(u_1(\boldsymbol{x}), u_2(\boldsymbol{x}))$ in the AP-LR plane at $x_3 = 0$, computed over a beat cycle comprised of $n_{\text{beat}} = 60$ timesteps looking in the ventral direction for (a,b,c) an even cilia distribution and (d,e,f) the experimentally observed cilia distribution. (a,d) Time-averaged flow fields. (b,c,e,f) Cilia densities on (b,e) the dorsal roof and (c,f) the ventral floor where the dark shading denotes cilia that are tilted towards the posterior pole. The scale arrow of $10\,\mu\text{ms}^{-1}$ corresponds to a prescribed cilia beat frequency of $\omega = 2\pi \cdot 30\,\text{Hz}$ and cilium length $L = 4.1\,\mu$m; because Stokes flow is linear the results for different cilia beat frequencies or cilia lengths can be calculated from the relation $u \propto \omega L$. Replotted from Smith *et al.* [73]. Axis notation a, anterior; p, posterior; l, left and r, right.

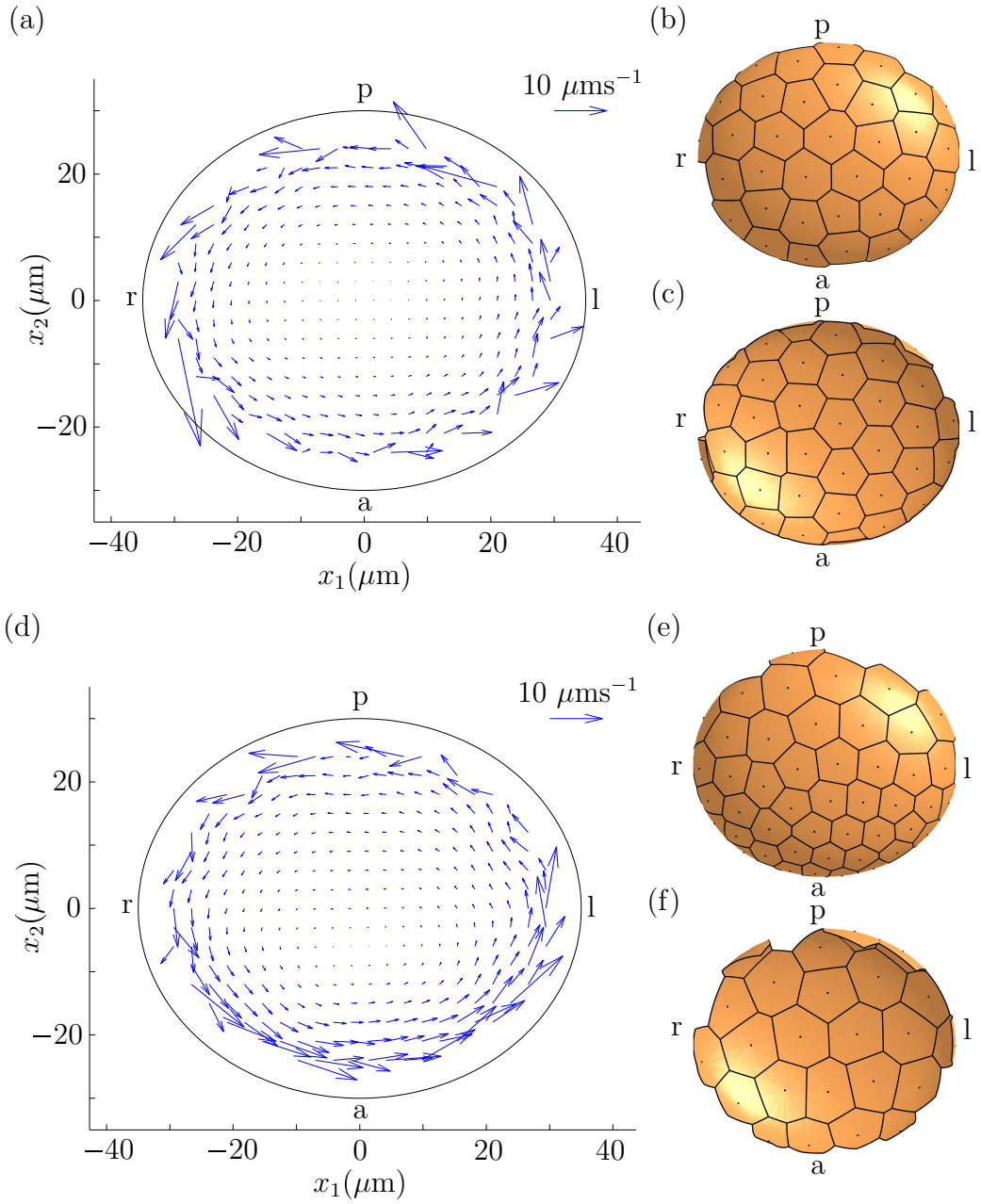

Figure 6.5: As figure 6.4 but for all cilia tilted towards the dorsal pole. (b,c,e,f) Light shading denotes cilia that are tilted towards the dorsal pole. Replotted from Smith *et al.* [73].

in the mid-plane, $x_3 = 0$, in the combined tilt case cilia are still tilted in the dorsal direction, the same as in the dorsal tilt only case. This is also the same for the asymmetric cilia distribution case, where the centre of the swirl is still shifted towards the anterior edge (figure 6.6(d)). However, by considering the transverse DV-LR plane, $x_2 = 0$, the flow fields for dorsal tilt only and combined tilt for an asymmetric cilia distribution are

remarkably different (figure 6.7). The flow in the DV-LR plane is very weak for dorsal tilt only cilia with no particular direction whereas in the combined cilia tilt case there is a leftward flow close to the dorsal roof that has a rightward counterflow near to the ventral floor that is of similar magnitude. In all six cases considered in this section there are

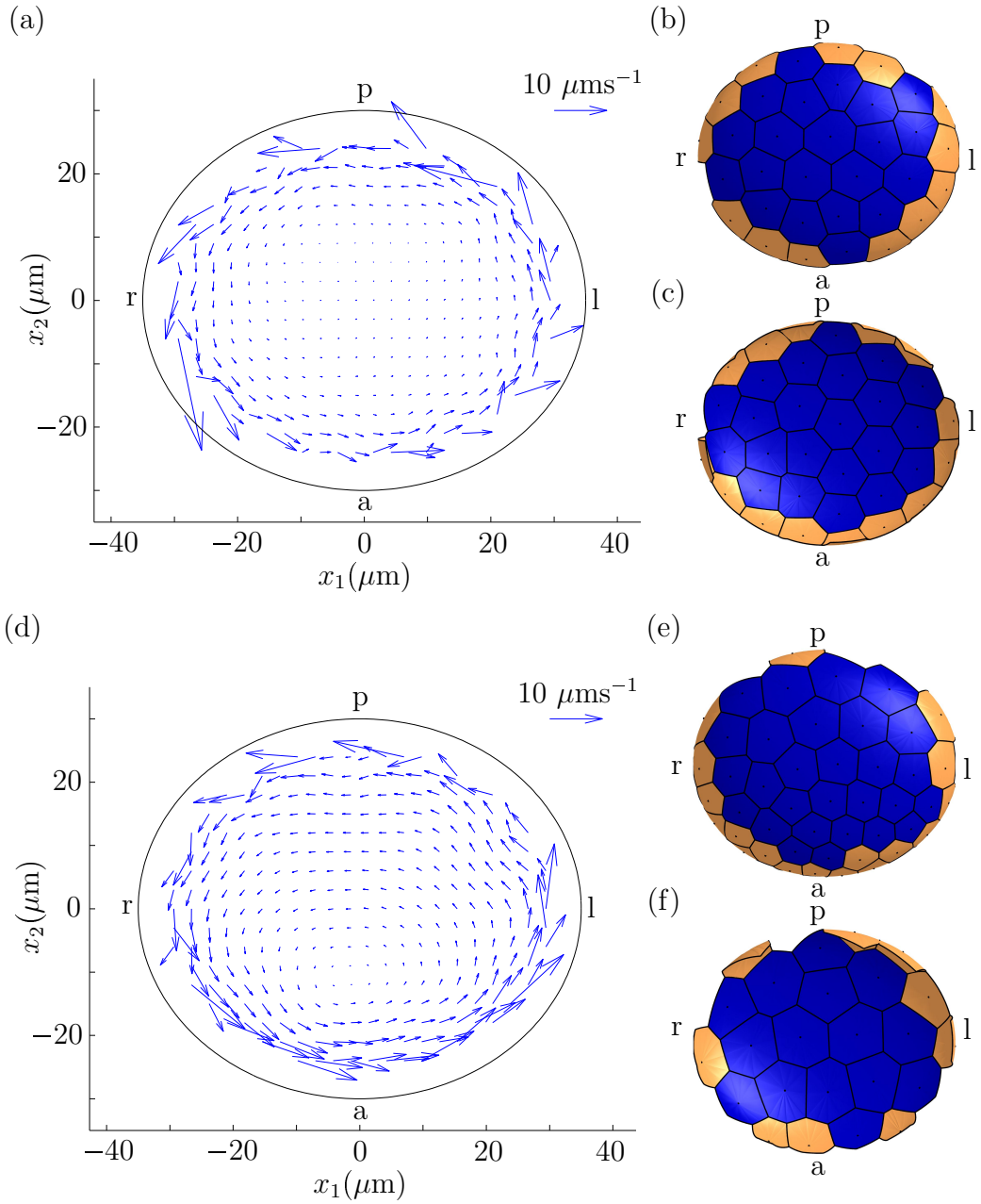

Figure 6.6: As figure 6.4 but for a combination of cilia tilted towards the posterior and dorsal poles. (b,c,e,f) Dark shading denotes cilia that are tilted towards the posterior pole whereas light shading denotes a tilt towards the dorsal pole. Replotted from Smith *et al.* [73].

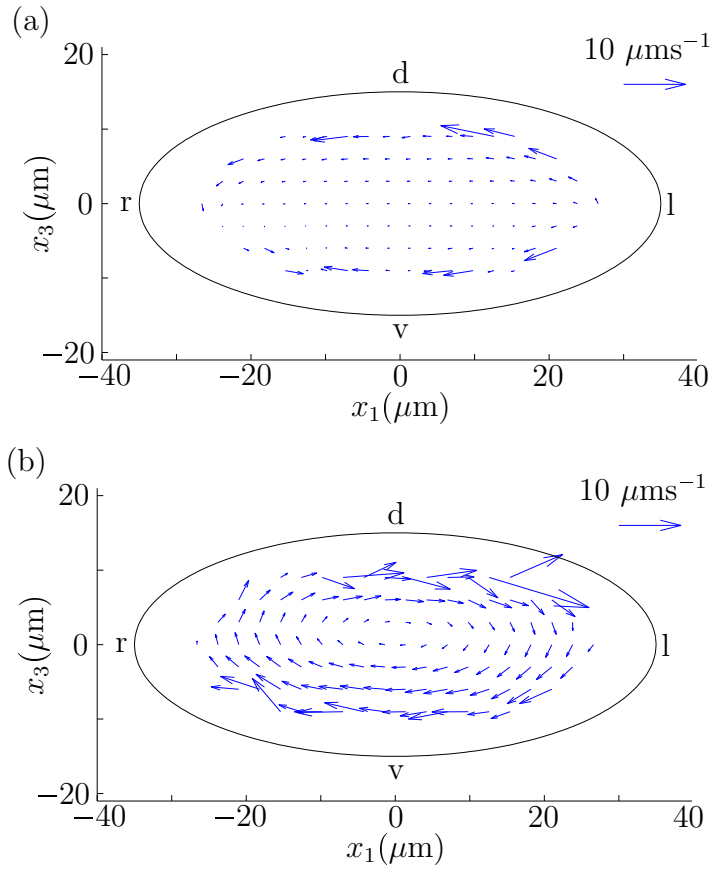

Figure 6.7: Time-averaged flow field $(u_1(\boldsymbol{x}), u_3(\boldsymbol{x}))$ in the DV-LR plane at $x_2 = 0$ only, computed over a beat cycle comprised of $n_{\text{beat}} = 60$ timesteps looking in the posterior direction for (a) all cilia tilted towards the dorsal pole and for (b) a combination of cilia tilted towards the posterior and dorsal poles. All other details are as in figure 6.4. Replotted from Smith *et al.* [73].

some instances of very large velocities towards the periphery of the KV, see figures 6.4d, 6.5(a) and 6.6(a). This kind of flow field feature should not be unexpected in this region because it is in close proximity to cilia tips at points of their rotation cycle. A cilium tip rotating at 30 Hz will have a tip speed of approximately 70 μms^{-1} meaning that in peripheral regions large velocity components can be expected.

6.4 Multiple frequencies in zebrafish cilia

For nodal cilia in many species only an average cilium beat frequency is reported [19, 35, 46, 63, 65, 71]. Based on Fourier analysis of cilia in the zebrafish KV Lopes and Rua *et*

al. [personal communication] have found that a portion of the cilia exhibit more than one frequency; a two-cilia population hypothesis characterised by the cilia frequencies with one group rotating with a single frequency and a second group rotating with two frequencies.

To model a cilium with two frequencies a 'wobble' can be introduced into the cilium centreline. A cilium rotating with frequency $\hat{F}_1$ can be made to wobble with a frequency $\hat{F}_2$ by altering how the cilium centreline behaves in time; this is achieved with $\phi(s) = (a + \varepsilon \sin(2\pi \hat{F}_2 t)) \tanh(bs)$ in (6.1) where $\varepsilon \geqslant 0$ controls the contribution of the wobble, see figure 6.8. If the observed frequencies are measured as $\hat{f}_1$ and $\hat{f}_2$ from the Fourier spectra, then the simulation frequencies need to be defined as $\hat{F}_1 = \hat{f}_1$ and $\hat{F}_2 = \hat{f}_1 - \hat{f}_2$ in this model so as to give the same peaks in the simulation Fourier spectra. In these

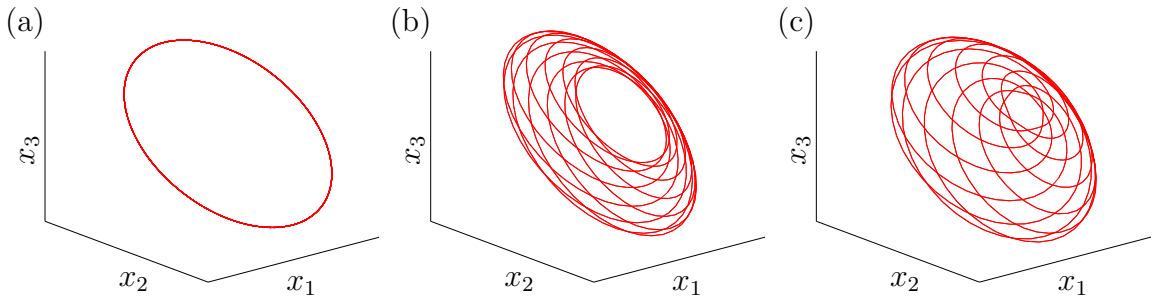

Figure 6.8: Cilium tip tracks. (a) $\varepsilon = 0$, (b) $\varepsilon = 0.25$, (c) $\varepsilon = 0.45$ for frequencies $\hat{F}_1 = 36\,\text{Hz}$ and $\hat{F}_2 = 21\,\text{Hz}$.

simulations the domain is represented as before, as a scalene ellipsoid (6.2) with cilia distributed asymmetrically [47] and with a combination of tilt directions [73]. The cilia are again modelled using (4.4) however, this time with $a_0 = 0.15\,\mu\text{m}$ and a length that depends on whether wildtype or mutant embryos are being simulated [56, 82]. Wildtype cilia typically have an average length of $4\,\mu\text{m}$ ($\hat{\alpha} = 64/3$) whereas $DeltaD^{-/-}$ mutant cilia have an average length of $2.25\,\mu\text{m}$ ($\hat{\alpha} = 29/3$).

In this section the average velocity at any position is calculated using Gaussian integration in time, meaning that meshes are generated at time points $t_{nq} = T(\alpha_q + 1)/(2N_I) +$

$T(n-1)/N_I$ where α_q are the Gauss abscissas and

$$\boldsymbol{u}^{\text{ave}}(\boldsymbol{x}) = \frac{1}{T}\int_{t_0}^{t_0+T} \boldsymbol{u}(\boldsymbol{x},t)\mathrm{d}t \approx \frac{1}{2N_I}\sum_{n=1}^{N}\sum_{q=1}^{Q} \boldsymbol{u}\left(\boldsymbol{x},t_{nq}\right) w_q \tag{6.8}$$

where $N_I = 3$, $Q = 12$, $t_0 = 0.06$, $T = 1$ and w_q are the Gaussian integration weights. Gaussian integration is chosen over the left rectangle rule because the same accuracy can be achieved with little over half the time points; $n_{\text{beat}} = N_I Q = 36$ here.

The observations of Lopes and Rua *et al.* [personal communication] show that in wildtype embryos containing 70 cilia, approximately 50% have a single Fourier peak at $\hat{f}_1 = 36\,\text{Hz}$, 46 % have two Fourier peaks at $\hat{f}_1 = 36\,\text{Hz}$ and $\hat{f}_2 = 15\,\text{Hz}$, and the remaining 4 % are immotile. It is also observed that the distribution of these types of cilia is random inside the KV. The introduction of wobbling cilia into the simulations does change some of the local flow characteristics (figure 6.9(a)) but the overall flow in the AP-LR plane is similar to the previous results discussed in section 6.3.3 (compare figures 6.6(d) and 6.9(a)). The local flow from anterior to left is changed insofar as the faster portion of this flow extends further round the left side towards the posterior than before. Also, flow in the central region of this plane is now faster. However, overall the flow is still an anticlockwise swirl about the DV-axis with a slightly shifted centre towards the posterior, as observed in experiments [47, 81].

DeltaD$^{-/-}$ mutant zebrafish embryos do not only differ by having shorter cilia, the observed frequencies are also different. Approximately 74 % of cilia have a single Fourier peak at $\hat{f}_1 = 23\,\text{Hz}$, 19 % have two Fourier peaks, at $\hat{f}_1 = 40\,\text{Hz}$ and $\hat{f}_2 = 11\,\text{Hz}$, and the remaining 7 % are immotile. Again, these are distributed randomly inside the KV. The different cilia length and frequencies change the flow dramatically. The anticlockwise swirl is replaced with an uncoordinated flow that is slower at all points in the domain (figure 6.9(b)) suggesting that this flow will not be sufficient to break L-R symmetry correctly.

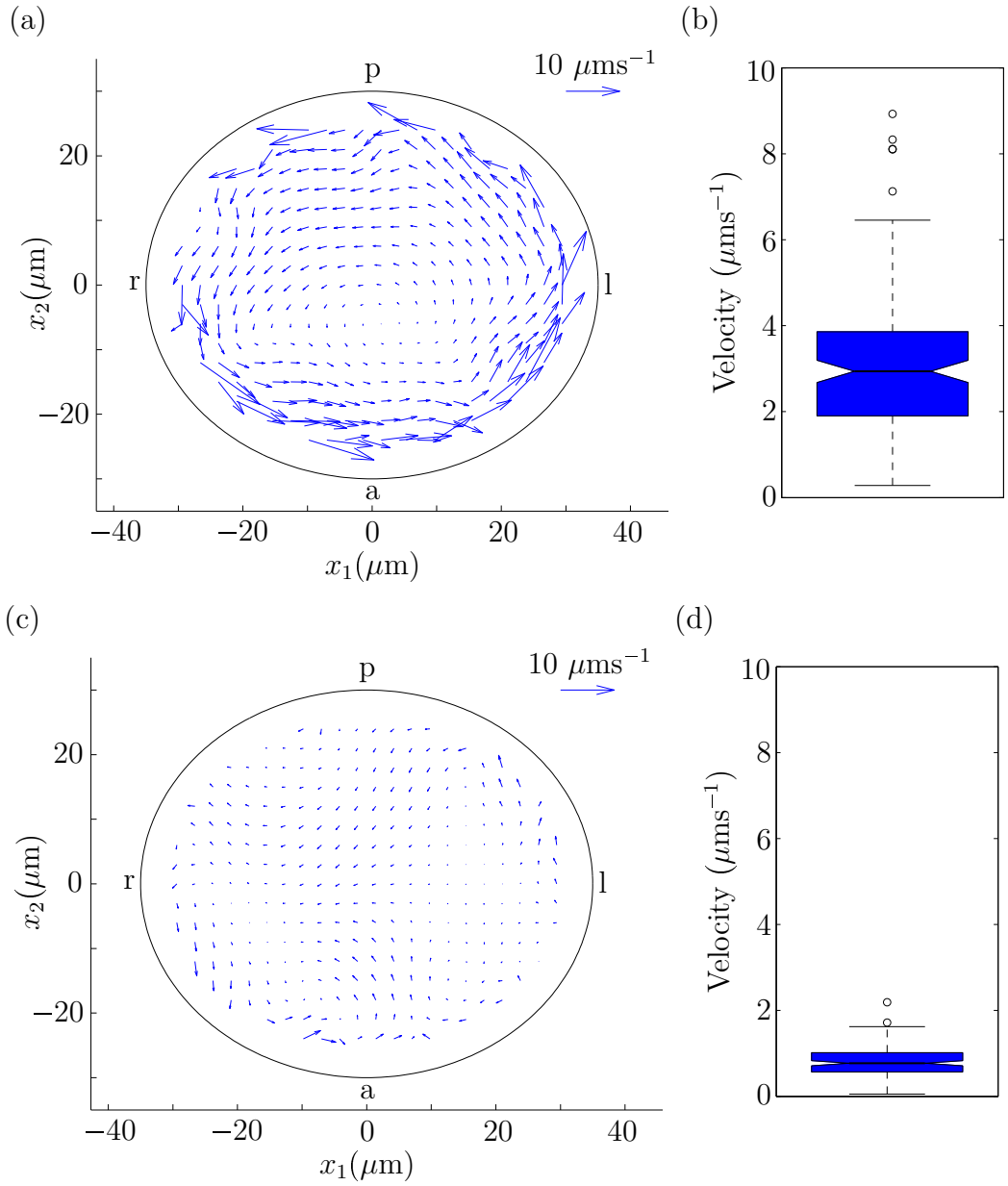

Figure 6.9: Time-averaged flow field $(u_1(\boldsymbol{x}), u_2(\boldsymbol{x}))$ in the AP-LR plane at $x_3 = 0$, computed over a beat cycle comprised of $n_{\text{beat}} = 36$ timesteps looking in the ventral direction. (a,c) Time-averaged flow fields. (b,d) Boxplots of time-averaged velocity magnitudes in a reduced ellipsoidal domain inside the Kupffer's vesicle sampled from 140 points. (a) Wildtype embryo, cilium length is $4\,\mu$m, with 50 % of cilia having a single Fourier peak, $\hat{f}_1 = 36\,$Hz, 46 % having two Fourier peaks, $\hat{f}_1 = 36\,$Hz and $\hat{f}_2 = 15\,$Hz, and 4 % immotile. (b) Wildtype embryo, mean time-averaged velocity magnitude is approximately $3\,\mu$ms^{-1}. (c) *DeltaD*$^{-/-}$ mutant embryo, cilium length is $2.25\,\mu$m, with 74 % of cilia having a single Fourier peak, $\hat{f}_1 = 23\,$Hz, 19 % having two Fourier peaks, $\hat{f}_1 = 40\,$Hz and $\hat{f}_2 = 11\,$Hz, and 7 % immotile. (d) *DeltaD*$^{-/-}$ mutant embryo, mean time-averaged velocity magnitude is approximately $1\,\mu$ms^{-1}. Cilia are distributed asymmetrically as shown in figure 6.6(e,f). Axis notation a, anterior; p, posterior; l, left and r, right.

6.5 Robustness of flow

No two Kupffer's vesicles and developed zebrafish will be truly identical and as such the distribution of cilia beat frequencies observed by Lopes and Rua *et al.* across many Kupffer's vesicles are different; it is found that the distribution of frequencies is random. However, wildtype zebrafish embryos will develop without any problems and $DeltaD^{-/-}$ mutant embryos will develop with organ positioning problems. This suggests that for the fluid flow to be a key step towards breaking the symmetry of the L-R body axis there must be some features of the flow that are consistent after randomising the cilia beat frequency distribution.

After randomising the cilia beat frequency distribution the faster flow from anterior to left is present in all simulated Kupffer's vesicles (figure 6.10) as is the anticlockwise swirl about the D-V axis. The centre of each swirl is also shifted towards the anterior by varying amounts and in some cases it is also shifted towards the right as well (figure 6.10(c,e)). The average velocity is approximately $3\,\mu\mathrm{ms}^{-1}$ and the leftward velocity is approximately $10\,\mu\mathrm{ms}^{-1}$ in all simulations despite the change in cilia beat frequency distribution.

6.6 Position dependent cilia length

Another interesting observation by Lopes and Rua *et al.* is that the length of cilia inside the Kupffer's vesicle is dependent on the location of the cilium. In wildtype embryos, cilia located anteriorly are longer (approximately $4\,\mu\mathrm{m}$) than cilia located posteriorly (approximately $3\,\mu\mathrm{m}$). The effect of a variable cilia length is shown in figure 6.11. Longer cilia produce a greater flow rate than shorter cilia and because there are more cilia located anteriorly than posteriorly a faster flow from anterior to left than from posterior to right is enhanced when compared to the cases where all cilia have the same length (figure 6.10). The average flow velocity is approximately $2.5\,\mu\mathrm{ms}^{-1}$ because some of the cilia are shorter (compare figures 6.10(b,d,f) and 6.11(b)).

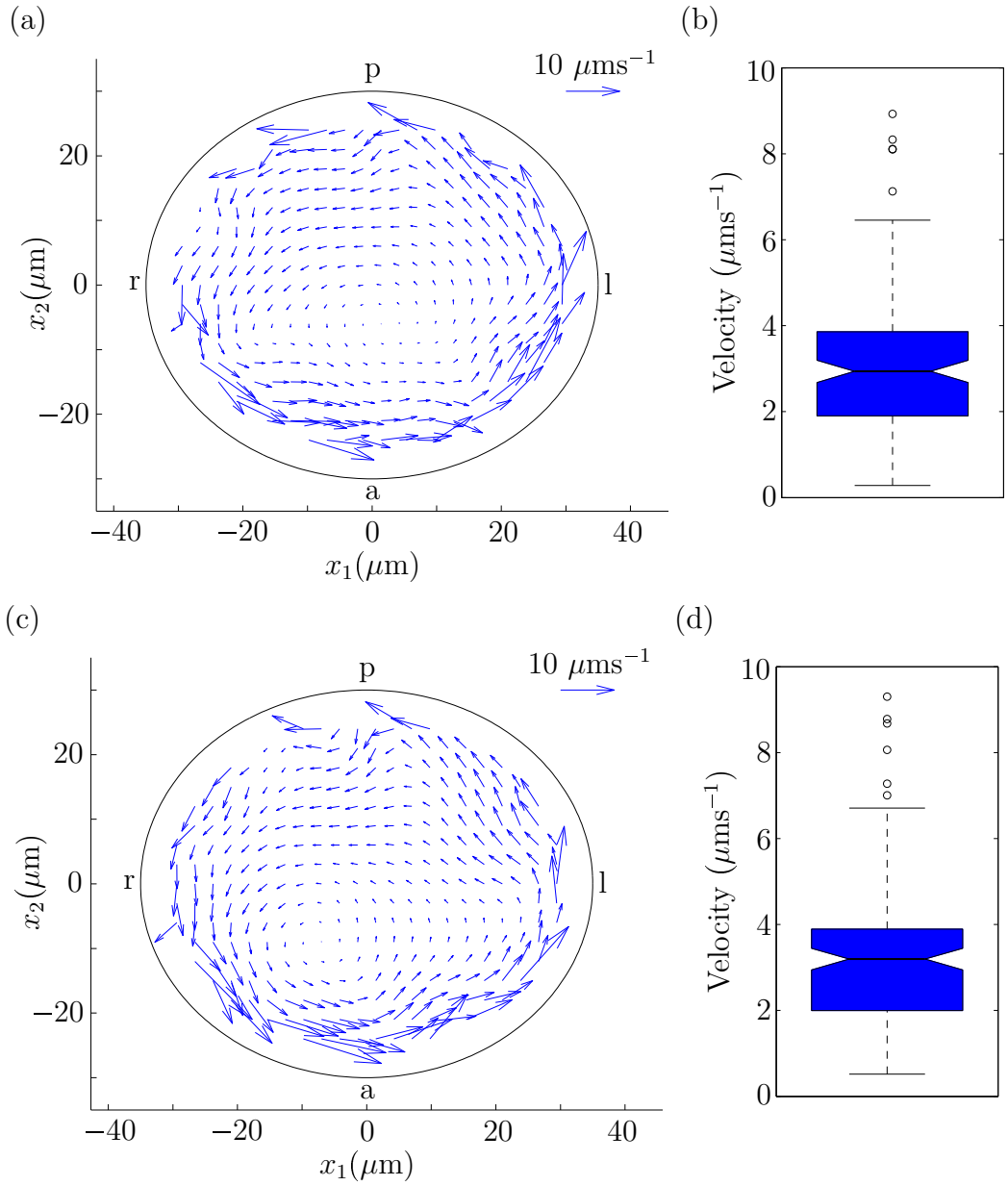

Figure 6.10: See below for details.

6.7 Summary

In this chapter a computational model of the zebrafish Kupffer's vesicle (KV) was developed that uses a mesh of the entire domain including cilia for the first time. A mesh of the domain allows greater modelling flexibility in the shape of cilia present inside the KV. This model was initially applied to six different cilia configurations based on experimental observations [46, 47, 56, 63, 81] for cilia length, tilt direction and angles, and cilia posi-

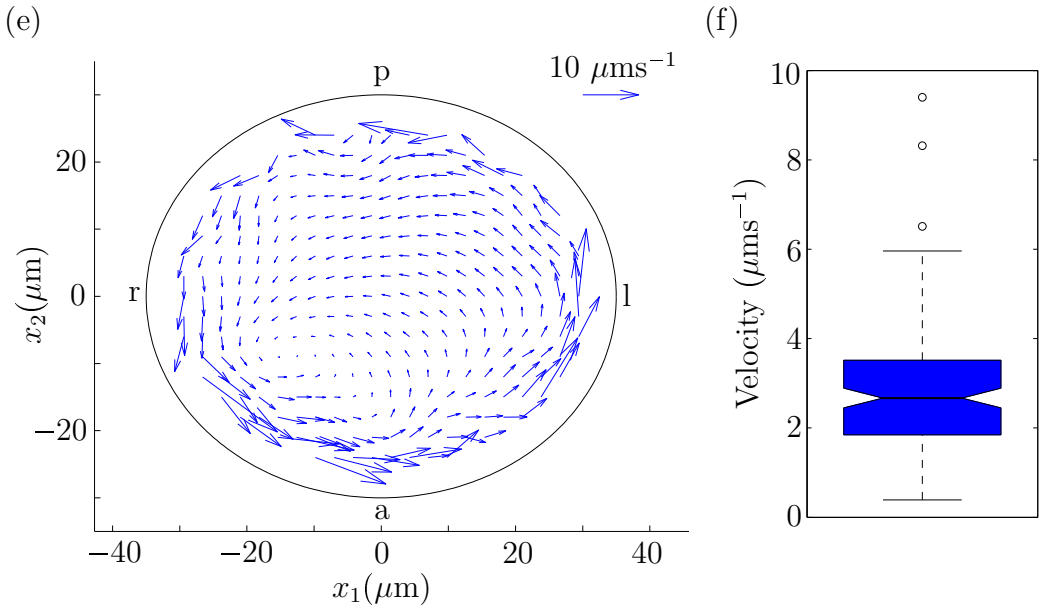

Figure 6.10: Time-averaged flow field $(u_1(\boldsymbol{x}), u_2(\boldsymbol{x}))$ in the AP-LR plane at $x_3 = 0$. All details are as figure 6.9(a,b). (a,c,e) Time-averaged flow fields. (b,d,f) Boxplots of time-averaged velocity magnitudes in a reduced ellipsoidal domain inside the Kupffer's vesicle sampled from 140 points. Cilia are distributed asymmetrically as shown in figure 6.6(e,f). Axis notation a, anterior; p, posterior; l, left and r, right.

tions. From the results of these simulations it can be predicted that the cilia configuration most likely to be present in the zebrafish KV is a combination of posterior and dorsal tilt directions depending on position coupled with an asymmetric cilia distribution between the dorsal roof and the ventral floor. This is a combination of the experimental observations of Kreiling *et al.* [47] and Supatto *et al.* [81] and is the only cilia configuration that closely reproduces the experimentally observed fluid flow of an anticlockwise swirl about the D-V axis with the centre shifted towards the anterior edge.

Experimental observations on cilia length [56] showed that wildtype embryos have cilia with an approximate length of $4\,\mu$m whereas $DeltaD^{-/-}$ mutant embryos have cilia with an approximate length of $2.25\,\mu$m. It is predicted from the simulation results that the velocity produced by shorter cilia will be slower. This result should be expected as the velocity in Stokes flow is proportional to the cilium length ($u \propto \omega L$) and it was shown in chapter 3 that the volume flow rate is proportional to the cube of cilium length ($Q \propto L^3$). Shortening cilia only reduces the calculated average velocity whereas the flow

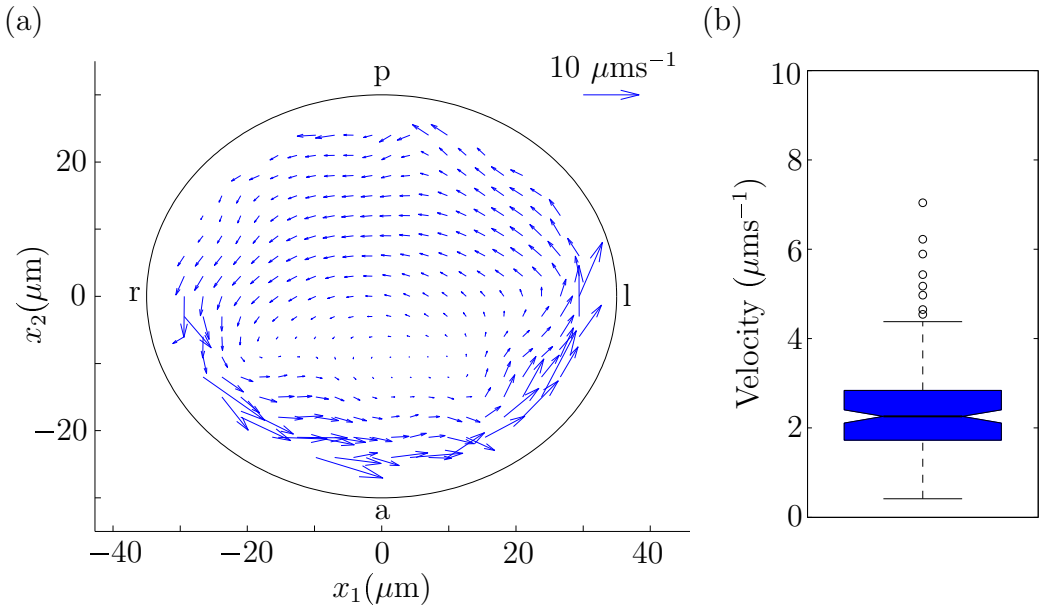

Figure 6.11: Time-averaged flow field $(u_1(\boldsymbol{x}), u_2(\boldsymbol{x}))$ in the AP-LR plane at $x_3 = 0$. All details are as figure 6.9(a,b). (a) Time-averaged flow fields. (b) Boxplot of time-averaged velocity magnitudes in a reduced ellipsoidal domain inside the Kupffer's vesicle sampled from 140 points. Cilia are distributed asymmetrically as shown in figure 6.6(e,f); cilia located anteriorly have length 4 μm and cilia located posteriorly have length 3 μm. Axis notation a, anterior; p, posterior; l, left and r, right.

characteristics remain unaltered.

Lopes and Rua *et al.* [personal communication] showed that the rotational frequency of shorter cilia in *DeltaD*$^{-/-}$ mutant embryos is different to the rotational frequency of wildtype cilia. Additionally, Lopes and Rua *et al.* showed that some cilia exhibit two frequencies as they rotate in both wildtype and mutant embryos, with the second frequency being interpreted as a wobble in this model. The effect of the change in frequencies between wildtype and mutant embryos is dramatic with the flow in mutant embryos being predicted to be much slower and uncoordinated when compared to the flow calculated in wildtype embryos when including the appropriate proportion of cilia with two frequencies. As the cilia beat frequency distribution is observed to be random these simulations were repeated for different frequency distributions. Changing the frequency distribution does not change the global flow features or the velocities, only some local flow features are altered.

A further observation by Lopes and Rua *et al.* is that cilia in wildtype embryos have

a different length depending on their position inside the KV. Longer cilia are observed in anterior regions and shorter cilia are observed in posterior regions. This has the effect of enhancing the stronger anterior to left flow and weakening the posterior to right flow because the positioning of longer cilia in anterior regions aligns with the greater proportion of cilia also found in the anterior region of the dorsal roof.

The results of all of these simulations show the importance of an asymmetric cilia distribution along with a combination of tilt directions. Furthermore, cilia length and cilium rotation frequencies are also shown to be critical to a suitable L-R symmetry breaking flow. This means that the zebrafish KV needs to develop each of these contributions to the fluid flow before it can be sufficient to break the symmetry of the L-R body axis.

CHAPTER 7

CONCLUSIONS

The question of how left-right asymmetric development is initiated in many vertebrate species has required, and will require, the continued input from many research fields. The clinical observations of Kartagener[43] in 1933 coupled with electron microscopy by Afzelius[2] in 1974 led to the original postulation that cilia could be involved in left-right asymmetric development. Then, in 1994, Sulik *et al.* [80] confirmed this hypothesis by observing cilia in the mouse organising structure, the embryonic node. The cilia, referenced as nodal cilia, were observed by Sulik *et al.* [80] and Nonaka *et al.* [60] performing a clockwise rotation that was generating a left directional fluid flow. The discovery of nodal cilia showed how they could be involved in left-right asymmetric development and the fluid flow was the earliest known left-right asymmetric event in development for the mouse. Subsequently, cilia and fluid flow have been observed in other species and in many, but not all, it is also the earliest left-right asymmetric event indicating how important fluid mechanics is in this problem. Because a fluid flow is present in the organising structure of these species, fluid mechanics can be used to gain a great amount of insight into this stage of development. Due to the small length and velocity scales of the organising structures the fluid flow can be accurately modelled using Stokes' equations and their singular solutions.

A theoretical study by Cartwright *et al.* [15] using the rotlet singularity of Stokes flow led to the proposal that nodal cilia in mice were tilted towards the already-established

posterior direction and that this mechanism would produce a directional flow from a rotational cilium movement; this was later verified experimentally by Okada *et al.* [65] and in a mechanical model by Nonaka *et al.* [61] This work was followed by Smith *et al.* [75] with nodal cilia in mice being modelled as slender ellipsoids using a centreline distribution of singularities and slender body theory coupled with a mesh representation of the covering membrane utilising the regularised boundary integral equation. By taking this model and varying the cilia parameters upright, missing and immotile cilia were simulated in this work as well as the different stages of development that the mouse node is present. When all cilia are upright, particles are swept around the mouse node in a 'global vortex'. Missing and immotile cilia alter the calculated particle paths as particles become trapped in single cilium vortices more frequently. This is because immotile or missing cilia have far less influence on the flow field. To simulate the different stages of development that the mouse node is present, late bud, early headfold, late headfold, 1 somite and 3 somite, the cilia parameters were varied; in particular the tilt angle of each cilium. The results of these simulations suggest that the mouse node has to develop first before a directional flow is established that could initiate left-right asymmetric development. This model enabled the flow fields inside the mouse node to be predicted under the action of many different cilia configurations. This is important because it is difficult to view fluid flow in the mouse node experimentally without removing the covering membrane. To visualise inside the node this membrane has to be removed to provide access to the flow region and this will certainly change the observed flow.

For this reason, and others, the zebrafish is an interesting organism to study. During development a zebrafish embryo is translucent allowing visualisation of fluid flow to be conducted without the removal of any of the bounding domain. The region of interest, the Kupffer's vesicle, appears at approximately 12 hours post-fertilisation which is much earlier than in the mouse. The geometry of the zebrafish Kupffer's vesicle is complex, comprising a scalene ellipsoid shape that has its entire internal surface lined with cilia. Due to this complexity the domain and cilia were modelled using a single mesh in this work.

Because the zebrafish embryo is transparent throughout development many experimental studies have been carried out. Supatto *et al.* [81] and Kreiling *et al.* [47] documented cilia positions, tilt directions and tilt angles as well as the type of fluid flow found inside the Kupffer's vesicle. Taking these observations, a comparative study was done to determine which parameters and positions the cilia require to produce the observed flow. It was determined that an asymmetric cilia distribution with respect to the anterior-posterior and dorsal-ventral axes is needed along with cilia located about the 'equator' having a tilt in the dorsal direction combined with cilia at the 'poles' having a tilt in the posterior direction. Another experimental study by Lopes *et al.* [56] showed how cilium length varies between wildtype and mutant zebrafish embryos, with cilia in wildtype embryos being 1–2 μm longer. Shorter cilia only reduces the calculated time-averaged flow velocity whilst the flow features remain unchanged. Cilium length has a significant effect on the fluid flow because the velocity is proportional to cilium length and the flow rate is proportional to the cube of cilium length. This suggests that cilia must grow to at least a certain length before the fluid flow is strong enough to initiate asymmetric development, again indicating that the Kupffer's vesicle has to develop itself first just as the mouse node does.

A related study was conducted by Lopes and Rua *et al.* looking at cilia beat frequencies. It was found that some cilia beat with a single frequency, others with multiple frequencies and the small remainder with no frequency meaning they are immotile. To introduce a second frequency into the cilia mechanism in the zebrafish model the cilia were made to 'wobble'. Lopes and Rua *et al.* showed that cilia in wildtype and mutant embryos have different cilia beat frequencies. By having some cilia wobbling in wildtype embryos and others immotile does change the local flow characteristics; however the global flow is not dramatically changed. In mutant embryos with different cilia beat frequencies and shorter cilia the calculated flow profiles are very different to those in wildtpe embryos. The predicted flow is uncoordinated and does not resemble an anticlockwise swirl about the dorsal-ventral axis. Another observation by Lopes and Rua *et al.* is that in wildtype

embryos cilia are longer if they are located in an anterior region rather than a posterior region. The impact of this is to enhance the asymmetric flow field that is faster from anterior to left than from posterior to right. These simulations suggest that the important cilium characteristics in the zebrafish Kupffer's vesicle are their position in the domain, tilt direction and cilium length that are position dependent and the cilia beat frequencies. The zebrafish Kupffer's vesicle needs all these parameters to be aligned so as to establish an appropriate fluid flow to initiate left-right asymmetric development. The results of the zebrafish mutant cases reinforce this as without the alignment of these flow parameters a suitable symmetry breaking flow is not created.

The computational code was developed independently of the mesh generation. Therefore, this code will work with any mesh subject to it being made up of quadratic quadrilateral and triangular elements. This means that other zebrafish cilia configurations can be studied or indeed any other species provided a series of meshes can be generated. The work on the zebrafish Kupffer's vesicle can be carried forward by using a mesh representation of the domain constructed directly from experimental images. To keep the degrees of freedom as low as possible, so computational times are reasonable, cilia can be modelled as slender ellipsoids across the whole domain as demonstrated in the mouse node model. These techniques will take the domain away from being an 'ideal' shape and will make any further results closer to those observed experimentally. From this, many different 'real' embryos can be modelled and any morphological differences between wildtype and mutant embryos can be captured adding an extra layer to what may also be involved in the robust left-right symmetry breaking of many vertebrate species from a directional fluid flow.

LIST OF REFERENCES

[1] M. Abramowitz and I. A. Stegun, *Handbook of mathematical functions with formulas, graphs, and mathematical tables*, Dover publications, 1964.

[2] B. A. Afzelius, *A human syndrome caused by immotile cilia*, Science **193** (1976), no. 4250, 317–319.

[3] ———, *Cilia-related diseases*, J. Pathol. **204** (2004), no. 4, 470–477.

[4] J. Ainley, S. Durkin, R. Embid, P. Boindala, and R. Cortez, *The method of images for regularized Stokeslets*, J. Comput. Phys. **227** (2008), no. 9, 4600–4616.

[5] G. K. Batchelor, *Slender-body theory for particles of arbitrary cross-section in Stokes flow*, J. Fluid Mech. **44** (1970), 419–440.

[6] ———, *The stress system in a suspension of force-free particles*, J. Fluid Mech. **41** (1970), no. 3, 545–570.

[7] J. R. Blake, *A note on the image system for a Stokeslet in a no-slip boundary*, Math. Proc. Camb. Philos. Soc. **70** (1971), 303–310.

[8] J. R. Blake and A. T. Chwang, *Fundamental singularities of viscous flow*, J. Eng. Math. **8** (1974), no. 1, 23–29.

[9] M. Blum, T. Weber, T. Beyer, and P. Vick, *Evolution of leftward flow*, Semin. Cell Dev. Biol., vol. 20, Elsevier, 2009, pp. 464–471.

[10] C. J. Brokaw, *Computer simulation of flagellar movement IX. Oscillation and symmetry breaking in a model for short flagella and nodal cilia*, Cell Motil. Cytoskeleton **60** (2005), no. 1, 35–47.

[11] ———, *Symmetry breaking in a model for nodal cilia*, AIP Conference Proceedings, vol. 755, 2005, pp. 107–117.

[12] N. A. Brown and L. Wolpert, *The development of handedness in left/right asymmetry*, Development **109** (1990), no. 1, 1–9.

[13] J. Buceta, M. Ibañes, D. Rasskin-Gutman, Y. Okada, N. Hirokawa, and J. C. Izpisúa-Belmonte, *Nodal cilia dynamics and the specification of the left/right axis in early vertebrate embryo development*, Biophys. J. **89** (2005), no. 4, 2199–2209.

[14] D. A. Cano, S. Sekine, and M. Hebrok, *Primary cilia deletion in pancreatic epithelial cells results in cyst formation and pancreatitis*, Gastroenterology **131** (2006), no. 6, 1856–1869.

[15] J. H. E. Cartwright, O. Piro, and I. Tuval, *Fluid-dynamical basis of the embryonic development of left-right asymmetry in vertebrates*, Proc. Natl. Acad. Sci. U.S.A. **101** (2004), no. 19, 7234–7239.

[16] T. Caspary, C. E. Larkins, and K. V. Anderson, *The graded response to sonic hedgehog depends on cilia architecture*, Dev. Cell **12** (2007), no. 5, 767–778.

[17] S. Childress, *Mechanics of swimming and flying*, vol. 2, Cambridge Univ. Press, 1981.

[18] A. T. Chwang and T. Y. Wu, *Hydromechanics of low-Reynolds-number flow. Part 2. Singularity method for Stokes flows*, J. Fluid Mech. **67** (1975), no. 4, 787–815.

[19] J. R. Colantonio, J. Vermot, D. Wu, A. D. Langenbacher, S. Fraser, J. N. Chen, and K. L. Hill, *The dynein regulatory complex is required for ciliary motility and otolith biogenesis in the inner ear*, Nature **457** (2009), no. 7226, 205–209.

[20] R. Cortez, *The method of regularized Stokeslets*, SIAM J. Sci. Comput. **23** (2001), no. 4, 1204–1225.

[21] R. Cortez, L. Fauci, and A. Medovikov, *The method of regularized Stokeslets in three dimensions: analysis, validation, and application to helical swimming*, Phys. Fluids **17** (2005), no. 031504, 1–14.

[22] A. Dabdoub and M. W. Kelley, *Planar cell polarity and a potential role for a wnt morphogen gradient in stereociliary bundle orientation in the mammalian inner ear*, J. Neurobiol. **64** (2005), no. 4, 446–457.

[23] J. G. de la Torre and V. A. Bloomfield, *Hydrodynamic theory of swimming of flagellated microorganisms*, Biophys. J. **20** (1977), no. 1, 49–67.

[24] G. Dhatt and G. Touzot, *The finite element method displayed*, vol. 27, Wiley, 1984.

[25] A. Erdélyi, W. Magnus, F. Oberhettinger, and F. G. Tricomi, *Tables of integral transforms. Vol. II. Based, in part, on notes left by Harry Bateman*, Bateman Manuscript Project, 1954.

[26] K. Feistel and M. Blum, *Three types of cilia including a novel* $9 + 4$ *axoneme on the notochordal plate of the rabbit embryo*, Dev. Dyn. **235** (2006), no. 12, 3348–3358.

[27] M. I. Ferrante, L. Romio, S. Castro, J. E. Collins, D. A. Goulding, D. L. Stemple, A. S. Woolf, and S. W. Wilson, *Convergent extension movements and ciliary function are mediated by ofd1, a zebrafish orthologue of the human oral-facial-digital type 1 syndrome gene*, Hum. Mol. Genet. **18** (2009), no. 2, 289–303.

[28] M. Fliegauf, T. Benzing, and H. Omran, *When cilia go bad: cilia defects and ciliopathies*, Nat. Rev. Mol. Cell Biol. **8** (2007), no. 11, 880–893.

[29] J. Gray and G. J. Hancock, *The propulsion of sea-urchin spermatozoa*, J. Exp. Biol. **32** (1955), no. 4, 802–814.

[30] J. Gros, K. Feistel, C. Viebahn, M. Blum, and C. J. Tabin, *Cell movements at hensens node establish left/right asymmetric gene expression in the chick*, Science **324** (2009), no. 5929, 941–944.

[31] H. Hamada, C. Meno, D. Watanabe, and Y. Saijoh, *Establishment of vertebrate left-right asymmetry*, Nat. Rev. Genet. **3** (2002), no. 2, 103–113.

[32] M. Hashimoto, K. Shinohara, J. Wang, S. Ikeuchi, S. Yoshiba, C. Meno, S. Nonaka, S. Takada, K. Hatta, A. Wynshaw-Boris, et al., *Planar polarization of node cells determines the rotational axis of node cilia*, Nat. Cell Biol. **12** (2010), no. 2, 170–176.

[33] N. Hirokawa, Y. Okada, and Y. Tanaka, *Fluid dynamic mechanism responsible for breaking the left-right symmetry of the human body: The nodal flow*, Annu. Rev. Fluid Mech. **41** (2009), 53–72.

[34] N. Hirokawa, Y. Tanaka, Y. Okada, and S. Takeda, *Nodal flow and the generation of left-right asymmetry*, Cell **125** (2006), no. 1, 33–45.

[35] Y. Hirota, A. Meunier, S. Huang, T. Shimozawa, O. Yamada, Y. S. Kida, M. Inoue, T. Ito, H. Kato, M. Sakaguchi, T. Sunabori, M. Nakaya, S. Nonaka, T. Ogura, H. Higuchi, H. Okano, N. Spassky, and K. Sawamoto, *Planar polarity of multiciliated ependymal cells involves the anterior migration of basal bodies regulated by non-muscle myosin ii*, Development **137** (2010), no. 18, 3037–3046.

[36] B. Q. Huang, T. V. Masyuk, M. A. Muff, P. S. Tietz, A. I. Masyuk, and N. F. LaRusso, *Isolation and characterization of cholangiocyte primary cilia*, Am. J. Physiol.-Gastroint. Liver Physiol. **291** (2006), no. 3, G500–G509.

[37] B. Huner and R. G. Hussey, *Cylinder drag at low Reynolds number*, Phys. Fluids **20** (1977), 1211.

[38] M. Ibañes and J. C. I. Belmonte, *Left-right axis determination*, WIREs: Systems Biology and Medicine **1** (2009), no. 2, 210–219.

[39] S. Ishijima and Y. Hiramoto, *Flexural rigidity of echinoderm sperm flagella.*, Cell structure and function **19** (1994), no. 6, 349.

[40] R. E. Johnson, *An improved slender-body theory for Stokes flow*, J. Fluid Mech. **99** (1980), no. 2, 411–431.

[41] R. E. Johnson and C. J. Brokaw, *Flagellar hydrodynamics. a comparison between resistive-force theory and slender-body theory*, Biophys. J. **25** (1979), no. 1, 113–127.

[42] O. Kagami and R. Kamiya, *Translocation and rotation of microtubules caused by multiple species of chlamydomonas inner-arm dynein*, J. Cell Sci. **103** (1992), no. 3, 653.

[43] M. Kartagener, *Zur pathogenese der bronchiektasien*, Lung **84** (1933), no. 1, 73–85.

[44] S. Kim and S. J. Karrila, *Microhydrodynamics*, Butterworth–Heinemann New York, 1991.

[45] C. B. Kimmel, W. W. Ballard, S. R. Kimmel, B. Ullmann, and T. F. Schilling, *Stages of embryonic development of the zebrafish*, Dev. Dyn. **203** (1995), no. 3, 253–310.

[46] A. G. Kramer-Zucker, F. Olale, C. J. Haycraft, B. K. Yoder, A. F. Schier, and I. A. Drummond, *Cilia-driven fluid flow in the zebrafish pronephros, brain and Kupffer's vesicle is required for normal organogenesis*, Development **132** (2005), no. 8, 1907–1921.

[47] J. A. Kreiling, Prabhat, G. Williams, and R. Creton, *Analysis of Kupffer's vesicle in zebrafish embryos using a cave automated virtual environment*, Dev. Dyn. **236** (2007), no. 7, 1963–1969.

[48] O. A. Ladyzhenskaya, *The mathematical theory of viscous incompressible flow*, Gordon and Breach, 1963.

[49] J. D. Lee and K. V. Anderson, *Morphogenesis of the node and notochord: the cellular basis for the establishment and maintenance of left-right asymmetry in the mouse*, Dev. Dyn. **237** (2008), no. 12, 3464–3476.

[50] M. Levin and M. Mercola, *Gap junction-mediated transfer of left-right patterning signals in the early chick blastoderm is upstream of shh asymmetry in the node*, Development **126** (1999), no. 21, 4703–4714.

[51] J. Lighthill, *Flagellar hydrodynamics: the John von Neumann lecture, 1975*, Siam Rev. (1976), 161–230.

[52] N. Liron, *Fluid transport by cilia between parallel plates*, J. Fluid Mech. **86** (1978), 705–726.

[53] ———, *The LGL (Lighthill-Gueron-Liron) theorem-historical perspective and critique*, Math. Meth. Appl. Sci. **24** (2001), no. 17-18, 1533–1540.

[54] N. Liron and S. Mochon, *Stokes flow for a Stokeslet between two parallel flat plates*, J. Eng. Math. **10** (1976), no. 4, 287–303.

[55] H. Lodish, A. Berk, S. L. Zipursky, P. Matsudaira, D. Baltimore, and J. Darnell, *Molecular cell biology*, Wiley Online Library, 1995.

[56] S. S. Lopes, R. Lourenço, L. Pacheco, N. Moreno, J. Kreiling, and L. Saúde, *Notch signalling regulates left-right asymmetry through ciliary length control*, Development **137** (2010), no. 21, 3625–3632.

[57] J. McGrath, S. Somlo, S. Makova, X. Tian, and M. Brueckner, *Two populations of node monocilia initiate left-right asymmetry in the mouse*, Cell **114** (2003), no. 1, 61–73.

[58] T. D. Montenegro-Johnson, A. A. Smith, D. J. Smith, D. Loghin, and J. R. Blake, *Modelling the fluid mechanics of cilia and flagella in reproduction and development*, Eur. Phys. J. E **35** (2012), no. 10.

[59] S. Nonaka, H. Shiratori, Y. Saijoh, and H. Hamada, *Determination of left-right patterning of the mouse embryo by artificial nodal flow*, Nature **418** (2002), no. 6893, 96–99.

[60] S. Nonaka, Y. Tanaka, Y. Okada, S. Takeda, A. Harada, Y. Kanai, M. Kido, and N. Hirokawa, *Randomization of left-right asymmetry due to loss of nodal cilia generating leftward flow of extraembryonic fluid in mice lacking KIF3B motor protein*, Cell **95** (1998), no. 6, 829–837.

[61] S. Nonaka, S. Yoshiba, D. Watanabe, S. Ikeuchi, T. Goto, W. F. Marshall, and H. Hamada, *De novo formation of left-right asymmetry by posterior tilt of nodal cilia*, PLoS Biol. **3** (2005), no. 8, 1467–1472.

[62] A. Okabe, B. N. Boots, K. Sugihara, and S. N. Chiu, *Spatial tessellations: concepts and applications of Voronoi diagrams*, Wiley & Sons Chichester., 1992.

[63] N. Okabe, B. Xu, and R. D. Burdine, *Fluid dynamics in zebrafish Kupffer's vesicle*, Dev. Dyn. **237** (2008), no. 12, 3602–3612.

[64] Y. Okada, S. Nonaka, Y. Tanaka, Y. Saijoh, H. Hamada, and N. Hirokawa, *Abnormal nodal flow precedes situs inversus in iv and inv mice*, Mol. Cell **4** (1999), no. 4, 459–468.

[65] Y. Okada, S. Takeda, Y. Tanaka, J. C. I. Belmonte, and N. Hirokawa, *Mechanism of nodal flow: a conserved symmetry breaking event in left-right axis determination*, Cell **121** (2005), no. 4, 633–644.

[66] J. M. Ottino, *The kinematics of mixing: stretching, chaos, and transport*, vol. 3, Cambridge Univ. Press, 1989.

[67] P. O. Persson and G. Strang, *A simple mesh generator in MATLAB*, SIAM Rev. **46** (2004), no. 2, 329–345.

[68] C. Pozrikidis, *Boundary integral and singularity methods for linearized viscous flow*, Cambridge Univ. Press, 1992.

[69] ———, *A practical guide to boundary element methods with the software library BEMLIB*, CRC Press, 2002.

[70] W. B. Russel, *Brownian motion of small particles suspended in liquids*, Annu. Rev. Fluid Mech. **13** (1981), no. 1, 425–455.

[71] A. Schweickert, T. Weber, T. Beyer, P. Vick, S. Bogusch, K. Feistel, and M. Blum, *Cilia-driven leftward flow determines laterality in xenopus*, Curr. Biol. **17** (2007), no. 1, 60–66.

[72] K. Shinohara, A. Kawasumi, A. Takamatsu, S. Yoshiba, Y. Botilde, N. Motoyama, W. Reith, B. Durand, H. Shiratori, and H. Hamada, *Two rotating cilia in the node cavity are sufficient to break left-right symmetry in the mouse embryo*, Nat. Commun. **3** (2012), 622–629.

[73] A. A. Smith, T. D. Johnson, D. J. Smith, and J. R. Blake, *Symmetry breaking cilia-driven flow in the zebrafish embryo*, J. Fluid Mech. **705** (2012), 26–45.

[74] D. J. Smith, *A boundary element regularized Stokeslet method applied to cilia- and flagella-driven flow*, Proc. R. Soc. A-Math. Phys. Eng. Sci. **465** (2009), 3605–3626.

[75] D. J. Smith, J. R. Blake, and E. A. Gaffney, *Fluid mechanics of nodal flow due to embryonic primary cilia*, J. R. Soc. Interface **5** (2008), no. 22, 567–573.

[76] D. J. Smith, E. A. Gaffney, and J. R. Blake, *Discrete cilia modelling with singularity distributions: application to the embryonic node and the airway surface liquid*, Bull. Math. Biol. **69** (2007), no. 5, 1477–1510.

[77] D. J. Smith, A. A. Smith, and J. R. Blake, *Mathematical embryology: the fluid mechanics of nodal cilia*, J. Eng. Math. **70** (2011), no. 1, 255–279.

[78] I. N. Sneddon, *Fourier transforms*, McGraw-Hill, 1951.

[79] C. D. Stern, R. T. Yu, A. Kakizuka, C. R. Kintner, L. S. Mathews, W. W. Vale, R. M. Evans, and K. Umesono, *Activin and its receptors during gastrulation and the later phases of mesoderm development in the chick embryo*, Dev. Biol. **172** (1995), no. 1, 192–205.

[80] K. Sulik, D. B. Dehart, T. Inagaki, J. L. Carson, T. Vrablic, K. Gesteland, and G. C. Schoenwolf, *Morphogenesis of the murine node and notochordal plate*, Am. J. Anat. **201** (1994), no. 3, 260–278.

[81] W. Supatto, S. E. Fraser, and J. Vermot, *An all-optical approach for probing microscopic flows in living embryos*, Biophys. J. **95** (2008), no. 4, 29–31.

[82] W. Supatto and J. Vermot, *From cilia hydrodynamics to zebrafish embryonic development*, Curr. Top. Dev. Biol. **95** (2011), 33–66.

[83] C. Tabin, *Do we know anything about how left-right asymmetry is first established in the vertebrate embryo?*, J. Mol. Histol. **36** (2005), no. 5, 317–323.

[84] C. J. Tabin and K. J. Vogan, *A two-cilia model for vertebrate left-right axis specification*, Genes Dev. **17** (2003), no. 1, 1–6.

[85] Y. Tanaka, Y. Okada, and N. Hirokawa, *Fgf-induced vesicular release of sonic hedgehog and retinoic acid in leftward nodal flow is critical for left-right determination*, Nature **435** (2005), no. 7039, 172–177.

[86] M. A. Taylor, B. A. Wingate, and R. E. Vincent, *An algorithm for computing Fekete points in the triangle*, SIAM J. Numer. Anal. **38** (2001), no. 5, 1707–1720.

[87] S. C. Teilmann and S. T. Christensen, *Localization of the angiopoietin receptors tie-1 and tie-2 on the primary cilia in the female reproductive organs*, Cell Biol. Int. **29** (2005), no. 5, 340–346.

[88] R. D. Vale and Y. Y. Toyoshima, *Rotation and translocation of microtubules in vitro induced by dyneins from tetrahymena cilia*, Cell **52** (1988), no. 3, 459–469.

APPENDIX A

JOURNAL OF ENGINEERING MATHEMATICS PUBLICATION

The paper in this appendix is published in the Journal of Engineering Mathematics, co-written with my Ph.D. supervisors, and should be referenced for further background. The publication details are, J. Eng. Math., (2011), **70**, pp. 255–279, doi: 10.1007/s10665-010-9383-y.

APPENDIX B

JOURNAL OF FLUID MECHANICS PUBLICATION

The paper in this appendix is published in the Journal of Fluid Mechanics, co-written with a fellow Ph.D student, Thomas Montenegro-Johnson (né Johnson), and our Ph.D. supervisors, and should be referenced for further background. The publication details are, J. Fluid Mech., (2012), **705**, pp. 26–45, doi: 10.1017/jfm.2012.117.

APPENDIX C

EUROPEAN PHYSICAL JOURNAL E PUBLICATION

The paper in this appendix is published in the European Physical Journal E, co-written with a fellow Ph.D student, Thomas Montenegro-Johnson (né Johnson), and our Ph.D. supervisors, and should be referenced for further background. The publication details are, Eur. Phys. J. E, (2012), **35**, doi: 10.1140/epje/i2012-12111-1.